UNIVERSITY OF CALIFORNIA
RIVERSIDE

First Principles Insights into Ion Transport and Intercalation in MXenes and Transition Metal Oxides

A Dissertation submitted in partial satisfaction
of the requirements for the degree of

Doctor of Philosophy

in

Chemistry

by

Yangyunli Sun

June 2021

Dissertation Committee:
Dr. De-en Jiang, Chairperson
Dr. Gregory Beran
Dr. Ludwig Bartels

The Dissertation of Yangyunli Sun is approved:

Committee Chairperson

University of California, Riverside

COPYRIGHT ACKNOWLEDGEMENT

The text and figure in Chapter 3, in part or full, are reproduced from "Proton Redox and Transport in MXene-Confined Water", ACS applied materials & interfaces,2019,12(1): 763-770. The co-author (Dr. De-en Jiang) directed and supervised the research that forms the basis of this chapter.

The text and figure in Chapter 4, in part or full, are reproduced from "Titanium carbide MXene shows an electrochemical anomaly in water-in-salt electrolytes" (under review of Nature). The co-authors (Dr. Yury Gogotsi and De-en Jiang) directed and supervised the research that forms the basis of this chapter. Other co-authors include Xuehang Wang, Tyler S. Mathis, Wan-Yu Tsai, Netanel Shpigel, Hui Shao, Danzhen Zhang, Kanit Hantanasirisakul, Fyodor Malchick, Nina Balke, and Patrice Simon.

The text and figure in Chapter 5, in part or full, are reproduced from "MXene Edge Reconstruction from *ab initio* Evolutional Study" (in preparation). The co-author (Dr. De-en Jiang) directed and supervised the research that forms the basis of this chapter.

The text and figure in Chapter 6, in part or full, are reproduced from "Optimal Linear Water Density for Proton" (Journal of Physical Chemistry C, doi.org/10.1021/acs.jpcc.1c00205). The co-author (Dr. De-en Jiang) directed and supervised the research that forms the basis of this chapter.

The text and figure in Chapter 7, in part or full, are reproduced from "Confined Interlayer Water Promotes Structural Stability for High-Rate Electrochemical Proton Intercalation in Tungsten Oxide Hydrates", ACS Energy Letters, 2019, 4(12): 2805-2812.

The co-authors (Dr. Veronica Augustyn and Dr. De-en Jiang) directed and supervised the

research that forms the basis of this chapter. Other co-authors include James B. Mitchell, Natalie R. Geise, Alisa R. Paterson, Naresh C. Osti, Simon Fleischmann, Rui Zhang, Louis A. Madsen, Michael F. Toney, Alexander I. Kolesnikov，and Eugene Mamontov.

The text and figure in Chapter 8, in part or full, are reproduced from "Fast Proton Insertion in Layered $H_2W_2O_7$ via Selective Etching of an Aurivillius Phase", Advanced Energy Materials, 2021, 11(1): 200335. The co-authors (Dr. Veronica Augustyn and Dr. De-en Jiang) directed and supervised the research that forms the basis of this chapter. Other co-authors include: Ruocun Wang, Alexander Brady, Simon Fleischmann, Tim B. Eldred, Wenpei Gao, and Hsiu-Wen Wang.

ACKNOWLEDGMENTS

First of all, I would like to show my special thanks to my research advisor Prof. De-en Jiang. Without his patient guidance and support, this work wouldn't be possible appear. I also like to thank my committee members, Dr. Gregory Beran and Dr. Ludwig Bartels for their helpful suggestions in my SYRE and qualify exam.

Then, I would like to thank my research collaborators in FIRST-EFRC: Prof. Veronica Augustyn, Prof. Yury Gogotsi, Dr. Paul R. C. Kent, Prof. Michael Naguib, and Prof. Adri C. T. van Duin for productive collaborations and valuable experiences in various research areas.

Finally, I would like to appreciate the nice experience with my groupmates, especially Dr. Cheng Zhan and Dr. Lihua Xu, for their helpful discussions.

Last but not least, I would like to thank my parents for their strong supporting.

This work was supported by the Fluid Interface Reactions, Structures, and Transport (FIRST) Center, an Energy Frontier Research Center founded by the U.S. Department of Energy (DOE), Office of Science, Office of Basic Energy Sciences. This research used computing resources from the National Energy Research Scientific Computing Center (NERSC).

DEDICATED TO

My parents, Shuangping Sun and Hongmei Hu.

ABSTRACT OF THE DISSERTATION

First Principles Insights into ion Transport and Intercalation in MXenes and Transition Metal Oxides

by

Yangyunli Sun

Doctor of Philosophy, Graduate Program in Chemistry
University of California, Riverside, June 2021
Dr. De-en Jiang, Chairperson

The dream device for electrochemical energy storage (EES) should have both high energy density (as in batteries) and high power density (as in supercapacitors). Pseudocapacitors are a promising type of EES technologies toward that dream. The power density of a pseudocapacitor is mainly determined by the ion transport at the interface and inside the electrode. Therefore, atomistic understanding of the ion intercalation and transport is needed for rational design of high-performance pseudocapacitors. In this dissertation, we have investigated the ion transport, intercalation mechanism, interfacial structure, and spectroscopic features of two typical pseudocapacitive systems: MXenes (2D metal carbides and nitrides) and tungsten oxide hydrates.

In the first part of the dissertation, we employed density functional theory (DFT) and first-principles molecular dynamics (FPMD) to study the ion insertion and transport in MXene electrodes. We first studied the proton dynamics in MXene-confined water to understand the relation between proton diffusion and surface redox behavior under

confinement. Then, we studied the Li^+ insertion into MXene in water-in-salts electrolyte. Our DFT calculation agrees well with the experimental electrochemical quartz crystal microbalance (EQCM) and in-situ X-ray diffraction (XRD) results, suggesting the desolvation-free Li^+ (de)intercalation mechanism. Next, we investigated MXene edge structure by integrating the DFT calculation and structural search methods. The predicted most stable structure in vacuum exhibits an interlayer connection at the edge, while the configurational search of hydrated edge suggests the spontaneous CH_4 formation, which was observed in previous experiments.

In the second part of the dissertation, we studied the protonation sites and proton diffusion in tungsten oxides hydrates. We first investigated proton diffusion in tunnel *h*-WO_3 and reported the optimal linear water density of 4 water/nm for highest proton conductivity. Next, we compared the calculated vibrational densities of states (VDOS) with inelastic neutron scattering (INS) measurement, to pinpoint proton at the bridging oxygen site in monoclinic $WO_3 \cdot H_2O$. Finally, we studied the proton adsorption in the $H_2W_2O_7$ and revealed low proton adsorption energies at terminal oxygen sites.

In summary, our simulation work provided significant mechanistic understanding on the pseudocapacitive behavior of MXenes and tungsten oxides hydrates from both thermodynamic and kinetic perspectives, which will facilitate the development of high-performance pseudocapacitors for EES.

Table of Contents

List of Figures

Chapter 1. Introduction

1.1. Energy storage materials

The conventional energy resource fossil fuel has been the main primary energy resource for decades. Although fossil fuels are continuously accumulating by natural processes, they are consuming much faster than new ones are formed. Furthermore, burning fossil fuels results in serious environmental pollution such as acid rain, global warming, and so on. Under this circumstance, the search for renewable energy resources is ongoing worldwide. To better utilize and store renewable energy resources, electrochemical energy storage (EES) devices are needed. Moreover, since Li-ion batteries have deeply changed our daily life, there are growing needs to powering multiple potable and wearable electronics as well as electric vehicles. This also demands EES devices. In general, we desire EES material that can store and output a large amount of energy in a short period meanwhile possess a long lifetime.

Supercapacitors are important energy storage devices due to their ability to achieve both high energy density and power density. Based on the charge storage mechanism, there are mainly two types of supercapacitors: Electric double layer capacitors (EDLCs), which store energy via electrolyte ions adsorption on charged surface; pseudocapacitors, which store energy through surface or near surface redox reaction. Comparing with EDLCs, pseudocapacitors usually exhibit relatively higher energy density. While comparing with batteries, pseudocapacitors usually possess higher power density. In other words, pseudocapacitors occupy a middle ground between EDLCs and batteries.

1.2. Types of pseudocapacitance

The concept of pseudocapacitance can be trace back to the work of Conway and Gileadi in early 1960s who used pseudocapacitance to describe the reversible electrochemical capacitance related to surface adsorption.[1] Since then, the concept of pseudocapacitance has been extended. Depending on the process associated with pseudocapacitance, it can be classified into 3 types: 1) adsorption pseudocapacitance which related to the monolayer electrochemical adsorption; 2) redox pseudocapacitance which associated with faradic reaction; 3) intercalation pseudocapacitance which corresponded with intercalation process that does not result in the phase transition of the host. The schematic illustration of the three types of pseudocapacitance is shown in Figure 1.1.

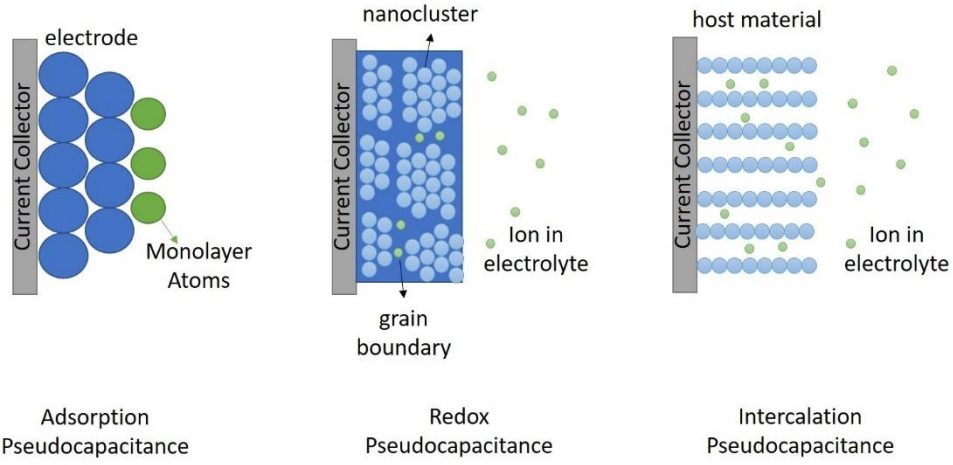

Figure 1.1 Illustration of the three types of pseudocapacitance.

As emerging works have demonstrated that structure tunning, surface engineering or crystal morphology designing may introduce pseudocapacitive contribution in the charge storage process, the distinction between different types of pseudocapacitive and battery type process becomes blurred. Therefore, the understanding of the atomic origins that enables the transformation in energy storage relevant system is desired.

1.3. Pseudocapacitive material

Due to the potential of achieving both high energy and high power density in pseudocapacitors, plenty of efforts have been put into finding new pseudocapacitive materials and achieving pseudocapacitive energy storage in conventional electrode material by structure designing. Transition metal oxides are the most well-known pseudocapacitive materials, while there are also newly discovered materials such as MXenes, perovskite oxides, and metal-organic frameworks that exhibit pseudocapacitive behavior. In this thesis, we mainly focus on MXenes and transition metal oxides. In particular, $Ti_3C_2T_x$ and tungsten oxides.

1.3.1. 2D transition metal carbides/nitrides (MXenes)

About a decade ago, MXenes were introduced as a new family of two-dimensional transition metal carbide, carbonitride, or nitride with a general formula of $M_{n+1}X_n$ (M=metal; X=C, N).[2-4] It can be synthesized through selective etching the "A" layer from the MAX phase (Figure 1.2). MXenes exhibit covalent bonds between M and X atoms. The two-dimensional sheets are stacked through the weak interlayer van der Waals interaction. MXenes possess an electronically conductive carbide/nitride core, and plenty of interlayer ion storage sites and diffusion pathways. These structural features make MXenes great candidates as pseudocapacitance energy storage material. Due to the flexible interlayer, depending on the type of electrolyte and MXene's interlayer chemistry, ions with different solvation structures can potentially be intercalated into the MXene layers, hence results in different charge storage capacities and dynamics.

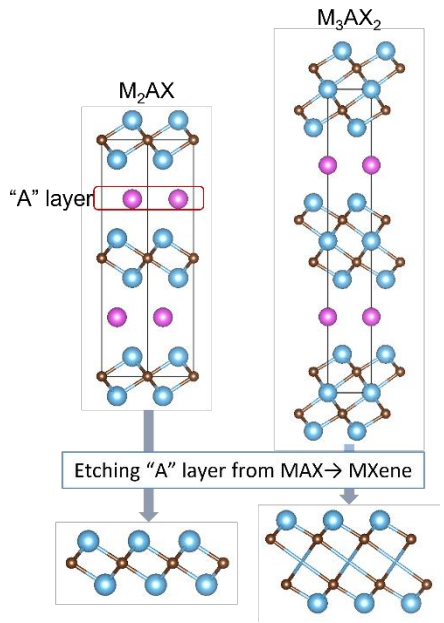

Figure 1.2 Schematic illustration of the formation of MXenes from MAX phase.

Different charge storage capacities have been observed in neutral, basic, and acidic electrolytes. When MXene is immersed in neutral and basic electrolytes, a large number of solvated cations of different charges and sizes can be inserted into the interlayer of MXene resulting in interlayer spacing expansion. [4] Lukatskaya *et al*. reported a capacitance around 80 F/g in 1 M K_2SO_4 at a rate of 2 mV/s.[4] Comparing to neutral and basic electrolytes, MXenes have been reported relatively high capacity in acidic electrolytes. Ghidiu *et al*. demonstrated $Ti_3C_2T_x$ electrodes with mixed F and O terminations exhibit capacities ~ 245 F/g at 2 mV/s.[5] Lukatskaya *et al*. performed in situ XANES to measure the change of the Ti oxidation state in $Ti_3C_2T_x$ when cycled in 1 M H_2SO_4 electrolyte.[6] The measurement of the averaged Ti oxidation state change accord well with the experimental capacity, which confirmed the charge storage was dominated by pseudocapacitive proton intercalation. Mu *et al*. employed in situ X-rag diffraction to investigate the charging mechanism of the $Ti_3C_2T_x$ electrode in 1M H_2SO_4 and found the interlayer spacing expands and shrinks

during charge and discharge cycles by about 0.5 Å which confirmed the volume change during the electrochemical cycle.[7]

More efforts will be made on revealing fundamental understandings of charge storage in MXenes. MXenes not only can serve as great materials to achieve both high energy density and power density, but they also can act as a good material platform for understanding energy storage under confinement.

1.3.2. Transition metal oxides

Transition metal oxides are the most well-known pseudocapacitive materials. The first discovered pseudocapacitance in transition metal oxides can be trace back to 1971 when the charge storage behavior of RuO_2 thin film in H_2SO_4 was reported. It has been reported to exhibit capacitance of about ~720 F/g in a voltage window of 1V at a scan rate of 2mV/s.[8] This value is much higher than double-layer capacitances of active carbons. The attractive performance of RuO_2 has then stimulated the interest in achieving pseudocapacitance in low-cost and abundant transition metal oxides.

Tungsten oxides and its hydrate has been deemed as possible pseudocapacitive material. The most notable phases are monoclinic WO_3 (m-WO_3) and hexagonal WO_3 (h-WO_3). These two phases are both formed by WO_6 octahedra but with different arrangements of the octahedra.

Monoclinic WO_3 is formed by a three-dimensional network of corner-sharing distorted WO_6 octahedra. While the hydrate phase of Monoclinic WO_3 is a layered compound with structural water locate at the interlayer. Previous study on proton conductivity of WO_3 hydrate has demonstrated $WO_3 \cdot 2H_2O$ possess high proton

conductivity. At different temperature ranges, it has been found to exhibit different proton conduction barriers. The barrier of 0.36 eV at high temperature was attributed to the proton bulk diffusion, while the low barrier of 0.15 eV at low temperature region was attributed to surface diffusion.[9] Following study on WO_3 hydrates revealed a non-Grotthuss proton diffusion mechanism for $WO_3 \cdot 2H_2O$ from first-principles simulations. The high proton conductivity indicating $WO_3 \cdot 2H_2O$ could serve as electrode material with good rate performance. This has been demonstrated by Mitchell *et al*. that revealed the transition from battery-like charge storage behavior of anhydrous monoclinic WO_3 to pseudocapacitive behavior in $WO_3 \cdot 2H_2O$ in H_2SO_4.[10] Further study from Wang *et al*. discovered that the high rate capability of $WO_3 \cdot 2H_2O$ is resulted from its flexible structure.[11]

For the hexagonal phase of tungsten oxides, the corner shared octahedra arranged in a six-member ring. This arrangement forms hexagonal tunnels along the (001) direction throughout the whole lattice. Sun *et al*. found the large internal surface area of h-WO_3 is accessible for both CO_2 and electrolytes.[12] Zhu *et al*. demonstrate h-WO_3 exhibit pseudocapacitance behavior in H_2SO_4 with a capacitance of up to 421.8 F/g under the current density of 0.5 A/g.[13] Jiang *et al*. employed electrochemical quartz crystal microbalance (EQCM) to monitor the mass evolution of h-WO_3 hydrate electrode. They found both the proton and the confined water goes in and out the tunnel during the charge/discharge process.[14]

1.4. Important research questions and knowledge gaps in understanding pseudocapacitive energy storage in MXenes and tungsten oxides

Despite the plenty of reports on pseudocapacitive of MXenes, our understanding on the pseudocapacitive behavior of MXenes is still limited. For example, how does the confinement from the MXene affects the dynamics of ions and molecules? Moreover, how does the working ion type and concentration affect the energy storage behavior? In this thesis, we adopted density functional theory (DFT) simulations to achieve deeper understanding on the energy storage mechanism of MXenes.

Due to the nice crystalline structure and flexible structure arrangement as well as the unique effect of structural water, tungsten oxides provide a nice platform to study structure designing strategies to achieve pseudocapacitive energy storage. Thus, understand the proton diffusion and adsorption in different tungsten oxides and tungsten oxide hydrates can potentially benefit the development of pseudocapacitors. Specifically, we are interested in following questions: 1) How does the proton diffuse in tungsten oxide hydrates and 2) where are the protons locating during the pseudocapacitive energy storage process. In this thesis, we collaborated with an experimental group, investigated the proton transport and intercalation in different phases of tungsten oxides hydrates to achieve better understanding on the correlation of the crystal structure and the energy storage behavior in tungsten oxides.

References

1. Conway, B. E.; Gileadi, E., Kinetic theory of pseudo-capacitance and electrode reactions at appreciable surface coverage. *Transactions of the Faraday Society* **1962,** *58* (0), 2493-2509.

2. Naguib, M.; Kurtoglu, M.; Presser, V.; Lu, J.; Niu, J.; Heon, M.; Hultman, L.; Gogotsi, Y.; Barsoum, M. W., Two-Dimensional Nanocrystals Produced by Exfoliation of Ti_3AlC_2. **2011,** *23* (37), 4248-4253.

3. Naguib, M.; Mashtalir, O.; Carle, J.; Presser, V.; Lu, J.; Hultman, L.; Gogotsi, Y.; Barsoum, M. W., Two-Dimensional Transition Metal Carbides. *ACS Nano* **2012,** *6* (2), 1322-1331.

4. Anasori, B.; Lukatskaya, M. R.; Gogotsi, Y., 2D metal carbides and nitrides (MXenes) for energy storage. *Nature Reviews Materials* **2017,** *2* (2), 16098.

5. Ghidiu, M.; Lukatskaya, M. R.; Zhao, M.-Q.; Gogotsi, Y.; Barsoum, M. W., Conductive two-dimensional titanium carbide 'clay' with high volumetric capacitance. *Nature* **2014,** *516* (7529), 78-81.

6. Lukatskaya, M. R.; Bak, S.-M.; Yu, X.; Yang, X.-Q.; Barsoum, M. W.; Gogotsi, Y., Probing the Mechanism of High Capacitance in 2D Titanium Carbide Using In Situ X-Ray Absorption Spectroscopy. **2015,** *5* (15), 1500589.

7. Mu, X.; Wang, D.; Du, F.; Chen, G.; Wang, C.; Wei, Y.; Gogotsi, Y.; Gao, Y.; Dall'Agnese, Y., Revealing the Pseudo-Intercalation Charge Storage Mechanism of MXenes in Acidic Electrolyte. **2019,** *29* (29), 1902953.

8. Zheng, J. P.; Cygan, P. J.; Jow, T. R., Hydrous Ruthenium Oxide as an Electrode Material for Electrochemical Capacitors. *Journal of The Electrochemical Society* **1995,** *142* (8), 2699-2703.

9. Li, Y. M.; Hibino, M.; Miyayania, M.; Kudo, T., Proton conductivity of tungsten trioxide hydrates at intermediate temperature. *Solid State Ionics* **2000,** *134* (3), 271-279.

10. Mitchell, J. B.; Lo, W. C.; Genc, A.; LeBeau, J.; Augustyn, V., Transition from Battery to Pseudocapacitor Behavior via Structural Water in Tungsten Oxide. *Chemistry of Materials* **2017,** *29* (9), 3928-3937.

11. Wang, R.; Mitchell, J. B.; Gao, Q.; Tsai, W.-Y.; Boyd, S.; Pharr, M.; Balke, N.; Augustyn, V., Operando Atomic Force Microscopy Reveals Mechanics of Structural Water Driven Battery-to-Pseudocapacitor Transition. *ACS Nano* **2018,** *12* (6), 6032-6039.

12. Sun, W.; Yeung, M. T.; Lech, A. T.; Lin, C.-W.; Lee, C.; Li, T.; Duan, X.; Zhou,

J.; Kaner, R. B., High Surface Area Tunnels in Hexagonal WO_3. *Nano Letters* **2015,** *15* (7), 4834-4838.

13. Zhu, M.; Meng, W.; Huang, Y.; Huang, Y.; Zhi, C., Proton-Insertion-Enhanced Pseudocapacitance Based on the Assembly Structure of Tungsten Oxide. *ACS Applied Materials & Interfaces* **2014,** *6* (21), 18901-18910.

14. Jiang, H.; Hong, J. J.; Wu, X.; Surta, T. W.; Qi, Y.; Dong, S.; Li, Z.; Leonard, D. P.; Holoubek, J. J.; Wong, J. C.; Razink, J. J.; Zhang, X.; Ji, X., Insights on the Proton Insertion Mechanism in the Electrode of Hexagonal Tungsten Oxide Hydrate. *Journal of the American Chemical Society* **2018,** *140* (37), 11556-11559.

Chapter 2. Methods and Theories

2.1. Rationales for the computational methods of choice and theories behind

Probing the location of the working ions is important to understand the energy storage mechanism of the electrode material. Density functional theory (DFT) simulation is a convenient way to study atoms/molecules binding site by comparing the binding energy that obtained from electronic level accuracy. While the main issue with DFT is the actual term of exchange correlation functional is unknown. Local density approximation (LDA) and generalized gradient approximation (GGA) are two commonly used approximations for exchange correlation functional. LDA is known for overbinding, especially for molecules. While GGA succeeds in reducing the effects of LDA overbinding by incorporating the inhomogeneities of the electron density. Thus, in this thesis, we adopted GGA for exchange correlation functional, in particular, the Perdew-Burke-Ernzerhof (PBE)[1] version.

For systems like two-dimension materials that are stacked by van der Waals interaction between the layers or liquid system that forms networks through hydrogen bonding, accurately describing the van der Waals interaction is required. However, GGA can't correctly describe the van der Waals interaction. Thus, we need to incorporate van der Waals correction in DFT. The simplest way is to add energy correction to the conventional Kohn Sham DFT energy. Here, we adopted the DFT-D2[2] and DFT-D3[3] methods proposed by Grimme *et al*.

Due to the complexity of interfacial chemistry and physics in pseudocapacitors,

FPMD can be a handy way to obtain the atomic details of ion transport behavior. With FPMD, we can obtain the dynamic behavior of ion at electronic level accuracy and investigate the ion transport behavior under picosecond timescales. Based on the power of FPMD simulation, we can investigate the detailed mechanism of ion movement under confinement, and how the chemical environment affects its diffusivity.

2.2. Density functional theory

Density functional theory (DFT) is a computational modeling method based on the two Hohenberg-Kohn theorems and the Kohn Sham equation to solve the ground state electronic structures. Since it was first proposed in the 1970s, it has been a popular method to study the ground states properties of atoms, molecules, and condensed phases.

2.2.1. Hohenberg-Kohn theorem

The idea of density functional theory was originally proposed in the Thomas-Fermi model and then put on a firm theoretical foundation in the framework of the two Hohenberg-Kohn theorems[4]. The first theorem demonstrates that the ground state properties of any many-body system can uniquely determine by the electron density. The second theorem proves that the true ground-state electron density is the density that minimizes the total energy. By using the functionals of the spatial electron density, the many-body problem of N electrons with 3N spatial coordinates is reducing to three spatial coordinates.

2.2.2. Kohn-Sham DFT

The Hohenberg-Kohn theorems was then further developed by Walter Kohn and Lu Jeu Sham to Kohn-Sham DFT (KS DFT).[5] Under this framework, the full interacting

system is reduced to a fictitious non-interacting system where the electrons move in an effective 'Kohn-Sham' single-particle potential. The total energy of the system is then expressed as:

$$E_{KS}[n] = \sum_i \int dr \varphi_i^*(r)(-\frac{1}{2}\nabla^2)\varphi_i + \int dr\, V_{ext}(r)n(r) + E_H[n] + E_{xc}[n]$$

where $n(r) = \sum_i |\varphi_i(r)|^2$, $E_H[n] = \frac{1}{2}\int dr dr' \frac{n(r)n(r')}{|r-r'|}$ and $E_{xc}[n]$ represent the exchange and correlation interaction. The exchange and correlation interactions are unknown functionals of n which become the difficult part within KS DFT.

2.2.3. Exchange correlation approximation

The major problem of the KS DFT is that the exact expression of the exchange-correlation functional is unknown. Therefore, approximations to express exchange-correlation functional have been proposed.

The simplest approximation is the local-density approximation (LDA). In this approximation, the exchange-correlation functional is expressed as

$$E_{xc}^{LDA}[n] = \int dr n(r)\varepsilon_{xc}(n(r))$$

where $\varepsilon_{xc}(n(r))$ is the energy per electron at position r that is the only function of electron density at position r. In the LDA, the exchange-correlation interaction at position r is only affected by the electron density at the same position. This leads to the tendency of underestimate the exchange energy and overestimate the correlation energy. The errors raise from the exchange and correlation parts could compensate each other to a certain degree. Therefore, LDA is very successful for homogeneous electron gas systems. However, for those inhomogeneous systems, LDA tends to overestimate the bond strength.

In order to obtain better prediction, people introduced the gradient of the density term to account for the nonhomogeneous of electron density. Therefore, the approximation allowed to account for the contribution of the electron density away from the position. These approximations are referred to as generalized gradient approximations (GGA) and have the form of:

$$E_{xc}^{LDA}[n] = \int drn(r)\varepsilon_{xc}(\nabla n(r)).$$

Using the GGA, great predictions for molecular geometries and ground-state properties have been achieved. There are different versions of GGA functional, the Perdew-Burke-Ernzerhof (PBE[1]) version is one of the most popular versions.

2.2.4. Pseudopotentials (PP) and Projected Augmented Wave (PAW) method

The electrons in the inner shell are strongly bound by the nucleus and do not significantly affect the chemical bonding of the atoms. The chemical binding properties are mostly determined by the valence electrons. Also, the all-electron potential is not computationally efficient. Therefore, it is reasonable to reduce the atom to an ionic core that interacts with the valence electrons. Based on this, an effective potential, a pseudopotential is proposed to attempt to replace the complicated effect of the core electrons. This concept largely reduces the computational effort without missing the essential physics.

The valence wavefunctions tend to exhibit rapid oscillations near the ion core. An accurate description of this area would require many Fourier components. The projected augmented wave (PAW) method was proposed to solve this issue by applying transforming operators to transform these rapidly oscillating wavefunctions into smooth wavefunctions

which are more computationally convenient.

2.3. vdW correction methods

Local and semilocal density functionals can't correctly describe the van der Waals interaction. The simplest way to correctly capture the van der Waals feature is to add a correction to the conventional Kohn-Sham energy:

$$E = E_{KS-DFT} + E_{vdw}$$

Among all the proposed correction methods, the DFT-D2 and DFT-D3 methods proposed by Grimme *et al*. are the most popular.

In the D2 method[2], the correction term can be calculated as:

$$E_{vdw} = -\frac{1}{2}\sum_{i=1}^{N_{at}}\sum_{j=1}^{N_{at}}\sum_{L}\frac{C_{6ij}}{r_{ij,L}^{6}} f_{d,6(r_{ij},L)}$$

where the summations are over all atoms and all translations of the units. For case L=0, i≠ j. The C_{6ij} term is the dispersion coefficient for atom pair i and j and the f(r) term is a damping function to scale the force field. The dispersion coefficient C_{6ij} is calculated as $C_{6ij} = \sqrt{C_{6ii}C_{6jj}}$. The value C_{6ii} varies among different elements, but insensitive to the particular chemical composition.

In the D3 method[3], the correction term is express as:

$$E_{vdw} = -\frac{1}{2}\sum_{i=1}^{N_{at}}\sum_{j=1}^{N_{at}}\sum_{L}\left(\frac{C_{6ij}}{r_{ij,L}^{6}} f_{d,6(r_{ij},L)} + \frac{C_{8ij}}{r_{ij,L}^{8}} f_{d,8(r_{ij},L)}\right)$$

Different from method D2, the dispersion coefficients are adjusted to the local geometry (coordination number) of atoms i and j.

In general, the DFT-D3 method provides better predictions for the van deer Waals

interaction, but in some cases, the D2 methods might give better results. For example, the *h*-WO_3 that is modeled in this thesis.

2.4. First principles Molecular dynamics (FPMD)

Molecular dynamics (MD) is a computational method for investigating the dynamic evolution of the system. The trajectory of the studied atoms and molecules is calculated from numerically solving Newton's equations of motion. All the atoms in the system are considered as massive, point-like particles.

In the first principles molecular dynamics (FPMD) method, the forces acting on each particle are calculated from the quantum mechanical wave function. The most commonly used two FPMD are Car-Parrinello molecular dynamics (CPMD)[6] and Born-Oppenheimer molecular dynamics(BOMD). Under the CPMD framework, the electrons are kept close to the ground state via fictitious dynamics to preventing the need for costly self-consistent iterative minimization. However, CPMD is limited in deal with metallic systems since the equation of motions of the CPMD is for full and equally occupied electronic states. In contrast to CPMD, BOMD treats electronic motion within the time-independent Schrödinger equation that the wavefunction is obtained via self-consistent iterative minimization. With the development of DFT algorithms, now in BOMD, after the convergence of the self-consistent field (SCF) cycle in the first step, the following steps only need several SCF cycles. In this thesis, we adopt BOMD since MXene is metallic.

References

1. Perdew, J. P.; Burke, K.; Ernzerhof, M., Generalized Gradient Approximation Made Simple. *Physical Review Letters* **1996,** *77* (18), 3865-3868.

2. Grimme, S., Semiempirical GGA-type density functional constructed with a long-range dispersion correction. **2006,** *27* (15), 1787-1799.

3. Grimme, S.; Antony, J.; Ehrlich, S.; Krieg, H., A consistent and accurate ab initio parametrization of density functional dispersion correction (DFT-D) for the 94 elements H-Pu. **2010,** *132* (15), 154104.

4. Hohenberg, P.; Kohn, W., Inhomogeneous Electron Gas. *Physical Review* **1964,** *136* (3B), B864-B871.

5. Kohn, W.; Sham, L. J., Self-Consistent Equations Including Exchange and Correlation Effects. *Physical Review* **1965,** *140* (4A), A1133-A1138.

6. Car, R.; Parrinello, M., Unified Approach for Molecular Dynamics and Density-Functional Theory. *Physical Review Letters* **1985,** *55* (22), 2471-2474.

Chapter 3. Proton Redox and Transport in MXene-Confined Water

3.1. Introduction

MXenes are a new family of 2D materials, consisting of transition metal carbides, nitrides, and carbonitrides with the general chemical formula of $M_{n+1}X_n$ (M=transition metal; X=C/N).[1-3] They can be synthesized via selective removal the main-group "A" element from the MAX phases by chemical etching in fluorine-containing acidic solutions. MXenes have been used as electrode materials for batteries,[4, 5] supercapacitors,[6, 7] and electrocatalysts.[8, 9] They are also explored for electronics[10, 11] and membrane[12, 13] applications.

Previous studies have shown that MXenes exhibit pseudocapacitance in the H_2SO_4 electrolyte.[14, 15] The proton-involved surface redox reaction has been found to be the key process to induce the pseudocapacitive behavior of MXene. Computational screening suggested new nitride-based MXenes for higher pseudocapacitance.[16] In aqueous solutions, it was found that the interlayer distance in MXene layers could expand due to the intercalation of water molecules and cations.[17-19] The intercalated water molecules raise the accessibility of proton to the surface redox reaction sites.

Despite the many recent reports of MXenes for pseudocapacitive energy storage in acidic electrolytes, the mechanism and dynamics of proton transfer in the intercalated water inside MXene layers is not well understood. In particular, one wonders how water under confinement and the water-layer thickness affect the mechanism of proton transfer and how the surface-redox process of the proton couples with the proton transport in water in the

context of the Grotthuss mechanism. Other important questions include: how can the transport and the system be optimized to enhance redox while not limiting transport? how can the proton-transfer mechanism be tuned by the electrode such as different surface terminations and by the electrolyte such as pH?

To begin to address the important questions above, here we employ first principles methods to examine the behavior of proton in different scenarios of interaction with a MXene layer, to provide a dynamic picture. We chose the prototypical MXene, Ti_3C_2,[15, 20] for which many experimental studies have been published in terms of its pseudocapacitive energy storage in the H_2SO_4 electrolyte. During chemical processing, the surface of Ti_3C_2 will be terminated by groups such as O, OH, or F (minor).[10] In this work, we will focus on the O termination which becomes OH when the MXene layer is reduced in the H_2SO_4 electrolyte. We use first principles molecular dynamics (FPMD) simulation to examine proton redox and transport in water confined inside $Ti_3C_2O_2$ layers. Our analysis of the FPMD trajectories focuses on the surface redox chemistry and the diffusion of protons within the hydrogen-bond network of confined water layers. Below we first describe the method details for our FMPD simulations.

3.2. Methods

Kohn-Sham Density functional theory (KS-DFT) implemented in the Vienna *ab initio* Simulation Package (VASP) was used for structure optimization and FPMD.[21] The generalized-gradient-approximation in the form of Perdew-Burke-Ernzerhof (PBE) functional was used for electron exchange-correlation in combination with DFT-D3 to account for van der Waals interactions.[22, 23] The electron-nuclei interaction was described

by projector augmented wave (PAW) potentials.[24] An energy cutoff of 500 eV was used for the plane-wave basis set. A k-point mesh of 3×3×1 was used for sampling the Brillouin zone. Convergence criteria were 10^{-5} eV in energy and 0.01 eV/Å in force for geometry optimization.

To model the MXene-water(proton)-MXene structure, we used an orthorhombic supercell (a=10.52 Å; b=9.11 Å) of the $Ti_3C_2O_2$ monolayer (12 formula units). Then three protons and different layers of water (one, two, three layers, corresponding to 10, 17, 26 water molecules per cell, respectively) were randomly inserted into the cell. The whole simulation cell is charge neutral, so there are extra electrons in the electrode to balance the proton charge in the water layer. Since about 0.5 H^+ per formula unit can be stored in MXenes such as $Ti_3C_2O_2$,[25] our use of three protons in 12 formula units simulates an early stage of the charging process. To determine the optimal interlayer spacing (the c parameter), we calculated the total energy as a function of the interlayer distance (see next section).

After an optimized interlayer spacing was obtained, FPMD simulations were performed in canonical ensemble (NVT) with Nosé-thermostat at 300 K for 16 ps (with a time step of 1 fs).[26-28] The system was considered well equilibrated when the temperature stabilized, which was usually achieved after a few ps. From the time-dependent trajectory of O_0 (oxygen atom bonded with proton), we can obtain its time-dependent mean square displacement (MSD):

$$\mathrm{MSD}(\Delta t) = \langle |\vec{r}(t_0 + \Delta t) - \vec{r}(t_0)|^2 \rangle = \frac{1}{N_t - m} \sum_{k=0}^{N_t - m - 1} \langle |\vec{r}(k + m) - \vec{r}(k)|^2 \rangle$$

where $\vec{r_i}$ represents the position of the particle, m is the number of snapshots for Δt, and N_t is the total number of snapshots. To evaluate the contribution from different directions, we also decomposed the MSD to xy plane and z direction by projecting the position to the relative direction. The diffusion coefficients were obtained by using the Einstein relation, $D = \frac{1}{6}\frac{\partial(MSD)}{\partial t}$. Proton diffusion in bulk water was also simulated by a cubic unit cell of 12.36 Å in length containing 63 water molecules and one proton.

3.3. Results and discussion

The interlayer spacing is a key parameter for water/proton confinement between MXene layers. To further understand the degree of confinement on the proton transfer, the water layer is a key variable that we address here. Below we first determine the interlayer spacings for the different water layers in confinement.

3.3.1. Proton and water confined in $Ti_3C_2O_2$ layers

Experimental observation showed that the interlayer distance increases with water intercalated between MXene layers.[19] Before modeling the proton transport in such system, we first determine the optimal interlayer spacing as the thickness of the intercalated water is varied. We used an orthorhombic unit cell of the $Ti_3C_2O_2$ monolayer and added different layers of water with three protons randomly distributed between the two $Ti_3C_2O_2$ monolayers (Figure 3.1). Here we chose the O-termination for the MXene because as protons get reduced on the surface, some O terminal groups will be converted to OH groups. In other words, the O- and OH- terminations are inter-convertible under the acidic electrolyte.[25]

For each different number of water layers, we optimized the structure as a function

of the interlayer distance to determine the interlayer spacing with the lowest energy. As shown in Figure 3.2, the optimal interlayer spacing is 12.5 Å, 15.0 Å, and 18.0 Å for one, two, and three confined water layers, respectively. We estimated the densities of the confined water layers and found them to be close to 1 in the cases of two and three layers (1.02 and 0.99 $g \cdot cm^{-3}$, respectively). In the case of the one-layer water, the strong interfacial interaction made the water density greater than 1 (1.15 $g \cdot cm^{-3}$). With these optimal interlayer spacings, we next performed FPMD simulations.

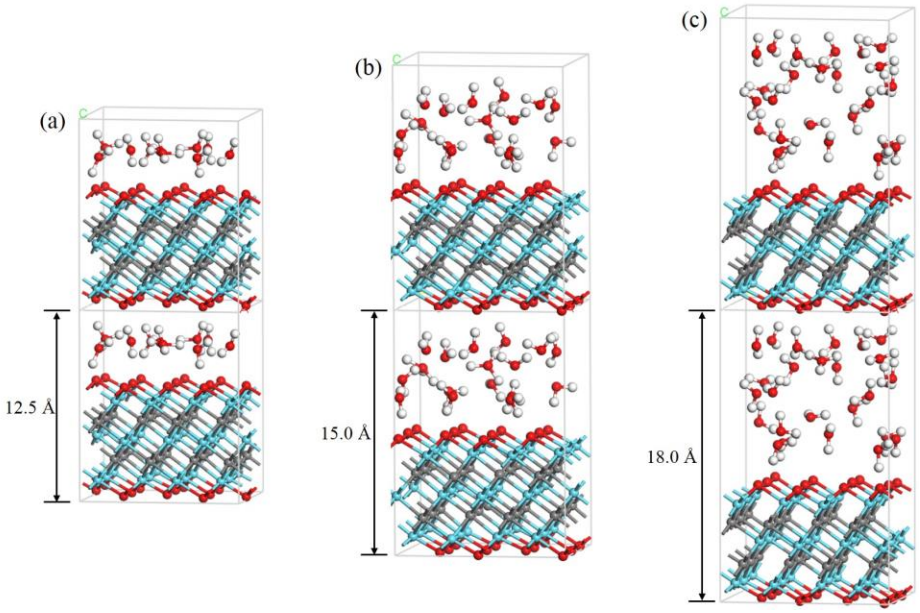

Figure 3.1. Optimized structures of protons confined in $Ti_3C_2O_2$ with different layers of water molecules: (a) one; (b) two; (c) three layers. Ti, cyan; C, gray; O, red; H, white.

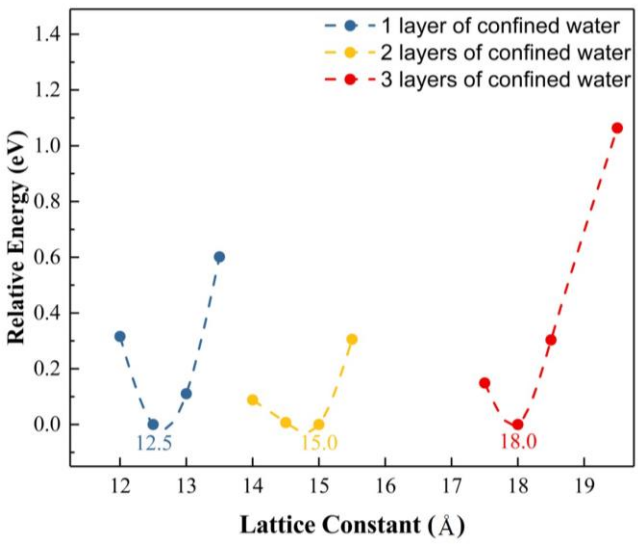

Figure 3.2. Relative energy as a function of c lattice parameter of $Ti_3C_2O_2$ with confined water and proton. A spline is used to connect the points for each case.

3.3.2. Proton redox and transport in water confined between $Ti_3C_2O_2$ layers

The FPMD simulations in the NVT ensemble at 300 K have been run for about 16ps for the three systems with three different numbers of water layers and the same number of protons. During the simulation timescale, we observed reversible surface redox processes for all three systems whereby a proton in the hydronium ion (H_3O^+) transfers to a surface O atom on $Ti_3C_2O_2$ and form a hydroxyl at the MXene-water interface. The typical snapshots of such reversible surface redox processes for the three models are shown in Figure 3.3. Since in all three cases proton transfer happened frequently and reversibly, the initial positions of the three protons did not affect the proton behavior much. By inspecting the FPMD trajectories, we also found that the proton surface-redox processes can take place on the different O sites on the $Ti_3C_2O_2$ surface, mediated with proton transfer events in the water layer.

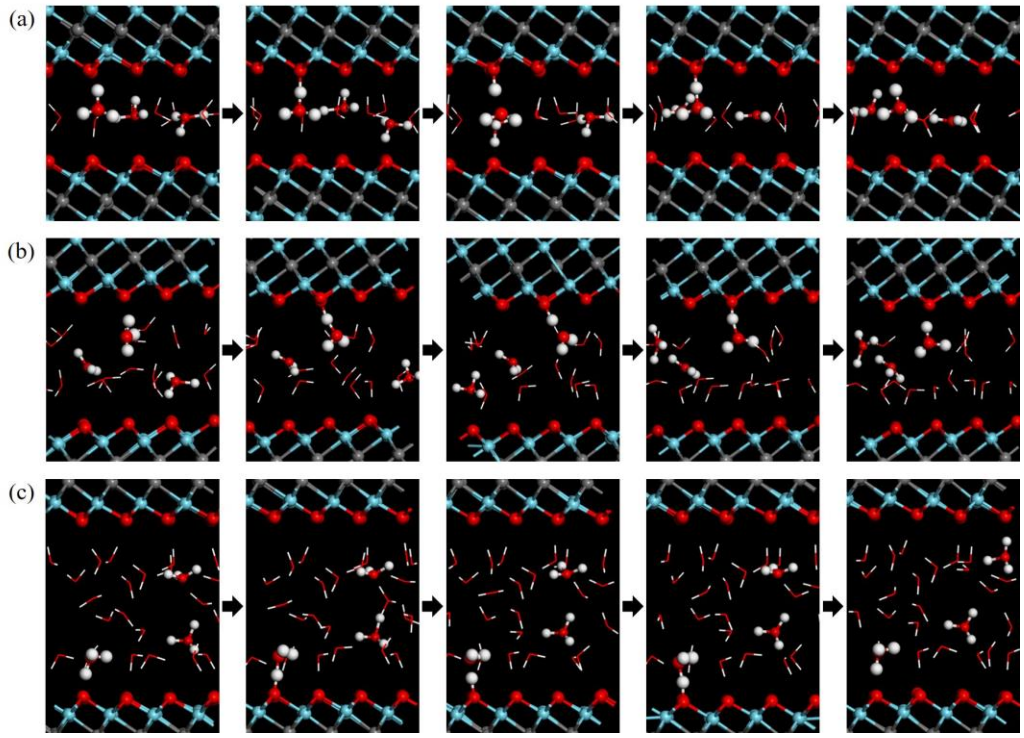

Figure 3.3. Snapshots of typical proton surface-redox processes in water confined between $Ti_3C_2O_2$ layers: (a) one layer; (b) two layers; (c) three layers of confined water. The interfacial water/H^+ involved in the surface-redox process and the hydronium ions are highlighted by a ball-and-stick model. Cyan, Ti; gray, C; red, O; white, H.

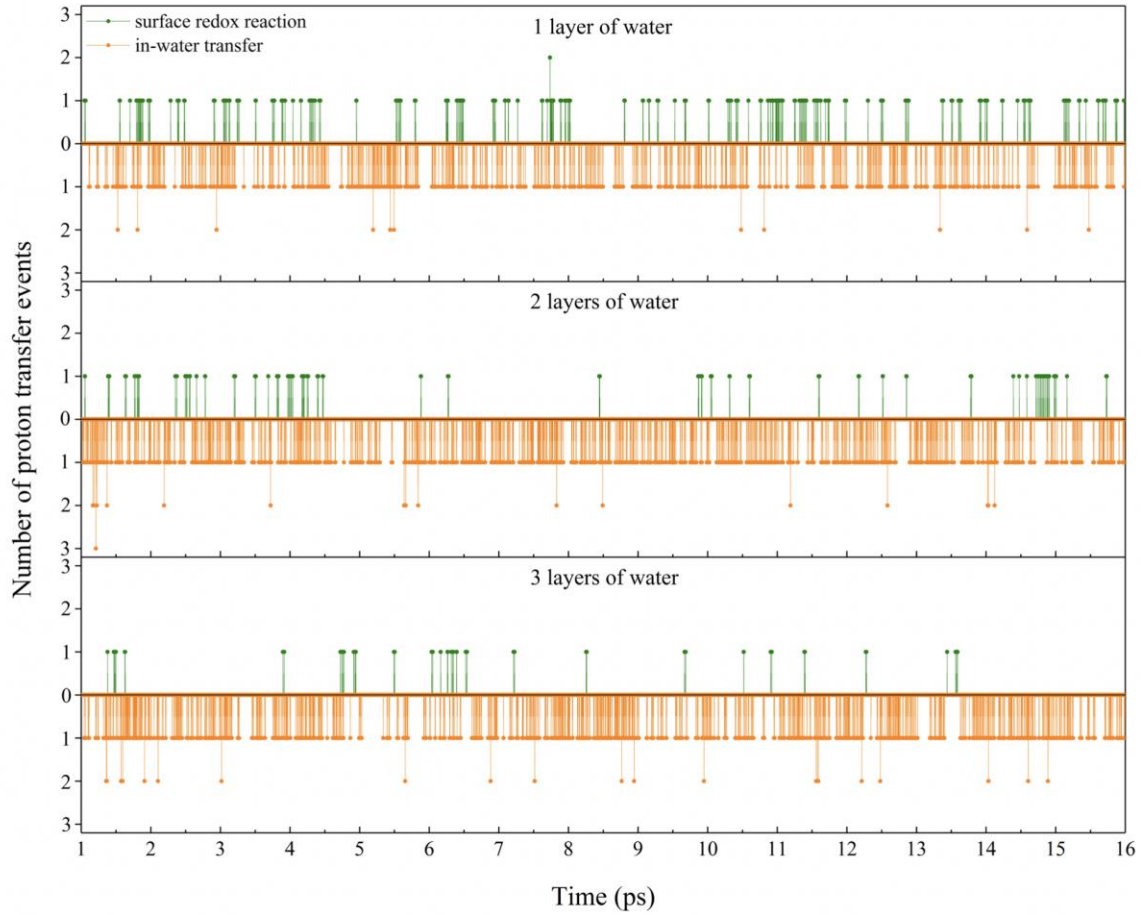

Figure 3.4. Number of proton surface redox (green) vs. in-water proton transfer (orange) events with time for different layers of water with protons confined between $Ti_3C_2O_2$ layers.

By counting the proton transfer events (surface redox vs. in-water transport) happened along the trajectory (Figure 3.4), we found that, regardless of the number of confined water layer, the in-water proton transfer events happened much more frequently than the surface redox reaction. We estimated the rate constants of the proton surface-redox process and found that it decreases with the number of water layers confined (Figure 3.5(a)). What is interesting is that the rate constant is much higher in the case of one-layer water than in the two or three layers of water. This is due to the higher chances of protons

in water to encounter the MXene surfaces when the thinner layer of water molecules is confined between the two MXene layers. Especially in the case of one layer, the water molecules and hydronium ions are now interacting with both $Ti_3C_2O_2$ surfaces. But in the case of two layers, the top layer interacts with the top surface while the bottom layer with bottom surface; in the case of three layers, the middle water layer is not directly interacting with either of the two $Ti_3C_2O_2$ surfaces. This picture of increasing interfacial $Ti_3C_2O_2/H_2O/H^+/Ti_3C_2O_2$ interactions as the number of the water layers confined becomes thinner and thinner is also consistent with lower coordination of water molecules around the hydronium ion for the thinner layers of water (Figure 3.5(b)). In other words, as the water becomes thinner from three layers to one layer, the interfacial interaction becomes stronger and the hydronium ion becomes less solvated by water molecules.

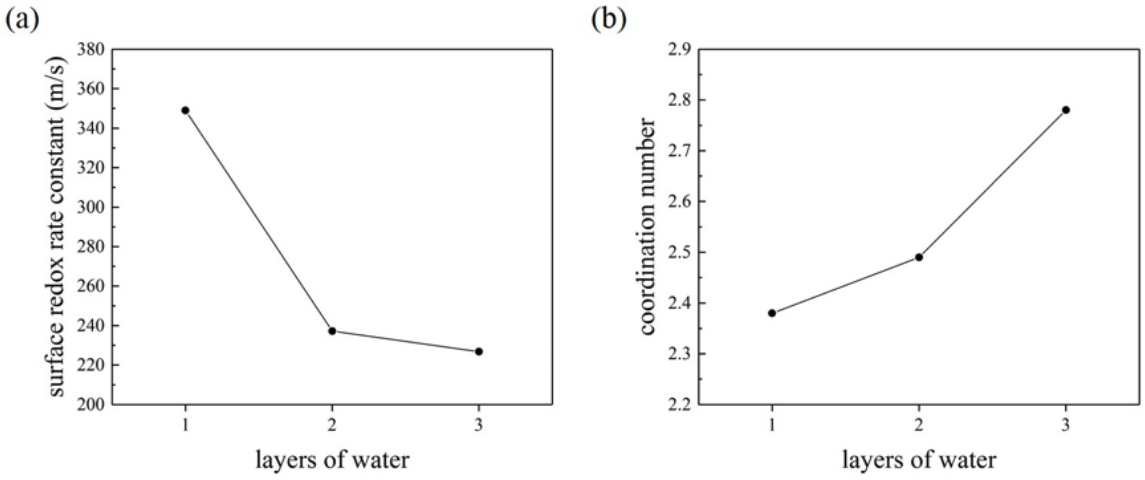

Figure 3.5. Proton surface redox rate constant (a) and average number of water molecules hydrogen-bonded to the hydronium ion (b) for different layers of water with protons confined in $Ti_3C_2O_2$ layers.

3.3.1. Mechanism of proton transport in water confined between $Ti_3C_2O_2$ layers

Mechanism of proton transfer in water has been extensively investigated in the past

decades via various spectroscopic techniques and computer simulations. Here we wonder how different proton transfer is in confined water from in bulk water. Following the notation from the literature,[29] we define the O atom in the hydronium ion as O_0 and its nearest O atom in the first coordination shell as O_{1x} atom; the O_0 - O_{1x} interaction is called a special pair (Figure 3.6). In Figure 3.7 (upper panel), we display the change of identity of O_0 and O_{1x} during a trajectory of 0.5 ps which signals proton-transfer events. During the 'short' segments, the O_0 identity is short-lived and switches back-and-forth with the O_{1x} identity; during the 'long' segments, the O_0 identity is long-lived but the O_{1x} identity change among three different O atoms. As a previous study proposed,[29] the short segments correspond to the Zundel state in which the O_0 and O_{1x} atoms share the proton and the O_0-H and O_{1x}-H bond lengths are close (Figure 3.7 lower panel). The 'long' segments correspond to the Eigen state of the hydronium ion coordinated by three water molecules in the first coordination shell, and the three O_1 atoms do the so-called 'special pair dance' whereby the identity of the O atom closest to O_0 (i.e., O_{1x}) switches among the three water molecules in the first coordination shell (Figure 3.6).[29] In this case the O_0-H bond is much shorter than the O_{1x}-H bond (Figure 3.7 lower panel). Taken together, Figure 3.7 shows that proton transfer follows the same Eigen-Zundel-Eigen mechanism in MXene-confined water as in bulk water.

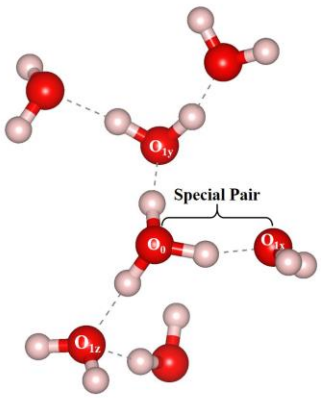

Figure 3.6. Typical solvation structure of hydronium ion in water. The O atom in the hydronium ion is label as O_0; the O atoms in the first coordination shell are labeled as O_1: the closest labeled as O_{1x}, the other two labeled as O_{1y} and O_{1z}. The special pair refers to O_0 and O_{1x}.

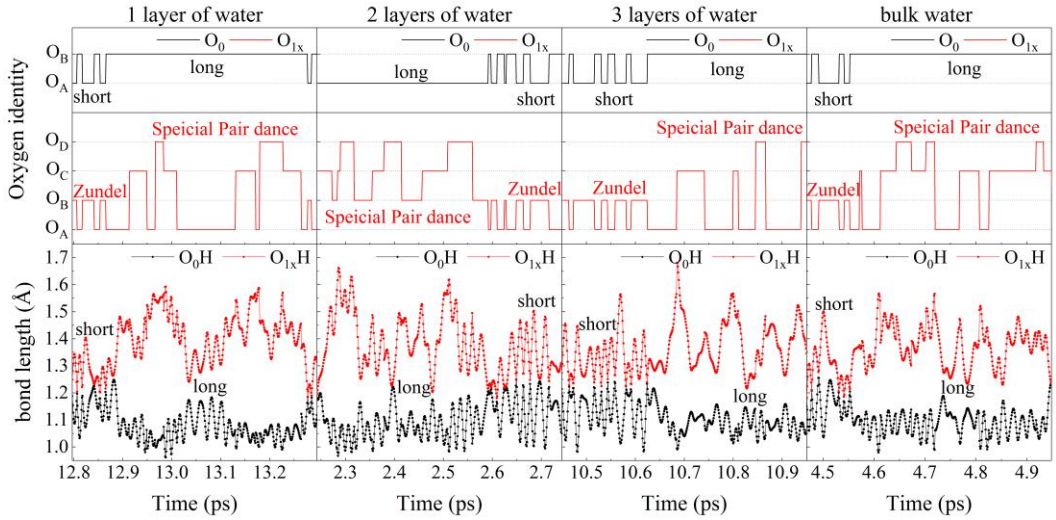

Figure 3.7. Change of O_0 and O_{1x} identity (upper panel) and their O-H bond lengths (lower panel) with time during a typical in-water proton-transfer event. The 'long' or 'short' labels refer to the relative duration of the O_0 identity. O_A, O_B, O_C, and O_D represent different water oxygen atoms. "Special Pair dance" refers to the correlated motion whereby the identity of the O_{1x} around O_0 switches among the three water molecules in the first coordination shell of O_0 (Figure 3.6).

3.3.2. Proton diffusivity in water confined between $Ti_3C_2O_2$ layers

After revealing the mechanism of proton transfer in the confined water, we next

quantify its mobility. Figure 3.7 shows that the key to proton transfer is the changing of the O_0 identity, namely, the O atom in the hydronium ion (Figure 3.6). To track the proton motion in the water layer, we therefore computed the MSD of the O_0 atoms and further decomposed the MSD into the xy-plane and the z-direction, as shown in Figure 3.8 (a).

The simulated diffusion coefficients from MSD for protons in the confined water layers are shown in Figure 3.8 (b). For comparison, we also simulated proton transport in bulk water (with the same FPMD method). Our simulated diffusion coefficient for proton in bulk water is $9.09 \pm 2.25 \times 10^{-9}$ $m^2 \cdot s^{-1}$, comparable to a previous simulation with the PBE[30] functional and the experimental value[31] of 9.31×10^{-9} $m^2 \cdot s^{-1}$. The simulated diffusion coefficients for protons in $Ti_3C_2O_2$-confined water are all lower than in bulk water. In the case of the three layers of water, the simulated value is 5.56×10^{-9} $m^2 \cdot s^{-1}$. This value further decreases to 2.98×10^{-9} $m^2 \cdot s^{-1}$ for the two-layer water and 1.59×10^{-9} $m^2 \cdot s^{-1}$ for the one-layer water. The proton transport becomes slower as the interaction between the water layer and the MXene surfaces becomes stronger.

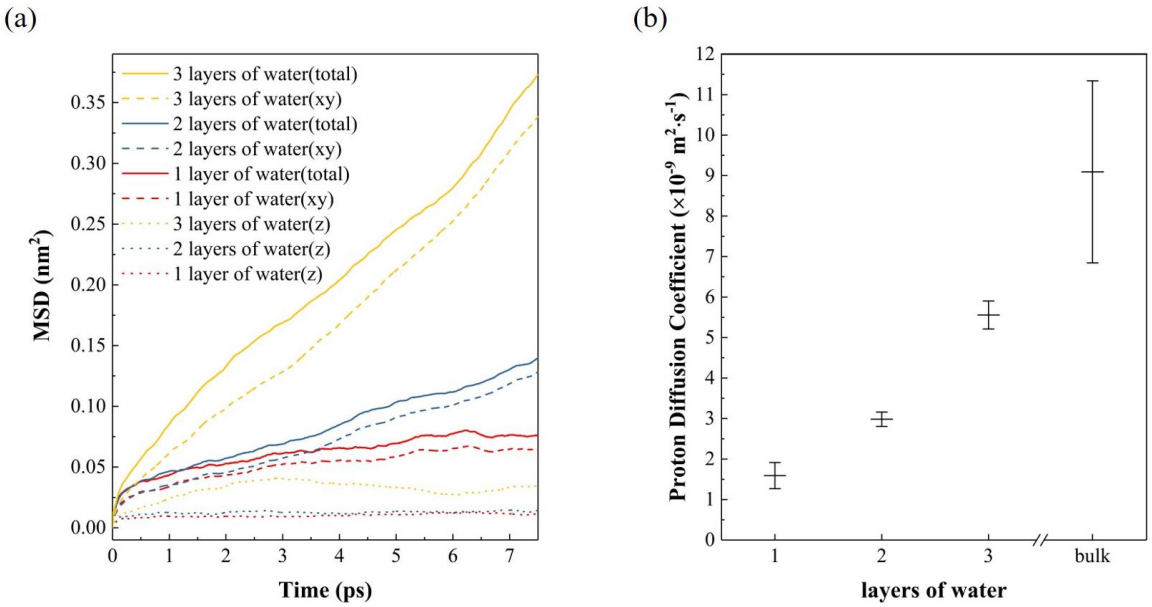

Figure 3.8. Proton diffusion in $Ti_3C_2O_2$-confined water layers: (a) total and decomposed mean-square displacement (MSD) of the O_0 atom; (b) proton diffusion coefficients for different number of water layers (value in bulk water included for comparison).

Figure 3.8 (a) shows that proton transfer is 2D-like for the three different thicknesses of the water layer. The interfacial interaction from the confinement plays a more significant role in slowing down the proton transfer in the cases of one layer and two layers of water, where all the water molecules are directly interacting with the electrode surfaces. In the case of three layers of water, there is now a water layer not interacting with the two electrode surfaces directly. In this case, although it is still 2D-like, the proton mobility is much higher and approaches that in bulk water (Figure 3.8 (b)). We expect that the proton transfer will become more 3D-like as the water layer thickness further increases. A simple extrapolation indicates that five layers of water would yield a proton diffusion coefficient about the same as that in the bulk water.

3.3.3. Comparison with the experiment and implications from our simulations

Recently, Mu *et al*. investigated the charging mechanism of the $Ti_3C_2T_x$ electrode

in 1M H_2SO_4 using in situ X-ray diffraction.[19] They found that the interlayer spacing expands and shrinks during charge and discharge cycles by about 0.5 Å and in the charged state, the interlayer spacing (as defined in Figure 3.1) expands to 14.3 Å. This is very close to the case of the intercalated protons with two layers of water in between $Ti_3C_2O_2$ layers in our simulations where we found the equilibrium interlayer spacing is 15.0 Å. So our simulations indicate that when cycling the $Ti_3C_2T_x$ electrode in 1M H_2SO_4 as explored by Mu *et al*., there are two layers of water solvent in between $Ti_3C_2O_2$ layers. Moreover, our findings suggest that once protons are intercalated into the water layer confined between the $Ti_3C_2T_x$ layers, both proton surface redox and in-water proton transfer are fast, despite that proton transfer is slowed down after confinement. Hence the bottleneck for the charging process could be the intercalating step, namely, how the protons migrate from the bulk electrolyte into the MXene galleries via the edges of the MXene layers. In addition, during our simulations, we fixed the interlayer spacing, since our models simulated a charged state where the protons are already in between MXene layers; by simulating the intercalation process, one can address the change of interlayer spacing during cycling where one allows the interlayer spacing to vary under an applied potential during a constant-stress simulation. We hope to address this question in a future study.

It is important to note that whether or not there is the intercalated water in MXene layers often depends on the preparation protocol.[17, 32] Moreover, the presence of water molecules in MXene layers has been attributed to co-intercalation of ions such as Li^+. Depending on the hydrophilicity of the intercalated metal ions, the amount of water confined between MXene layers could vary significantly and its diffusivity could be

affected greatly,[32, 33] which might further impact the proton's diffusivity if an acidic electrolyte is used. In this case, it is desirable to examine how the co-existent cations such as alkali ions play a role in the redox and transport behavior of protons in MXene layers. Further exploration is warranted.

3.4. Conclusions

Using first-principles molecular dynamics (FPMD) simulations, we revealed the mechanisms of proton redox at the $Ti_3C_2O_2$/water interfaces coupled with proton transfer in thin water layers confined between $Ti_3C_2O_2$ surfaces. We especially focused on the effect of the thickness of the water layer. Close to 20 ps of simulations at room temperature found that the proton redox process happens reversibly between surface -O sites and water molecules at the interfaces. In between proton surface redox events, more frequent in-water proton transfer events were observed. As the confined water layer becomes thinner and thinner from three layers to one layer, proton's surface redox rate increases, especially by a greater extent from two layers to one layer, but the in-water proton-transfer rate decreases. In the much less confined case of three layers of water, the proton mobility already approaches the bulk value. We further revealed that proton transfer still follows the Eigen-Zundel-Eigen mechanism in the 2D-like confined water (regardless of the thickness) as in the 3D bulk water via the special-pair dance. Comparison with recent experiment indicates that our models resemble closely the charged state of the $Ti_3C_2O_2$ electrode in H_2SO_4 especially in the case of two layers of water. Moreover, our findings suggest that once protons are intercalated into the water layer confined between the $Ti_3C_2T_x$ layers, both proton surface redox and in-water proton transfer are fast. The fast surface redox and

transfer processes for the intercalated protons as seen in our FPMD simulations imply that other processes are likely the bottleneck for the ionic transport and the charging process, such as the intercalating step whereby the protons migrate from the bulk electrolyte into the MXene galleries via the edges of the MXene layers.

References

1. Naguib, M.; Kurtoglu, M.; Presser, V.; Lu, J.; Niu, J.; Heon, M.; Hultman, L.; Gogotsi, Y.; Barsoum, M. W., Two-Dimensional Nanocrystals Produced by Exfoliation of Ti_3AlC_2. **2011,** *23* (37), 4248-4253.

2. Naguib, M.; Mashtalir, O.; Carle, J.; Presser, V.; Lu, J.; Hultman, L.; Gogotsi, Y.; Barsoum, M. W., Two-Dimensional Transition Metal Carbides. *ACS Nano* **2012,** *6* (2), 1322-1331.

3. Anasori, B.; Lukatskaya, M. R.; Gogotsi, Y., 2D metal carbides and nitrides (MXenes) for energy storage. *Nature Reviews Materials* **2017,** *2* (2), 16098.

4. Liang, X.; Garsuch, A.; Nazar, L. F., Sulfur Cathodes Based on Conductive MXene Nanosheets for High-Performance Lithium–Sulfur Batteries. **2015,** *54* (13), 3907-3911.

5. Ahmed, B.; Anjum, D. H.; Hedhili, M. N.; Gogotsi, Y.; Alshareef, H. N., H_2O_2 assisted room temperature oxidation of Ti2C MXene for Li-ion battery anodes. *Nanoscale* **2016,** *8* (14), 7580-7587.

6. Yan, J.; Ren, C. E.; Maleski, K.; Hatter, C. B.; Anasori, B.; Urbankowski, P.; Sarycheva, A.; Gogotsi, Y., Flexible MXene/Graphene Films for Ultrafast Supercapacitors with Outstanding Volumetric Capacitance. **2017,** *27* (30), 1701264.

7. Li, H.; Hou, Y.; Wang, F.; Lohe, M. R.; Zhuang, X.; Niu, L.; Feng, X., Flexible All-Solid-State Supercapacitors with High Volumetric Capacitances Boosted by Solution Processable MXene and Electrochemically Exfoliated Graphene. **2017,** *7* (4), 1601847.

8. Seh, Z. W.; Fredrickson, K. D.; Anasori, B.; Kibsgaard, J.; Strickler, A. L.; Lukatskaya, M. R.; Gogotsi, Y.; Jaramillo, T. F.; Vojvodic, A., Two-Dimensional Molybdenum Carbide (MXene) as an Efficient Electrocatalyst for Hydrogen Evolution. *ACS Energy Letters* **2016,** *1* (3), 589-594.

9. Zhou, S.; Yang, X.; Pei, W.; Liu, N.; Zhao, J., Heterostructures of MXenes and N-doped graphene as highly active bifunctional electrocatalysts. *Nanoscale* **2018,** *10* (23), 10876-10883.

10. Tang, Q.; Zhou, Z.; Shen, P., Are MXenes Promising Anode Materials for Li Ion Batteries? Computational Studies on Electronic Properties and Li Storage Capability of Ti_3C_2 and $Ti_3C_2X_2$ (X = F, OH) Monolayer. *Journal of the American Chemical Society* **2012,** *134* (40), 16909-16916.

11. Anasori, B.; Shi, C.; Moon, E. J.; Xie, Y.; Voigt, C. A.; Kent, P. R. C.; May, S. J.; Billinge, S. J. L.; Barsoum, M. W.; Gogotsi, Y., Control of electronic properties of 2D carbides (MXenes) by manipulating their transition metal layers. *Nanoscale Horizons* **2016,**

1 (3), 227-234.

12. Ding, L.; Wei, Y.; Wang, Y.; Chen, H.; Caro, J.; Wang, H., A Two-Dimensional Lamellar Membrane: MXene Nanosheet Stacks. **2017,** *56* (7), 1825-1829.

13. Ding, L.; Wei, Y.; Li, L.; Zhang, T.; Wang, H.; Xue, J.; Ding, L.-X.; Wang, S.; Caro, J.; Gogotsi, Y., MXene molecular sieving membranes for highly efficient gas separation. *Nature Communications* **2018,** *9* (1), 155.

14. Lukatskaya, M. R.; Bak, S.-M.; Yu, X.; Yang, X.-Q.; Barsoum, M. W.; Gogotsi, Y., Probing the Mechanism of High Capacitance in 2D Titanium Carbide Using In Situ X-Ray Absorption Spectroscopy. **2015,** *5* (15), 1500589.

15. Lukatskaya, M. R.; Kota, S.; Lin, Z.; Zhao, M.-Q.; Shpigel, N.; Levi, M. D.; Halim, J.; Taberna, P.-L.; Barsoum, M. W.; Simon, P.; Gogotsi, Y., Ultra-high-rate pseudocapacitive energy storage in two-dimensional transition metal carbides. *Nature Energy* **2017,** *2* (8), 17105.

16. Zhan, C.; Sun, W.; Kent, P. R. C.; Naguib, M.; Gogotsi, Y.; Jiang, D.-e., Computational Screening of MXene Electrodes for Pseudocapacitive Energy Storage. *The Journal of Physical Chemistry C* **2019,** *123* (1), 315-321.

17. Muckley, E. S.; Naguib, M.; Wang, H.-W.; Vlcek, L.; Osti, N. C.; Sacci, R. L.; Sang, X.; Unocic, R. R.; Xie, Y.; Tyagi, M.; Mamontov, E.; Page, K. L.; Kent, P. R. C.; Nanda, J.; Ivanov, I. N., Multimodality of Structural, Electrical, and Gravimetric Responses of Intercalated MXenes to Water. *ACS Nano* **2017,** *11* (11), 11118-11126.

18. Ghidiu, M.; Halim, J.; Kota, S.; Bish, D.; Gogotsi, Y.; Barsoum, M. W., Ion-Exchange and Cation Solvation Reactions in Ti_3C_2 MXene. *Chemistry of Materials* **2016,** *28* (10), 3507-3514.

19. Mu, X.; Wang, D.; Du, F.; Chen, G.; Wang, C.; Wei, Y.; Gogotsi, Y.; Gao, Y.; Dall'Agnese, Y., Revealing the Pseudo-Intercalation Charge Storage Mechanism of MXenes in Acidic Electrolyte. **2019,** *29* (29), 1902953.

20. Er, D.; Li, J.; Naguib, M.; Gogotsi, Y.; Shenoy, V. B., Ti_3C_2 MXene as a High Capacity Electrode Material for Metal (Li, Na, K, Ca) Ion Batteries. *ACS Applied Materials & Interfaces* **2014,** *6* (14), 11173-11179.

21. Kresse, G.; Furthmüller, J., Efficient iterative schemes for ab initio total-energy calculations using a plane-wave basis set. *Physical Review B* **1996,** *54* (16), 11169-11186.

22. Perdew, J. P.; Burke, K.; Ernzerhof, M., Generalized Gradient Approximation Made Simple. *Physical Review Letters* **1996,** *77* (18), 3865-3868.

23. Grimme, S.; Antony, J.; Ehrlich, S.; Krieg, H., A consistent and accurate ab initio parametrization of density functional dispersion correction (DFT-D) for the 94 elements H-Pu. **2010,** *132* (15), 154104.

24. Blöchl, P. E., Projector augmented-wave method. *Physical Review B* **1994,** *50* (24), 17953-17979.

25. Zhan, C.; Naguib, M.; Lukatskaya, M.; Kent, P. R. C.; Gogotsi, Y.; Jiang, D.-e., Understanding the MXene Pseudocapacitance. *The Journal of Physical Chemistry Letters* **2018,** *9* (6), 1223-1228.

26. Nosé, S., A unified formulation of the constant temperature molecular dynamics methods. **1984,** *81* (1), 511-519.

27. Shuichi, N., Constant Temperature Molecular Dynamics Methods. *Progress of Theoretical Physics Supplement* **1991,** *103*, 1-46.

28. Bylander, D. M.; Kleinman, L., Energy fluctuations induced by the Nos'e thermostat. *Physical Review B* **1992,** *46* (21), 13756-13761.

29. Markovitch, O.; Chen, H.; Izvekov, S.; Paesani, F.; Voth, G. A.; Agmon, N., Special Pair Dance and Partner Selection: Elementary Steps in Proton Transport in Liquid Water. *The Journal of Physical Chemistry B* **2008,** *112* (31), 9456-9466.

30. Chen, M.; Zheng, L.; Santra, B.; Ko, H.-Y.; DiStasio Jr, R. A.; Klein, M. L.; Car, R.; Wu, X., Hydroxide diffuses slower than hydronium in water because its solvated structure inhibits correlated proton transfer. *Nature Chemistry* **2018,** *10* (4), 413-419.

31. Light, T. S.; Licht, S.; Bevilacqua, A. C.; Morash, K. R., The Fundamental Conductivity and Resistivity of Water. *Electrochemical and Solid-State Letters* **2005,** *8* (1), E16.

32. Osti, N. C.; Naguib, M.; Ostadhossein, A.; Xie, Y.; Kent, P. R. C.; Dyatkin, B.; Rother, G.; Heller, W. T.; van Duin, A. C. T.; Gogotsi, Y.; Mamontov, E., Effect of Metal Ion Intercalation on the Structure of MXene and Water Dynamics on its Internal Surfaces. *ACS Applied Materials & Interfaces* **2016,** *8* (14), 8859-8863.

33. Yao, Y.; Kanai, Y.; Berkowitz, M. L., Role of Charge Transfer in Water Diffusivity in Aqueous Ionic Solutions. *The Journal of Physical Chemistry Letters* **2014,** *5* (15), 2711-2716.

Chapter 4. MXene in water-in-salt electrolytes

4.1. Introduction

Faradaic reduction-oxidation (redox) reactions and the electrostatic formation of electrical double-layers (EDLs) are used to store charge in batteries and EDL capacitors (EDLCs, or supercapacitors), respectively. More recently, materials that exhibit continuous surface redox reactions across a wide range of potentials, known as pseudocapacitive materials, have attracted attention as a way to increase the energy density of supercapacitors with minimal decreases in their power and cycle life. To distinguish between these charge storage mechanisms, electrochemists will primarily use the shape of cyclic voltammograms (CVs).[1] EDL formation results in a rectangular CV, where the amount of charge stored varies linearly as a function of potential. On the other hand, CVs with sharp peaks that have clear separation between the potentials of the oxidative and reductive reactions represent a Faradaic, or battery-type, process. In the case of surface or intercalation pseudocapacitance, either an EDL-like rectangular CV, like in the case of RuO_2 and MnO_2, or a broad and electrochemically reversible redox wave with a minimal separation between oxidation and reduction peaks is overlaid on a capacitive envelope, e.g., for titanium carbide MXene in protic electrolytes.[2, 3] The CVs of pseudocapacitive materials may also have an expanded envelope within the potential range of the redox processes, like in Nb_2O_5 in Li based organic electrolytes[4] or Cl-terminated MXene in LP30 electrolyte.[5] It is important to mention that in all these cases the charge storage mechanism depends not only on the electrode material, but also on the electrolyte used.[6] Water-in-salt

(WIS) electrolytes have attracted significant attention in recent years because of their ability to suppress hydrogen evolution and electrode oxidation, expand the voltage window, and enable high-voltage aqueous lithium-ion chemistries without use of flammable organic solvents.[7] Two-dimensional (2D) transition metal carbides and nitrides (MXenes) have shown EDL-like charge storage in neutral electrolytes and redox storage in acidic electrolytes[8], but the electrochemical behavior of MXenes in WIS electrolytes has not been deeply investigated yet. Here we investigated $Ti_3C_2T_x$ (where T_x stands for surface terminations like =O, –OH, –Cl, and –F) MXene with increased chemical stability produced using an improved synthesis process (Methods) in several WIS Li-ion electrolytes to reach the range of anodic potentials that was previously inaccessible for MXenes and determined the charge storage capabilities and mechanisms of $Ti_3C_2T_x$ in WIS electrolytes with wide voltage windows.

4.2. Details of the density functional theory (DFT) simulations

DFT calculations were performed with the Vienna *ab initio* Simulation Package (VASP).[9] The Perdew-Burke-Ernzerhof (PBE) functional of generalized gradient approximation (GGA) was employed for electron exchange correlation.[10] Projector augmented-wave (PAW) potentials were adopted for nuclei-electron interaction.[11] A plane-wave basis set with the kinetic energy cutoff of 500 eV was utilized for the valence electrons. DFT-D3 method was employed to account for van der Waals interactions.[12] Supercells containing 12 $Ti_3C_2O_2$ formula units were adopted to model MXene with different interfacial compositions. A k-point mesh of 2×2×2 was used for sampling the Brillouin zone. The convergence criteria were set to 10^{-5} eV in energy and 0.01 eV/Å in

force. To determine the d-spacing, we optimized the structure as a function of the c lattice parameter. The total energy vs. c was then fitted by a cubic polynomial function and the minimum of the fitted function was determined as the optimal d-spacing. Based on the experimental accumulated charge through the cathodic scan of a three-electrode Swagelok cell, the number of inserted Li^+ per unit of $Ti_3C_2T_x$ was estimated (assuming each inserted Li+ contributed to one charge).

The Li differential insertion energy can be obtained as:

$$\Delta G = E[Ti_3C_2O_2 \cdot y_{final}H_2O \cdot x_{final}lLi] - E[Ti_3C_2O_2 \cdot y_{initial}H_2O \cdot x_{initial}Li] - (y_{final} - y_{initial})\mu[H_2O] - (x_{final} - x_{initial})E[Li].$$

Here we assume $\mu[H_2O]$ of liquid water is equal to the $\mu[H_2O]$ of the water vapor at saturated vapor pressure.[13, 14] The corresponding intercalation voltage referenced to standard lithium electrode was calculated as

$$V = -\Delta G/e,$$

and then converted to Ag/AgCl electrode referenced according to standard electrode potential database.

4.3. Activated electrochemical process

Figure 4.1 (a) shows CVs of a vacuum-filtered $Ti_3C_2T_x$ MXene film in 3 M H_2SO_4 and three WIS electrolytes, specifically 19.8 m (mol/kg water) lithium chloride (LiCl), 19.2 m lithium bromide (LiBr), and 15 m lithium bis(trifluoromethanesulfonyl)-imide (LiTFSI) aqueous electrolytes. $Ti_3C_2T_x$ is typically used as a negative electrode material in aqueous systems as $Ti_3C_2T_x$ is oxidized beyond 0.1-0.2 V *vs* Ag/AgCl.[12,13] When a WIS electrolyte is used, the stable electrochemical potential window for $Ti_3C_2T_x$ is extended to 0.7 - 0.9 V

vs Ag (an Ag reference electrode was used throughout this study, unless specifically stated), which is approximately 0.5 V more positive than the open circuit potential (OCP). The overall potential window for $Ti_3C_2T_x$ in each of the three WIS electrolytes is 1.6 V, a 60% increase over the potential windows of 3 M H_2SO_4 and 1 M LiCl.

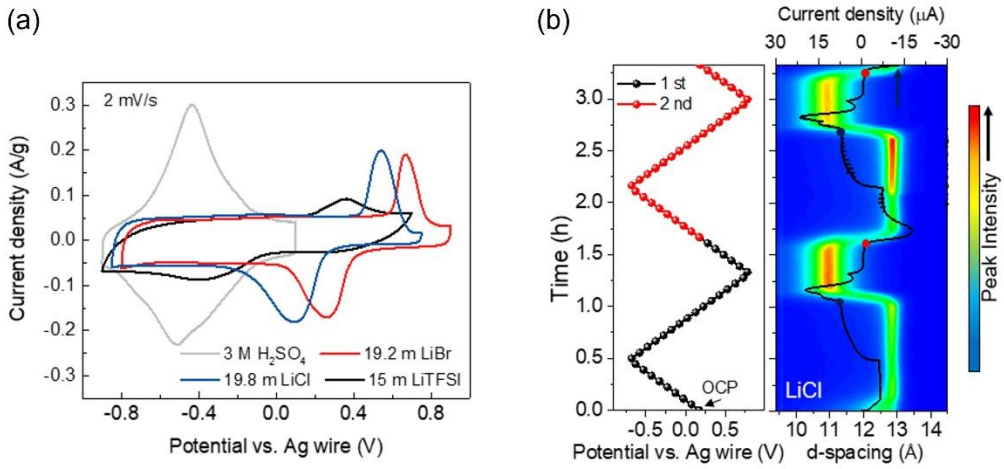

Figure 4.1. (a) Cyclic voltammograms for vacuum filtered $Ti_3C_2T_x$ electrodes collected at 2 mV/s in 19.8 m LiCl, 19.2 m LiBr, 15 m LiTFSI, and 3 M H_2SO_4 (b) The evolution of the interlayer spacing of $Ti_3C_2T_x$ during cyclic voltammetry in WIS electrolytes. *d*-spacing changes during cycling in 19.8 m LiCl electrolyte measured at a scan rate of 0.5 mV/s measured by *in situ* XRD. The intensities of the (002) diffraction peaks increases from blue to red, as shown in the scale bar.

Extending the stable electrochemical potential window towards more positive potentials activates a new electrochemical process, as shown by the pair of strong peaks in the anodic and cathodic scans of the CV curves for $Ti_3C_2T_x$ in all three WIS electrolytes. The two peaks in the WIS electrolytes correspond to a reversible process which contributes to increased charge storage capability.

4.4. Anomalous double-layer charging behavior

In situ XRD analysis was performed to monitor changes in the interlayer spacing of the $Ti_3C_2T_x$ electrode during electrochemical cycling in the WIS electrolytes. The (002)

peak, which corresponds to the *d*-spacing of $Ti_3C_2T_x$, was monitored for two cycles in the 19.8 m LiCl electrolyte without pre-cycling (Figure 4.1 (b)). The interlayer spacing changes were nearly identical for both cycles, indicating the reversibility of the process. The *d*-spacing of $Ti_3C_2T_x$ at the OCP (0.2 V *vs* Ag for 19.8 m LiCl) increased slightly from 12.7 Å to 12.9 Å when negative potential was applied. The *d*-spacing did not change when scanning from the OCP to -0.8 V and then back to 0.3 V, but an abrupt decrease from 12.9 Å to 11.0 Å was observed at 0.4 V. The narrow interlayer spacing did not change from 0.4 to 0.8 V, however, when the electrode was cycled back to 0.24 V, the interlayer spacing abruptly jumped from 11.0 Å to 12.9 Å over only a 100 mV change in potential. The abrupt shrinkage and expansion of the *d*-spacing both occur at the onset potentials of the anodic (marked by black dots in Figure 4.1 (b)) and cathodic (marked by red dots in Figure 4.1 (b)) peaks in the CVs, respectively.

Approximately the same trend and magnitude of change in *d*-spacing that were observed in the 15 m LiTFSI with larger anions size (0.39 × 0.8 nm for $TFSI^-$ versus 0.36 × 0.36 nm for Cl^-), which rules out the possibility of anion intercalation. Moreover, the *d*-spacing of 11 Å (an interlayer spacing of < 3.1 Å) at the maximum positive potential is too small to accommodate either Cl^- or $TFSI^-$. Additionally, the potentials required for the reversible oxidation/reduction of an anion pair do not correlate well with the potentials of the electrochemical process in the $Ti_3C_2T_x$/WIS system. Even the maximum applied potential of 0.8 V *vs* Ag is not sufficient to oxidize any of the anions of the WIS electrolytes. Since anions are not involved in the process, the peaks observed at positive potentials should then be due to cation (Li^+) insertion and de-insertion.

4.5. Desolvation-free cation insertion

To further investigate the charging mechanism of the WIS electrolytes, the relationship between the mass change caused by the insertion/desertion of electrolytes species and the abrupt interlayer spacing changes of the $Ti_3C_2T_x$ electrode was measured using an electrochemical quartz crystal microbalance with dissipation monitoring (EQCM-D) in 19.8 m LiCl (Figure 4.2 a & b). The added mass of the electrode was correlated with changes in the resonance frequency ($\Delta f/n$) following the Sauerbrey equation. Three electrochemical stages (S1-S3) were identified during the cathodic scan: (S1) From 0.45 V to 0.17 V, where almost no water accompanied the inserted Li^+. (S2) As soon as the potential reaches 0.17 V (red dot, onset potential of the cathodic peak), a dramatic increase in the amount of inserted water was observed, corresponding to 2.85 water molecules per intercalated Li^+. This water/Li^+ ratio is similar to the hydration number for Li^+ in the bulk WIS electrolyte (~2.80), meaning that desolvation did not occur for the Li^+ insertion process at the peak potentials in the WIS electrolytes, which is different from previous observations showing that the desolvation of Li^+ occurs upon intercalation into $Ti_3C_2T_x$.[15] Previous computational results suggest that desolvation-free Li^+ intercalation should result in EDL formation in MXenes in order to the maintain charge separation,[16] which is in agreement with our experimental observations. (S3) When the peak starts to fade below 0.05 V (yellow dot), the number of water molecules entering the $Ti_3C_2T_x$ with the Li^+ drops to 1.45 water per Li ion, which is similar to the value observed in Li-based salt-in-water electrolytes.[17] Reversibly, a greater number of water molecules per Li^+ leaves the interlayer space of the Ti_3CT_x at the onset potential of the anodic peak (from the black dot to the blue

dot in Figure 4.2 a) versus the peak-free region when the system cycles back from negative to positive potentials.

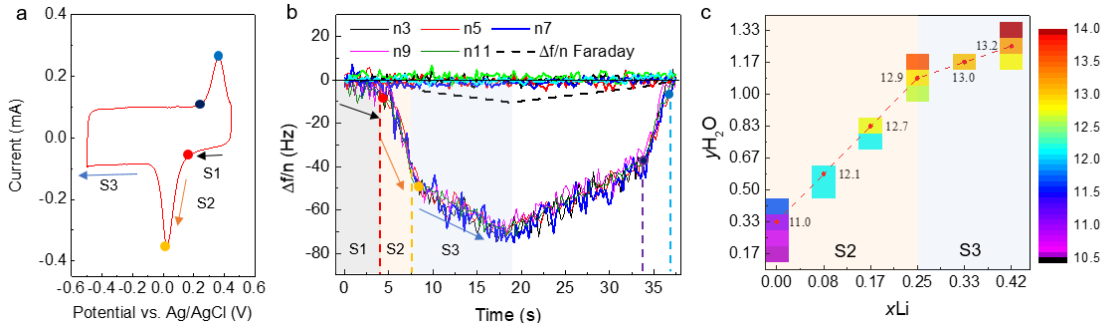

Figure 4.2 Changes in the populations of intercalated species during cycling of $Ti_3C_2T_x$ in 19.8 m LiCl. (a) Cyclic voltammogram recorded during electrochemical quartz crystal microbalance (EQCM) measurements. (b) Time-dependent changes of the resonance frequency $\Delta f/n$ during the insertion/extraction of Li^+ and water. (c) The *d*-spacings for various $Ti_3C_2O_2 \cdot xLi \cdot yH_2O$ as optimized by density functional theory (DFT) simulations.

Density functional theory (DFT) simulations (Figure 4.2) were performed to quantitatively correlate the changes in *d*-spacing with the intercalated species. We found that the S1 state is best represented by a composition of $Ti_3C_2O_2 \cdot 0.33H_2O$, whose 11.01 Å *d*-spacing from DFT closely matches the experimental *d*-spacing. We then inserted different numbers of water molecules and Li^+ ions and optimized the *d*-spacings of various $Ti_3C_2O_2 \cdot xLi \cdot yH_2O$ compositions (Figure 4.2c). The changes in the *d*-spacing for the S2 stage is best matched by co-intercalation of a 3:1 ratio of H_2O and Li^+ (close to the experimental value of 2.85 from EQCM), reaching a *d*-spacing of 12.94 Å for the composition $Ti_3C_2O_2 \cdot 0.25Li \cdot 1.08H_2O$, which matches well the XRD-measured *d*-spacing changes occurring during the cathodic scan (from 11.0 Å to 12.9 Å). As Li^+ ions are further inserted into the interlayer space (S3), we found that a significantly reduced H_2O/Li^+ ratio (1:1) best captures the almost constant *d*-spacing of ~13.0 Å in this regime. Hence, the

(de)intercalation of the solvated $[Li(H_2O)_3]^+$ species accounts for the large variations in the *d*-spacing and is responsible for the "redox-like" peaks seen in the voltammograms in the WIS electrolytes. Further DFT simulations of the intercalation energy and voltage confirm that the S2 stage has a higher thermodynamic driving force than the S3 stage for the intercalation of Li^+ ions (Figure 4.3a) and that the S2 stage has a much wider plateau at 0.5 V *vs* Ag/AgCl in the intercalation voltage *vs* *x*Li plot (Figure 4.3b), agreeing well with the midpoint between the cathodic and anodic peaks in Figure 4.1a. Since the stage S2 is not correlated with a distinct charge transfer process, we define this desolvation-free Li^+ insertion process as the mechanically coupled formation/removal of a confined double-layer between conducting 2D sheets.

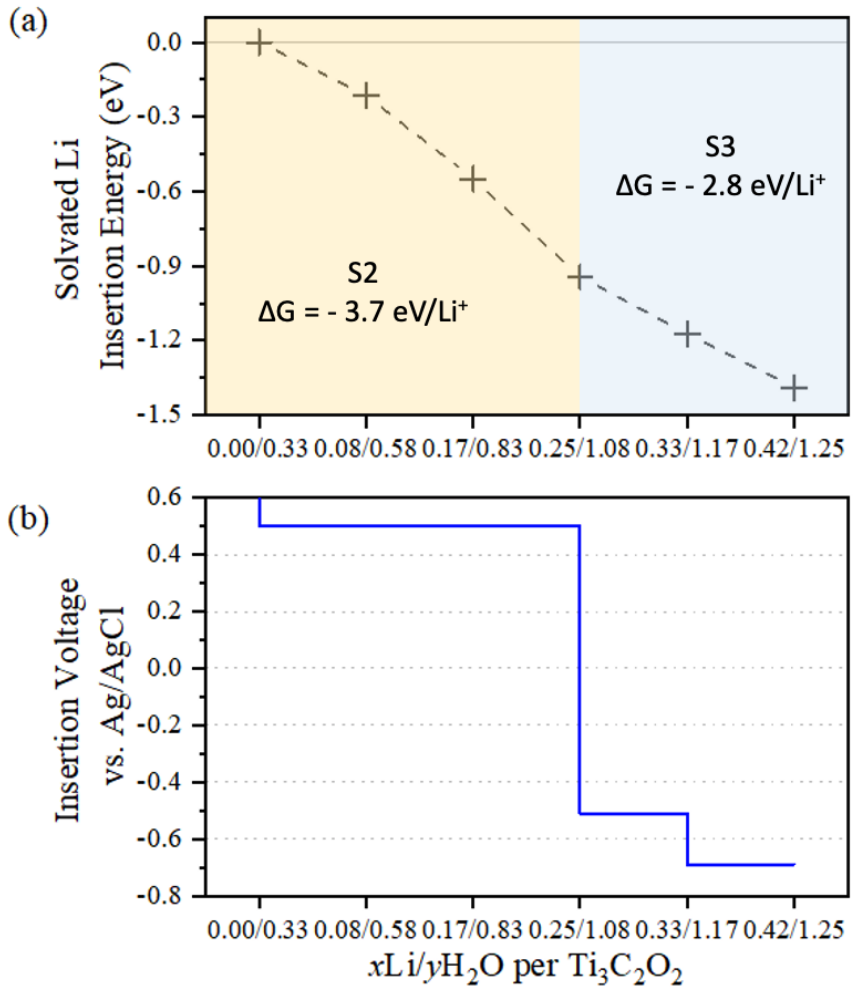

Figure 4.3. DFT-predicted insertion energy and voltage versus the amount of co-intercalated water and Li^+ in $Ti_3C_2O_2$. (a) Insertion energy of solvated Li^+ ions; each state is represented by a composition of $Ti_3C_2O_2 \cdot xLi \cdot yH_2O$ (the x/y pair is shown for the x-axis label). (b) Insertion voltage of solvated Li ion *vs* Ag/AgCl.

4.6. Conclusions

In this study, a desolvation-free Li^+ insertion charging mechanism was observed for $Ti_3C_2T_x$ MXene in WIS electrolytes. The process shows electrochemical characteristics identical to battery-like (Faradic) materials but was found to instead be caused by the formation of a confined electrical double-layer, where no distinct redox processes could be

observed at the potentials corresponding to the peaks in the voltammograms. In addition, this process is distinct from typical capacitive or pseudocapacitive charge storage due to the abrupt reversible interlayer space changes occurring when solvated Li^+ enters and exits the interlayer spaces of $Ti_3C_2T_x$ that is accompanied by sharp peaks with large peak potential separation. By extending the ion insertion potential and improving the oxidation resistance of $Ti_3C_2T_x$, the desolvation-free ion insertion process opens up opportunities for development of a new generation of devices for high-rate, high-energy storage and harvesting, as well as potential applications in sensing and actuation. By further increasing the cell potential to facilitate the reversible redox of halogen ions in confinement, there is potential for further increasing the amount of energy stored by 2D materials with confined electrolytes.

References

1. Mathis, T. S.; Kurra, N.; Wang, X.; Pinto, D.; Simon, P.; Gogotsi, Y., Energy Storage Data Reporting in Perspective—Guidelines for Interpreting the Performance of Electrochemical Energy Storage Systems. **2019,** *9* (39), 1902007.

2. Lukatskaya, M. R.; Kota, S.; Lin, Z.; Zhao, M.-Q.; Shpigel, N.; Levi, M. D.; Halim, J.; Taberna, P.-L.; Barsoum, M. W.; Simon, P.; Gogotsi, Y., Ultra-high-rate pseudocapacitive energy storage in two-dimensional transition metal carbides. *Nature Energy* **2017,** *2* (8), 17105.

3. Xia, Y.; Mathis, T. S.; Zhao, M.-Q.; Anasori, B.; Dang, A.; Zhou, Z.; Cho, H.; Gogotsi, Y.; Yang, S., Thickness-independent capacitance of vertically aligned liquid-crystalline MXenes. *Nature* **2018,** *557* (7705), 409-412.

4. Augustyn, V.; Come, J.; Lowe, M. A.; Kim, J. W.; Taberna, P.-L.; Tolbert, S. H.; Abruña, H. D.; Simon, P.; Dunn, B., High-rate electrochemical energy storage through Li^+ intercalation pseudocapacitance. *Nature Materials* **2013,** *12* (6), 518-522.

5. Li, Y.; Shao, H.; Lin, Z.; Lu, J.; Liu, L.; Duployer, B.; Persson, P. O. Å.; Eklund, P.; Hultman, L.; Li, M.; Chen, K.; Zha, X.-H.; Du, S.; Rozier, P.; Chai, Z.; Raymundo-Piñero, E.; Taberna, P.-L.; Simon, P.; Huang, Q., A general Lewis acidic etching route for preparing MXenes with enhanced electrochemical performance in non-aqueous electrolyte. *Nature Materials* **2020,** *19* (8), 894-899.

6. Wang, X.; Mathis, T. S.; Li, K.; Lin, Z.; Vlcek, L.; Torita, T.; Osti, N. C.; Hatter, C.; Urbankowski, P.; Sarycheva, A.; Tyagi, M.; Mamontov, E.; Simon, P.; Gogotsi, Y., Influences from solvents on charge storage in titanium carbide MXenes. *Nature Energy* **2019,** *4* (3), 241-248.

7. Suo, L.; Borodin, O.; Gao, T.; Olguin, M.; Ho, J.; Fan, X.; Luo, C.; Wang, C.; Xu, K., "Water-in-salt" electrolyte enables high-voltage aqueous lithium-ion chemistries. **2015,** *350* (6263), 938-943.

8. Anasori, B.; Lukatskaya, M. R.; Gogotsi, Y., 2D metal carbides and nitrides (MXenes) for energy storage. *Nature Reviews Materials* **2017,** *2* (2), 16098.

9. Kresse, G.; Furthmüller, J., Efficient iterative schemes for ab initio total-energy calculations using a plane-wave basis set. *Physical Review B* **1996,** *54* (16), 11169-11186.

10. Perdew, J. P.; Burke, K.; Ernzerhof, M., Generalized Gradient Approximation Made Simple. *Physical Review Letters* **1996,** *77* (18), 3865-3868.

11. Blöchl, P. E., Projector augmented-wave method. *Physical Review B* **1994,** *50* (24), 17953-17979.

12. Grimme, S.; Antony, J.; Ehrlich, S.; Krieg, H., A consistent and accurate ab initio parametrization of density functional dispersion correction (DFT-D) for the 94 elements H-Pu. **2010,** *132* (15), 154104.

13. Peterson, A. A.; Abild-Pedersen, F.; Studt, F.; Rossmeisl, J.; Nørskov, J. K., How copper catalyzes the electroreduction of carbon dioxide into hydrocarbon fuels. *Energy & Environmental Science* **2010,** *3* (9), 1311-1315.

14. Gokcen, N. A. J. J. o. t. A. C. S., Vapor pressure of water above saturated lithium chloride solution. **1951,** *73* (8), 3789-3790.

15. Gao, Q.; Sun, W.; Ilani-Kashkouli, P.; Tselev, A.; Kent, P. R. C.; Kabengi, N.; Naguib, M.; Alhabeb, M.; Tsai, W.-Y.; Baddorf, A. P.; Huang, J.; Jesse, S.; Gogotsi, Y.; Balke, N., Tracking ion intercalation into layered Ti_3C_2 MXene films across length scales. *Energy & Environmental Science* **2020,** *13* (8), 2549-2558.

16. Shao, H.; Xu, K.; Wu, Y.-C.; Iadecola, A.; Liu, L.; Ma, H.; Qu, L.; Raymundo-Piñero, E.; Zhu, J.; Lin, Z.; Taberna, P.-L.; Simon, P., Unraveling the Charge Storage Mechanism of $Ti_3C_2T_x$ MXene Electrode in Acidic Electrolyte. *ACS Energy Letters* **2020,** *5* (9), 2873-2880.

17. Lukatskaya, M. R.; Bak, S.-M.; Yu, X.; Yang, X.-Q.; Barsoum, M. W.; Gogotsi, Y., Probing the Mechanism of High Capacitance in 2D Titanium Carbide Using In Situ X-Ray Absorption Spectroscopy. **2015,** *5* (15), 1500589.

Chapter 5. MXene edge structure search

5.1. Introduction

Previous studies have revealed that once proton intercalated into the MXene interlayer, the surface redox reaction, as well as in-water transfer, is fast.[1] The rate-limiting step for the charging process could be the proton edge intercalation. The edge structure would significantly affect proton intercalation behavior as well as other intercalating species. Other than the edge intercalation process, the MXene edge structure also plays important role in MXene oxidation. Zhang *et al*. discovered MXene oxidation starts at the flake edge.[2] Natu *et al*. found capping the MXene edge with polyanionic salts could mitigate the oxidation of the MXene.[3]

Despite the many reports on MXene, the edge structures of MXene are unclear. In this work, we employed an evolutionary algorithm coupled with first-principles calculations extensively investigated the $Ti_3C_2O_2$ edge structure. From our search, the structures of stoichiometric edge are revealed. The phase stability diagrams of the considered edge structures were also constructed with reference to the chemical potentials of the component elements.

5.2. Computational methods

The search of the stoichiometric edge structures was performed by the evolutionary algorithm implemented in the Universal Structure Predictor: Evolutionary Xtallography package (USPEX). [4, 5] The algorithm has been successfully applied to bulk crystals,[6, 7] nanoparticles[8, 9], and solid surfaces.[10, 11] For the edge structure search, each

candidate structure consists of vacuum region, edge region, and substrate region. The substrate region is divided into buffer regions and fixed regions. Only the edge region and buffer region are optimized. For each type of edge, 40 populations are generated randomly in the first generation, and 30 populations are generated accordingly for the following generations. More than 180 generations and more than 63000 structures are explored in the entire search.

The Vienna Ab-initio Simulation Package (VASP) was invoked for first principles optimizations during the USPEX calculation.[4, 5, 12] Perdew-Burke-Ernzerhof (PBE) version of general-gradient approximation (GGA) are adopted for electron exchange-correlation functional.[13] DFT-D3 correction was used to describe the van der Waals interaction.[14] Projector augmented-wave (PAW) potentials are employed to account for electron-core interaction.[15] An energy cutoff of 500 eV was used for the plane-wave basis set. To faster the structure search process, a finite vacuum size, convergency criterial, and reciprocal-space k-point mesh resolution was adopted. So, after the structure search, the structures within 0.5 eV higher in energy compared to the lowest energy structure were submitted to higher accuracy optimization. A dense k-point sampling with the grid spacing around $2\pi \times 0.05$ $Å^{-1}$ in the Brillouin zone and a vacuum layer with a thickness of ~15 Å are selected for further optimization. The ionic positions are fully relaxed until the residual force on each ion is less than 0.01 eV/ Å. The lowest energy structure for each edge type from the further optimization were determined as the predicted stable surface.

According to different directions of termination, two kinds of edges are investigated here: armchair (AM) and zigzag (ZZ) (Figure 5.1a). Based on the conformation of the

exposed layer, the stoichiometric ZZ edge can then be divided into 3 types. Follow the notation of the previous study,[16] the layers contain the termination atom are named after the termination atom, "O" in our case, while other layers are named as "M" (Figure 5.1a). The order of the outmost three layers results in 3 types of ZZ edge: MMO, MOM, and OMM. To model each type, a slab with 6 formula unit plus edge were constructed (Figure 5.1b). The top two layers of the ZZ edge and the top one layer of the AM edge were treated as the surface region in which the initial positions were determined by USPEX. The bottom two formula units were treated as the fixed region, in which the positions were fixed to the bulk $Ti_3C_2O_2$. The rest middle layers were treated as the buffer region, which the initial positions were provided as the bulk $Ti_3C_2O_2$.

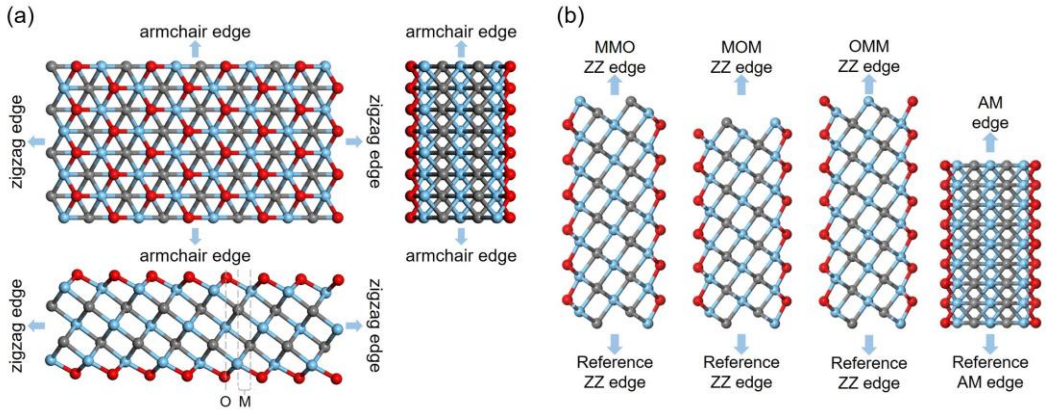

Figure 5.1 (a)Schematic of MXene zigzag (ZZ) and armchair (AM) edge (b) side view of MMO, MOM, OMM ZZ edge, and AM edge.

5.3. MXene edge in vacuum

We first studied the edge structure in vacuum. The interlayer spacing of the MXene slab is set to the interlayer spacing of the bulk AA stacked MXene. The side view of the schematic slab model is shown in Figure 5.2.

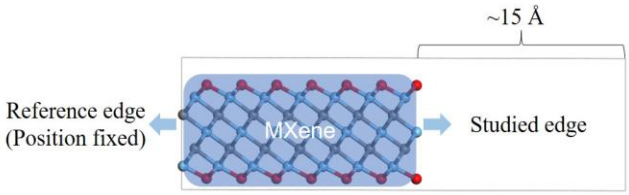

Figure 5.2. Schematic model of studied MXene edge in vacuum.

The side and top views of the predicted stable structure for each edge type are depicted in Figure 5.3. Except for the OMM ZZ edge, other types of edges exhibit atoms connected the nearby two $Ti_3C_2O_2$ layers.

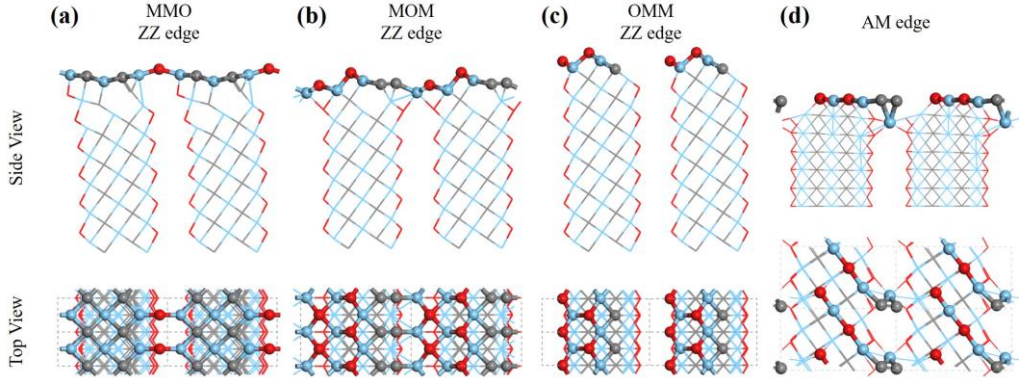

Figure 5.3. Side and top view of the predicted stable structure.

To further study the stability of different types of edges, we construct the stability diagram based on the surface excess grand potential (SGP). Following the previous study,[17] the total SGP of the slab can be defined as

$$\Omega_i^{total} = E_{slab}^i + PV - TS - N_{Ti}\mu_{Ti} - N_C\mu_C - N_O\mu_O \qquad (1)$$

where E_{slab}^i is the total energy of the slab system and N_{Ti}, N_C and N_O are the number of Ti, C, and O atoms in the slab model, respectively. μ_{Ti}, μ_C and μ_O are the chemical potentials of Ti, C, and O atoms, respectively. For a solid material, the PV term is small and constant and at low temperature the entropic contribution is negligible. Moreover, in

each slab model, one side of the slab is the desired edge with optimized atomic positions while the other side is the reference edge with the atomic position fixed to the bulk structure. Thus, the total SGP of slab i is consists of both SGP of edge i and SGP of the reference edge. Therefore, the above equation can be rewritten as

$$\Omega_i + \Omega_{ref} = E^i_{slab} - N_{Ti}\mu_{Ti} - N_C\mu_C - N_O\mu_O \qquad (2)$$

Since the desired edge and the reference edge always possess the same surface area S, so the SGP per unit area of edge i (ω_i) can be calculated from the below equation:

$$\omega_i = -\omega_{ref} + \frac{1}{S}\left(E^i_{slab} - N_{Ti}\mu_{Ti} - N_C\mu_C - N_O\mu_O\right) \qquad (3)$$

The chemical potential of each constituent elements is linked by the chemical potential of the bulk $Ti_3C_2O_2$:

$$\mu_{Ti_3C_2O_2} = E^{bulk}_{Ti_3C_2O_2} = 3\mu_{Ti} - 2\mu_C - 2\mu_O \qquad (4)$$

The variation of the chemical potential of each constituent elements is then referenced to the computed reference energy as shown below:

$$\Delta\mu_{Ti} = \mu_{Ti} - E^{bulk}_{Ti} \qquad (5)$$

$$\Delta\mu_C = \mu_{Ti} - E^{graphite}_C \qquad (6)$$

$$\Delta\mu_O = \mu_O - \frac{1}{2}E^{gas}_{O_2} \qquad (7)$$

where E^{bulk}_{Ti} and $E^{graphite}_C$ are the calculated total energy per atom from the related bulk phase, and $E^{gas}_{O_2}$ is the total energy of the O_2 molecule. By using equation (4)~(7), equation (3) can be rewritten as:

$$\omega_i = \phi_i - \omega_{ref} - \frac{1}{S}\left[\left(N_C - \frac{2}{3}N_{Ti}\right)\Delta\mu_C + \left(N_O - \frac{2}{3}N_{Ti}\right)\Delta\mu_O\right] \qquad (8)$$

$$\phi_i = \frac{1}{S}[E^i_{slab} - \frac{1}{3}N_{Ti} \cdot E_{Ti_3C_2O_2} - \left(N_C - \frac{2}{3}N_{Ti}\right)E_C^{graphite} - (N_O - \frac{2}{3}N_{Ti})\frac{1}{2}E_{O_2}^{gas}] \quad (9)$$

Since the slab model of AM and ZZ edge can't possess the same reference edge, so we then constructed slabs from bulk $Ti_3C_2O_2$ with both sides formed by reference edge to obtain the expression of the reference edge's SGP per unit area (ω_{ref}) from equation (10). In the previous slab model (desired edge + reference edge), the reference edges were fixed to the bulk structure. Therefore, the E^{ref}_{slab} was obtained from the unoptimized double reference edge slab model.

$$2\omega_{ref} = \phi_{ref} - \frac{1}{S}[\left(N_C - \frac{2}{3}N_{Ti}\right)\Delta\mu_C + (N_O - \frac{2}{3}N_{Ti})\Delta\mu_O] \quad (10)$$

The chemical potentials ranges were determined by imposing a series of thermodynamic boundary conditions. First, to avoid the Ti, C and O condense on the edge, their chemical potentials must be lower than their chemical potential of the stable phase:

$$\Delta\mu_{Ti} < 0 \quad (11)$$

$$\Delta\mu_C < 0 \quad (12)$$

$$\Delta\mu_O < 0 \quad (13)$$

By combining equation (4) and (11), we could obtain:

$$2\Delta\mu_C + 2\Delta\mu_O > \Delta H_{f,Ti_3C_2O_2} \quad (14)$$

where

$$\Delta H_{f,Ti_3C_2O_2} = E_{Ti_3C_2O_2} - 3E^{bulk}_{Ti} - 2E_C^{graphite} - E_{O_2}^{gas} \quad (15).$$

To avoid the precipitation of oxidation product of $Ti_3C_2O_2$: TiO and TiO_2, the following boundary condition should be satisfied:

$$\frac{2}{3}\Delta\mu_C - \frac{1}{3}\Delta\mu_O > \frac{1}{3}\Delta H_{f,Ti_3C_2O_2} - \Delta H_{f,TiO} \qquad (16),$$

$$\frac{2}{3}\Delta\mu_C - \frac{4}{3}\Delta\mu_O > \frac{1}{3}\Delta H_{f,Ti_3C_2O_2} - \Delta H_{f,TiO_2} \qquad (17),$$

where

$$\Delta H_{f,TiO} = E_{TiO} - E_{Ti}^{bulk} - \frac{1}{2}E_{O_2}^{gas} \qquad (18),$$

$$\Delta H_{f,TiO_2} = E_{TiO_2} - E_{Ti}^{bulk} - E_{O_2}^{gas} \qquad (19).$$

By satisfying the boundary condition above, we can obtain the allowed region for $Ti_3C_2O_2$.

For each edge, the SGP must be positive, otherwise the bulk solid would disintegrate to maximize its surface area. At specific $\Delta\mu_C$ and $\Delta\mu_O$, the edge that possesses the lowest positive SGP per unit area was determined as the most stable edge. Therefore, we obtained the diagram with different color areas represent different edges as the most stable edge (Figure 5.4a). From Figure 5.4a, we found under the allowed region for $Ti_3C_2O_2$, the MOM ZZ edge which predicts possessing interlayer connection is the most stable edge.

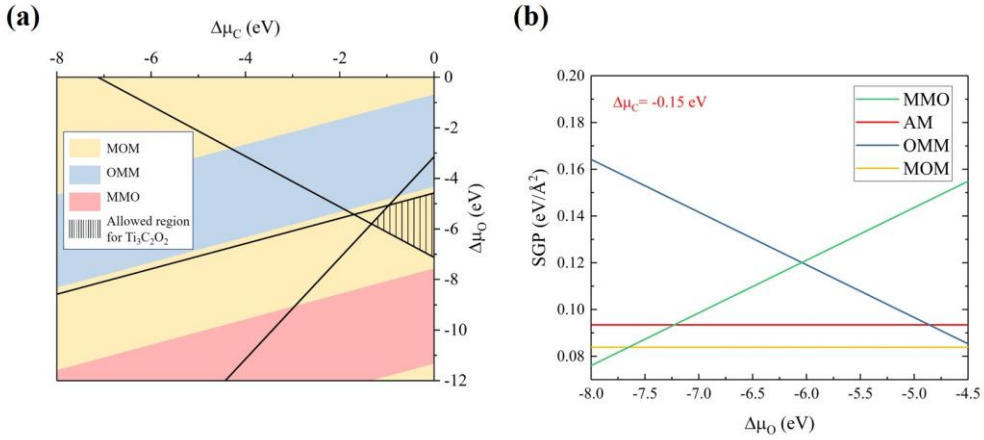

Figure 5.4 (a) stability diagram of the MXene edge. (b) The SGPs of different edge with $\Delta\mu_C = -0.15\ eV$.

5.4. Hydrated MXene edge

A previous study has shown that MXene slowly oxidates in pure water.[18] Therefore, we further study the hydrated MXene edge structure. According to a previous study, the interlayer spacing of MXene expands when immersing in electrolytes.[19] The expansion of the interlayer spacing could prohibit the formation of the interlayer connection. So, to avoid the interlayer interaction, here we enlarge the interlayer spacing of the MXene to 15Å. The side view of the schematic slab model is shown in Figure 5.5.

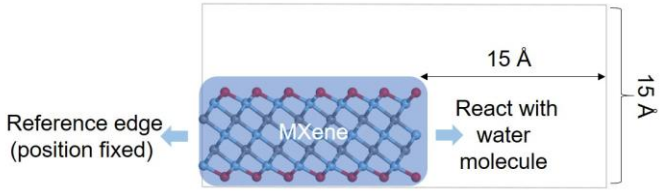

Figure 5.5 Schematic model of studied hydrated MXene edge.

To study the hydrated MXene edge, we search the edge structure of MXene react with different numbers of water molecules. Here we stop increasing the reactive water number in structure search when any of the following condition is satisfied: 1) The additionally added water molecule doesn't react with the edge; 2) The additionally added water molecule yields positive reaction energy; 3) The additionally added water molecule results in a negative surface excess grand potential under MXene allowed chemical potential range.

The side and top views of the predicted stable structure for each ZZ hydrated edge type are depicted in Figure 5.6. The MMO edge satisfied the first condition where the

fourth added water molecule only physically adsorbed on the edge. While the MOM and OMM edge satisfied the third condition. As shown in Figure 5.6, when ZZ edge reacts with water molecules, some of it produces CH_4 or H_2 gas molecules.

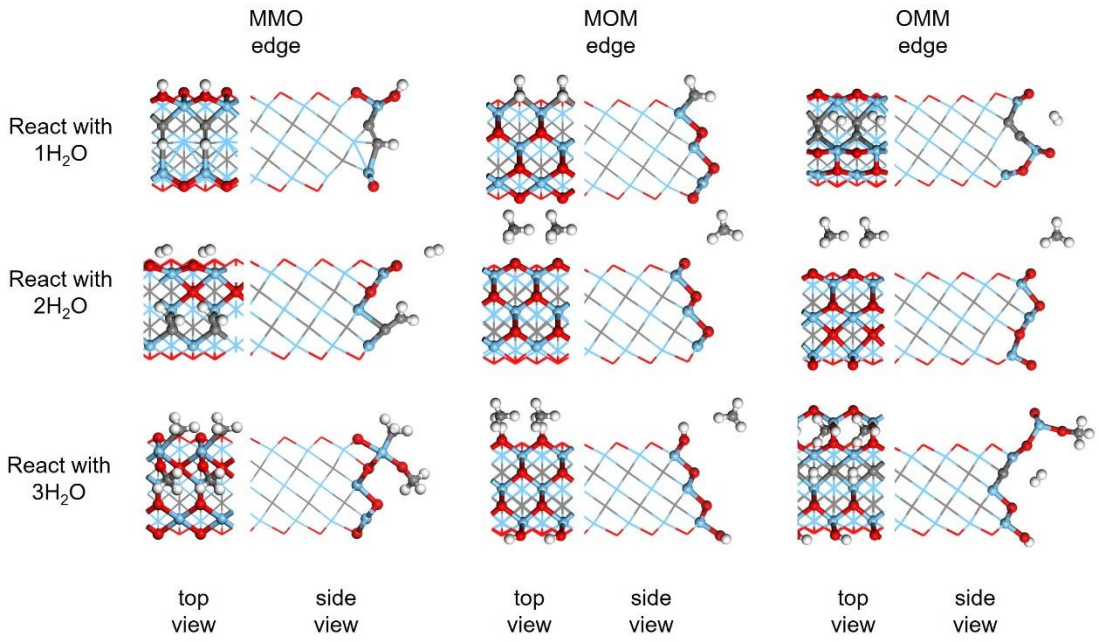

Figure 5.6 Side and top view of the predicted stable hydrated ZZ edge structure.

The side and top view of the predicted stable structure for AM hydrated edge type are depicted in Figure 5.7. The AM edge satisfied the second condition where the fourth added water molecule yields positive reaction energy. Same as the ZZ edge, when AM edge reacts with water molecules, some of it produces CH_4 or H_2 gas molecule.

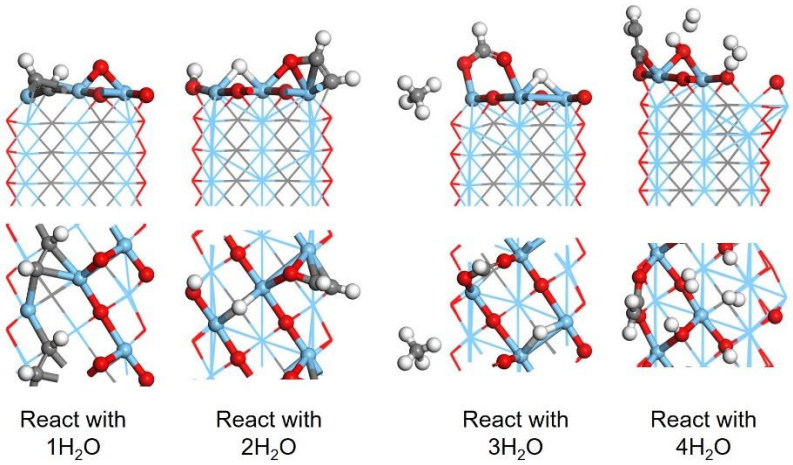

Figure 5.7 Side and top view of the predicted stable hydrated AM edge structure.

We then study the stability of different types of edges when reacting with different water molecules. We construct the stability diagram based on the surface excess grand potential (SGP). Similar to the vacuum case, the total SGP per unit area of slab i can be defined as

$$\omega_i = -\omega_{ref} + \frac{1}{S}\left(E^i_{edge} - N_{Ti}\mu_{Ti} - N_C\mu_C - N_O\mu_O - N_{H_2O}\mu_{H_2O}\right) \quad (20)$$

where $E^i_{edge} = E^i_{slab} + N_{mole}\mu^i_{mole}$ is the sum of the total energy of the slab system and the chemical potential of the produced gas molecule. N_{Ti}, N_C, N_O and N_{H_2O} are the number of Ti, C, O atoms, and H_2O molecules in the slab model, respectively. μ_{Ti}, μ_C, μ_O and μ_{H_2O} are the chemical potentials of Ti, C, O atoms, and H_2O molecules, respectively.

The chemical potential of each constituent elements is linked by the chemical potential of the bulk $Ti_3C_2O_2$ with an interlayer spacing of 15Å:

$$\mu_{Ti_3C_2O_2} = E^{bulk}_{Ti_3C_2O_2} = 3\mu_{Ti} - 2\mu_C - 2\mu_O \quad (21)$$

Similar to the vacuum case, equation (20) can be rewritten as:

$$\omega_i = \phi_i - \omega_{ref} - \frac{1}{S}[\left(N_C - \frac{2}{3}N_{Ti}\right)\Delta\mu_C + (N_O - \frac{2}{3}N_{Ti})\Delta\mu_O] \quad (22)$$

$$\phi_i = \frac{1}{S}[E^i_{edge} - \frac{1}{3}N_{Ti} \cdot E_{Ti_3C_2O_2} - \left(N_C - \frac{2}{3}N_{Ti}\right)E_C^{graphite} - (N_O - \frac{2}{3}N_{Ti})\frac{1}{2}E_{O_2}^{gas} - N_{H_2O}\mu_{H_2O}] \quad (23)$$

The reference edge's SGP per unit area (ω_{ref}), the boundary conditions are determined by the same way as the vacuum case with the $E_{Ti_3C_2O_2}$ set to the chemical potential of the bulk $Ti_3C_2O_2$ with an interlayer spacing of 15Å.

At specific $\Delta\mu_C$ and $\Delta\mu_O$, the edge that possesses the lowest positive SGP per unit area was determined as the most stable edge. Therefore, we obtained the diagram with different color areas represent different edges as the most stable edge (Figure 5.8). As shown in Figure 5.8, the AM-3H_2O, MMO-3H_2O, MMO-2H_2O edge are the stable edge under the allowed region for $Ti_3C_2O_2$. An early study revealed that CH_4 is the gas species produced from $Ti_3C_2T_x$.[20] This corresponds well with our finding of under certain chemical potential range the AM-3H2O with CH_4 production is the most stable edge.

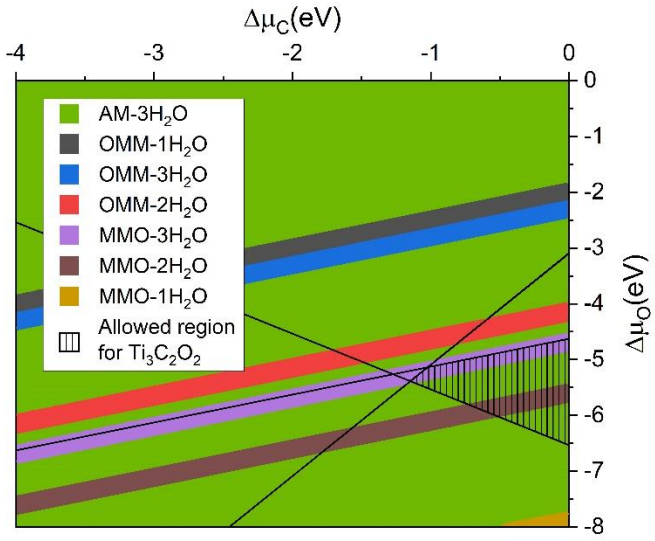

Figure 5.8 stability diagram of the hydrated MXene edge.

5.5. Conclusions

In conclusion, we extensively investigate the MXene edge structure in a vacuum and in water. By employed the evolutional algorithm, the stable edge structures of armchair, MMO zigzag, MOM zigzag, and OMM zigzag edges were predicted. The surface excess grand potentials were then employed to investigate the stability of different edges. From the stability diagram, the MOM zigzag edge was determined as the most stable edge in vacuum condition. While AM-3H_2O, MMO-3H_2O, MMO-2H_2O edge are the stable edge in the water. This work provides a foundation for further explore edge involved process of $Ti_3C_2O_2$.

References

1. Sun, Y.; Zhan, C.; Kent, P. R. C.; Naguib, M.; Gogotsi, Y.; Jiang, D.-e., Proton Redox and Transport in MXene-Confined Water. *ACS Applied Materials & Interfaces* **2020,** *12* (1), 763-770.

2. Zhang, C. J.; Pinilla, S.; McEvoy, N.; Cullen, C. P.; Anasori, B.; Long, E.; Park, S.-H.; Seral-Ascaso, A.; Shmeliov, A.; Krishnan, D.; Morant, C.; Liu, X.; Duesberg, G. S.; Gogotsi, Y.; Nicolosi, V., Oxidation Stability of Colloidal Two-Dimensional Titanium Carbides (MXenes). *Chemistry of Materials* **2017,** *29* (11), 4848-4856.

3. Natu, V.; Hart, J. L.; Sokol, M.; Chiang, H.; Taheri, M. L.; Barsoum, M. W., Edge Capping of 2D-MXene Sheets with Polyanionic Salts To Mitigate Oxidation in Aqueous Colloidal Suspensions. **2019,** *58* (36), 12655-12660.

4. Glass, C. W.; Oganov, A. R.; Hansen, N., USPEX—Evolutionary crystal structure prediction. *Computer Physics Communications* **2006,** *175* (11), 713-720.

5. Lyakhov, A. O.; Oganov, A. R.; Stokes, H. T.; Zhu, Q., New developments in evolutionary structure prediction algorithm USPEX. *Computer Physics Communications* **2013,** *184* (4), 1172-1182.

6. Eklund, K.; Kuklin, M. S.; Kraus, F.; Karttunen, A. J., Evolutionary Algorithm-based Crystal Structure Prediction for Gold(I) Fluoride. **2020,** *21* (8), 802-808.

7. Yu, Y.; Wang, Z.; Shao, G., Theoretical tuning of Ruddlesden–Popper type anti-perovskite phases as superb ion conductors and cathodes for solid sodium ion batteries. *Journal of Materials Chemistry A* **2019,** *7* (17), 10483-10493.

8. Mahdavifar, Z.; Shojaei, F., Evolutionary search for $(M©B16)^{Q}$ (M = Sc–Ni; Q = 0/−1) clusters: bowl/boat vs. tubular shape. *Physical Chemistry Chemical Physics* **2019,** *21* (40), 22618-22628.

9. Sen, A.; Sen, P., Designing rare earth free permanent magnets: insights from small Co clusters. *Physical Chemistry Chemical Physics* **2019,** *21* (40), 22577-22583.

10. Dupont, C.; Jupille, J.; Bourgeois, S.; Le Fèvre, P.; Verdini, A.; Floreano, L.; Domenichini, B., Substitution of Titanium for Magnesium Ions at the Surface of Mg-Doped Rutile. *The Journal of Physical Chemistry C* **2020,** *124* (21), 11490-11498.

11. Zhou, R.; Li, D.; Qu, B.; Sun, X.; Zhang, B.; Zeng, X. C., Rutile TiO_2(011)-2 × 1 Reconstructed Surfaces with Optical Absorption over the Visible Light Spectrum. *ACS Applied Materials & Interfaces* **2016,** *8* (40), 27403-27410.

12. Kresse, G.; Furthmüller, J., Efficient iterative schemes for ab initio total-energy

calculations using a plane-wave basis set. *Physical Review B* **1996,** *54* (16), 11169-11186.

13. Perdew, J. P.; Burke, K.; Ernzerhof, M., Generalized Gradient Approximation Made Simple. *Physical Review Letters* **1996,** *77* (18), 3865-3868.

14. Grimme, S.; Antony, J.; Ehrlich, S.; Krieg, H., A consistent and accurate ab initio parametrization of density functional dispersion correction (DFT-D) for the 94 elements H-Pu. **2010,** *132* (15), 154104.

15. Blöchl, P. E., Projector augmented-wave method. *Physical Review B* **1994,** *50* (24), 17953-17979.

16. Hong, L.; Klie, R. F.; Öğüt, S., First-principles study of size- and edge-dependent properties of MXene nanoribbons. *Physical Review B* **2016,** *93* (11), 115412.

17. Wang, Y.; Cheng, J.; Behtash, M.; Tang, W.; Luo, J.; Yang, K., First-principles studies of polar perovskite $KTaO_3$ surfaces: structural reconstruction, charge compensation, and stability diagram. *Physical Chemistry Chemical Physics* **2018,** *20* (27), 18515-18527.

18. Huang, S.; Mochalin, V. N., Hydrolysis of 2D Transition-Metal Carbides (MXenes) in Colloidal Solutions. *Inorganic Chemistry* **2019,** *58* (3), 1958-1966.

19. Mu, X.; Wang, D.; Du, F.; Chen, G.; Wang, C.; Wei, Y.; Gogotsi, Y.; Gao, Y.; Dall'Agnese, Y., Revealing the Pseudo-Intercalation Charge Storage Mechanism of MXenes in Acidic Electrolyte. **2019,** *29* (29), 1902953.

20. Huang, S.; Mochalin, V. N., Understanding Chemistry of Two-Dimensional Transition Metal Carbides and Carbonitrides (MXenes) with Gas Analysis. *ACS Nano* **2020,** *14* (8), 10251-10257.

Chapter 6. Proton dynamics in tunnel *h*-WO_3 hydrates

6.1. Introduction

Transition metal oxides have been used as pseudocapacitive electrodes due to their reversible redox feature and multi-valent oxidation states in acidic electrolytes, such as H_2SO_4 aqueous solution.[1, 2] They usually exhibit capacitance over 500 F/g, much higher than double-layer capacitances of activated carbons.[3] In particular, ruthenium oxide (RuO_2) has been studied as a typical pseudocapacitive material to understand the charge storage mechanism of pseudocapacitor for a long time[4] and its capacitive performance is significantly affected by the hydration level.[5]

Tungsten oxides and its hydrates are also of interest as pseudocapacitive materials.[6, 7] Among all the phases of WO_3, the hexagonal phase (*h*-WO_3) has sub-nanometer tunnels which allow fast proton intercalation and transport, leading to fast charging/discharging.[8, 9] Water molecules confined in the hexagonal tunnels were found to facilitate the proton insertion.[10] During the proton (de)insertion process, the *h*-WO_3 showed proton concentration and hydration level changes.[11]

Despite the interesting results of proton/water transport inside the 1D tunnels of *h*-WO_3, it remains unclear how proton, water, and the inner hydrophilic surface lining up the tunnels interact with each other to promote proton transport. One also wonders if the proton transport along the 1D tunnel still follows the Grotthuss mechanism via a chain of confined water molecules, or diffuse through the corner-sharing WO_6 octahedra as already been demonstrated for monoclinic $WO_3 \cdot 2H_2O$.[12, 13] Although there have been numerous

simulations of water-solvated proton transport in carbon nanotubes,[14-17] no such effort has been devoted to proton transport in the 1D tunnels inside transition-metal oxides. As such, here we aim to reveal the atomistic mechanism of proton transport inside the 1D tunnels of *h*-WO_3 via first principles molecular dynamics (FPMD) based on density functional theory (DFT).

6.2. Methods

DFT calculations and FPMD simulations were performed by using Vienna *Ab initio* Simulation Package (VASP).[18] The Perdew-Burke-Ernzerhof (PBE) functional within the generalized gradient approximation (GGA) was used for electron exchange-correlation.[19] Projector augmented wave (PAW) potential was used to treat the nuclei-electron interaction.[20] An energy cutoff of 700 eV was chosen for plane wave basis sets. DFT-D2 with GGA-PBE for van der Waals interaction was employed in all simulations which yielded the best agreement with the experiment for lattice parameters.[21] Atomic coordinates and lattice parameters were relaxed with convergence criterion of 10^{-5} eV in energy and 0.01 eV/Å in force. FPMD simulations were performed in canonical ensemble (NVT) with Nosé-thermostat under 300 K for 13 ps with 0.5 fs time step.[22-24] All the analyses were obtained from the last 12 ps trajectories.

Bulk 1×1×2 supercells of hexagonal tungsten oxide (*h*-WO_3) containing 6 formula units were used for computing water and proton intercalation energies. The Brillouin zone was sampled by a 4×4×4 Monkhorst-Pack k-mesh. The water intercalation energy was calculated according to: $E_{inter}(x) = \frac{E_{WO_3 \cdot xH_2O} - E_{WO_3} - xE_{H_2O}}{x}$, where *x* represents hydration level. The proton intercalation energy (E_H) in reference to ½ H_2 molecule in the gas phase

was calculated by the following equation: $E_H = \frac{E_{WO_3 \cdot xH_2O \cdot yH} - E_{WO_3 \cdot xH_2O} - y \cdot \frac{1}{2} E_{H_2}}{y}$, where x and y represent hydration and protonation levels, respectively.

FPMD simulations were performed on 1×1×4 supercell of h-WO_3 containing 12 formula units. The translational diffusivity of proton along the channel ($D_{trans,z}$) was obtained from the time-dependent z-direction-projected mean square displacement (zMSD) of O_0 (oxygen atom of the hydronium ion): $D_{trans,z} = \frac{1}{2}\frac{\partial zMSD(\mathrm{t})}{\mathrm{t}}$, where $\mathrm{zMSD(t)} = \langle|\vec{r}_z(t) - \vec{r}_z(0)|^2\rangle$ and $\vec{r_z}$ is z-projected position of O_0.

Rotational diffusivity of the water molecule was achieved by calculating the slope of the rotational mean square displacement (RMSD) vs time: $D_{trans,z} = \frac{1}{4}\frac{\partial RMSD(\mathrm{t})}{\mathrm{t}}$, where $\mathrm{RMSD(t)} = \langle|\varphi_t - \varphi_0|^2\rangle = \left\langle\left|\int_0^t \overrightarrow{d\varphi}\right|^2\right\rangle$. The vector $\overrightarrow{d\varphi}$ has the direction of $\vec{p}(t') \times \vec{p}(t' + dt)$ and magnitude $\left|\overrightarrow{d\varphi}\right| = cos^{-1}(\vec{p}(t') \cdot \vec{p}(t' + dt))$ where $\vec{p}(t')$ is the dipole vector of the water molecule.

6.3. Results and discussion

6.3.1. Tunnel structure in h-WO_3 and protonation sites in h-WO_3 with confined water.

Figure 6.1 shows the 1D tunnels (yellow isosurfaces) along the z axis with a diameter of ~5.4 Å inside h-WO_3. These hexagonal-shaped channels can incorporate water in the amount of 0.5 ~ 0.9 H_2O per h-WO_3 formula unit.[8, 11] Due to the small diameter of the channels, the water molecules form a 1D chain and indeed we found that water incorporation is favorable up to 0.83 water molecule per WO_3 (Figure 6.2(a)). The intercalated proton can bond with either the lattice oxygen (O_L) to form a hydroxyl group

or water (O_{H_2O}) to form a hydronium ion. By computing proton binding energy (E_H), we found that the O_{H_2O} site is always preferred than the lattice oxygen (Figure 6.2(b)) at the three different hydration levels examined ($WO_3 \cdot 0.33H_2O$, $WO_3 \cdot 0.5H_2O$, and $WO_3 \cdot 0.67H_2O$, corresponding to a linear density of 2.7, 4.0, and 5.2 water-mol/nm).

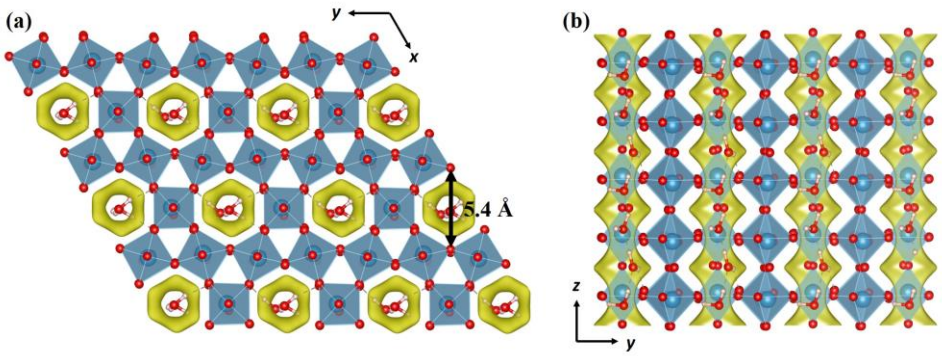

Figure 6.1. Crystal structure of *h*-WO_3 hydrate: (a) top view; (b) side view. Yellow electron-density isosurfaces (at 2.5×10^{-6} e/Å^3) indicate the 1D tunnels along the z-axis.

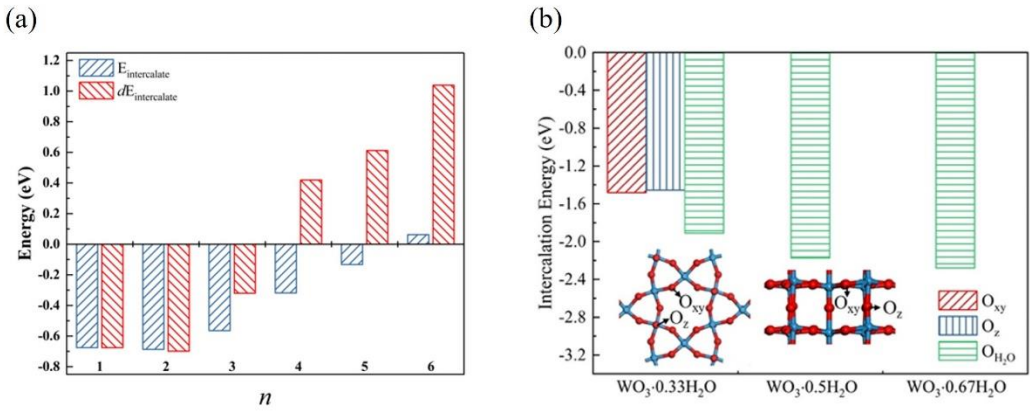

Figure 6.2 (a) Integral (E) and differential (*d*E) water intercalation energies into *h*-WO_3 as a function of hydration level *n* in $WO_3 \cdot \frac{n}{6}H_2O$. (b) Proton intercalation energy (at the level of 0.167 per WO_3) for different hydration levels. O_{xy} and O_z are two types of lattice oxygen (O_L).

6.3.2. Proton diffusivity along the water chain in *h*-WO_3.

Next, we performed FPMD simulations of proton transport along the 1D tunnel of

varying linear density of water at room temperature. To quantify proton mobility along the channel, we first calculated the time-dependent translational mean square displacement (MSD) of the O_0 (oxygen atom of the hydronium ion) from the FPMD trajectories. Then we decomposed the MSD to z direction (Figure 6.3 (c)) and calculated the proton diffusivity along the tunnel ($D_{trans,z}$) based on the Einstein relation. Figure 6.3 (a) shows $D_{trans,z}$ as a function of water linear density for the protonation level of 0.08 H^+ per WO_3. One can see a volcano-type curve: a maximum proton diffusivity of 4.78 $Å^2$/ps at a linear density of 4 water-mol/nm. We found the same optimal linear water density for a higher protonation level as well (Figure 6.3 (b)) for 0.17 H^+ per WO_3. Interestingly, similar linear water density was also found in other very different systems, such as single file water confined in carbon nanotube (~4.0 water-mol/nm)[25, 26] or in aquaglyceroporin GlpF channel (3.5~4.5 water-mol/nm),[27] indicating its universality. FPMD simulations have also been employed as early as in 1990s to simulate proton transfer in analogs of ion channels[28] and water wires.[29]

To compare with the experimental values and other phases of WO_3, we estimated proton diffusivities at 300 K by using a diffusion model[30] and the Arrhenius equation with the experimental or DFT barrier. Our simulated proton diffusivity of 0.5 $Å^2$/ps in h-$WO_3 \cdot 0.5H_2O$ at the protonation level of 0.17 H^+ per WO_3 is comparable to the experimental value of 0.4 $Å^2$/ps in *h*-$WO_3 \cdot 0.5H_2O$;[8] our simulated proton diffusivity of 4.78 $Å^2$/ps in *h*-$WO_3 \cdot 0.5H_2O$ at the protonation level of 0.08 H^+ per WO_3 is, however, much higher. Such variation is also found in other phases of WO_3. For example, in the case of layered monoclinic WO_3 with more water content (*m*-$WO_3 \cdot H_2O$), the estimated experimental

proton diffusivity is 0.47 Å^2/ps[31] while the simulated value is 4.83 Å^2/ps.[12]

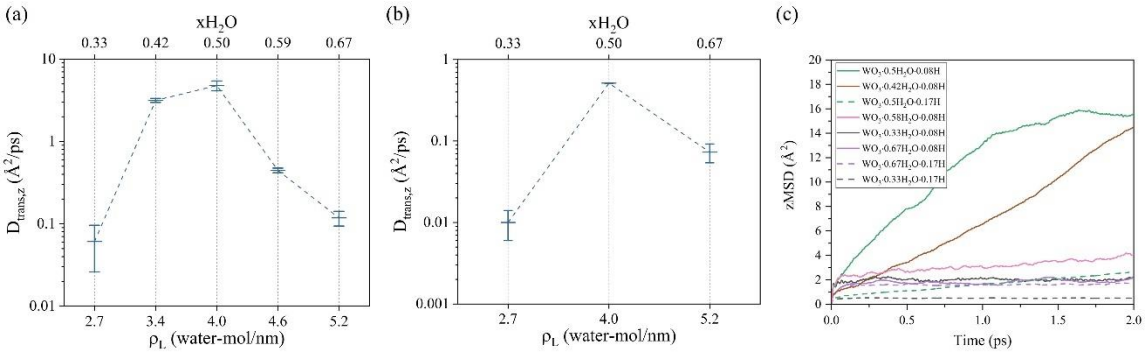

Figure 6.3. Proton diffusivity along the tunnel ($D_{trans,z}$) in *h*-WO_3 as a function of the linear water density (ρ_L) or hydration level (*x* H_2O per WO_3). Protonation level is at 0.08 H^+ per WO_3.

6.3.3. Mechanism of proton transport and role of hydrogen-bond defects along the water chain in *h*-WO_3

To understand why there is such an optimal water linear density and the mechanism of proton transport in the 1D tunnels of *h*-WO_3, we have analyzed the FPMD trajectories. At 4 water-mol/nm, we found that the intercalated protons still follow the Grotthuss-type diffusion along the water chain confined in the 1D tunnels of *h*-WO_3, as shown in Figure 6.4. One can see that the water molecules in the channel usually have two neighbors; the 3D hydrogen-bond (HB) network in bulk water is missing here. In the 1D channel, HB defects (HBDs) play an important role in dictating proton mobility. In a perfectly oriented water chain, a water molecule acts as a donor to one neighbor and an acceptor to the other. An HBD arises when the water molecule has less than 2 nearest neighbors (type 1 HBD or HBD1) or acts as an acceptor (or donor) to both neighbors (type 2 HBD or HBD2) (Figure 6.5). Such HB defects will be a roadblock for proton hopping along the water chain and are key to understanding the optimal linear water density in 1D proton transport.

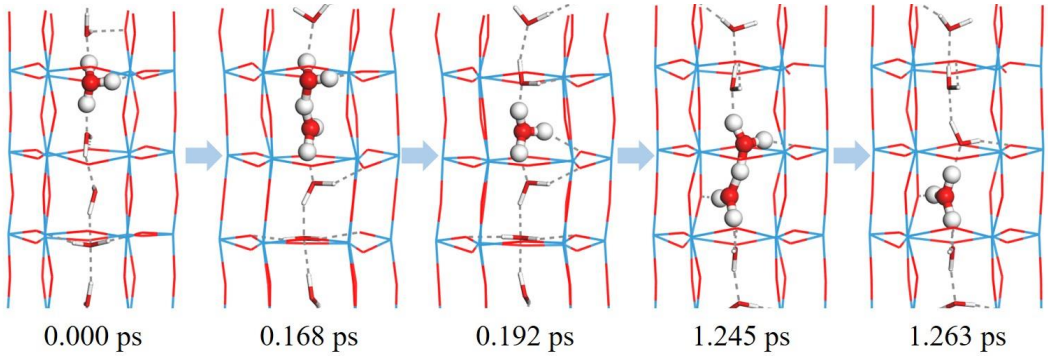

Figure 6.4. Snapshots of proton transfer along the water chain inside the 1D tunnels of *h*-WO_3 at a hydration level of 4.0 water-mol/nm. The hydronium and Zundel ions are highlighted by the ball-and-stick model. Color code: cyan, W; red, O; white, H. Only the wall of the *h*-WO_3 channel is shown.

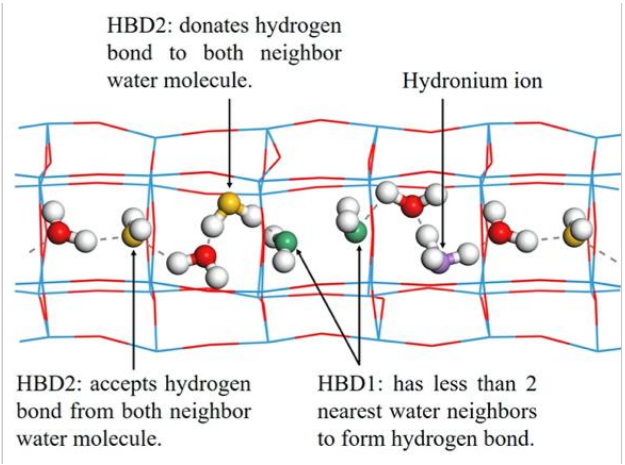

Figure 6.5 Different types of hydrogen-bonding defects (HBDs). The oxygen atom of type-1 HBD (HBD1) is shown in green; O of type 2 HBD (HBD2) is shown in yellow. The oxygen atom of the hydronium ion is shown in purple. Cyan, W; red, O; white, H.

We have tracked water molecules of both type 1 and type 2 HBDs (HBD1 and HBD2) as well as water molecules without HBD (non-HBD) by tagging their oxygen atoms, to reveal how their mobility relates to proton diffusion for the three different hydration levels (Figure 6.6). Proton motion is tracked by following the hydronium-ion oxygen. In the case of $WO_3 \cdot 0.33H_2O$ (corresponding to 2.7 water-mol/nm), HBD1 is the dominant type (Figure 6.6a,b). Both the HBDs (green) and proton (purple) are rather

stationary (Figure 6.6a) due to the gap between them (Figure 6.6b). In other words, the water chain is broken or not continuous, due to the low water density. Most of the time, proton just hops back and forth between two water molecules (dashed purple line in Figure 6.6).

In the case of $WO_3 \cdot 0.5H_2O$ (corresponding to 4.0 water-mol/nm), both types of HBDs together with non-HBD waters are all present in the tunnel (Figure 6.6c). One can see that proton is moving rapidly along the tunnel hopping from one water to another along the water chain (purple lines in Figure 6.6c, d). As proton moves through the water chain, one can also see concerted motion and interconversion of different types of water molecules (yellow and green dashed lines in Figure 6.6d). In the case of $WO_3 \cdot 0.67H_2O$ (corresponding to 5.2 mol/nm), type 2 HBD becomes dominant (yellow lines in Figure 6.6e, f) and mobilities of both HBDs and proton are significantly reduced. Apparently, now the water density is too high; the proton just hops back and forth among a few water molecules (purple lines in Figure 6.6 e,f). One can also see that there are pairs of water molecules which have similar z-positions (~6.0 Å and ~13.5 Å); in other words, they are not in a single file anymore). Figure 6.6 hence shows that the linear density at 4 water-mol/nm proves to be optimal in facilitating proton transport up and down the water chain. In higher protonation level in the channel, we found the same conclusion (Figure 6.7).

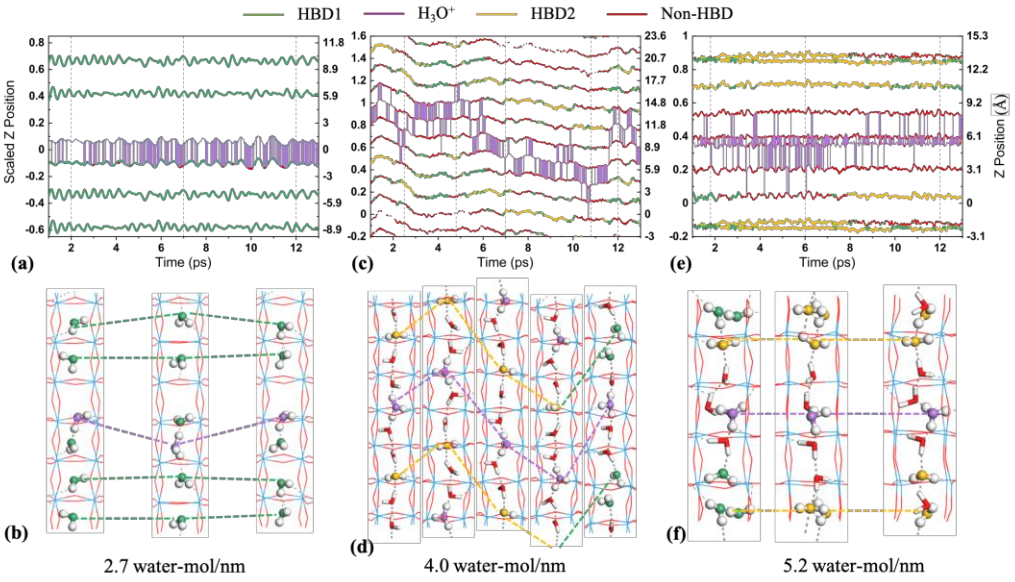

Figure 6.6. Motion of water molecules (HBD1, HBD2, and non-HBD) and hydronium ions along the 1D channels (z positions) of *h*-WO_3 (upper panel) together with a few snapshots (lower panel) at three different hydration levels: (a,b) 2.7 water-mol/nm; (c,d) 4.0 water-mol/nm; (e,f) 5.2 water-mol/nm. Protonation level is at 0.08 H^+ per WO_3.

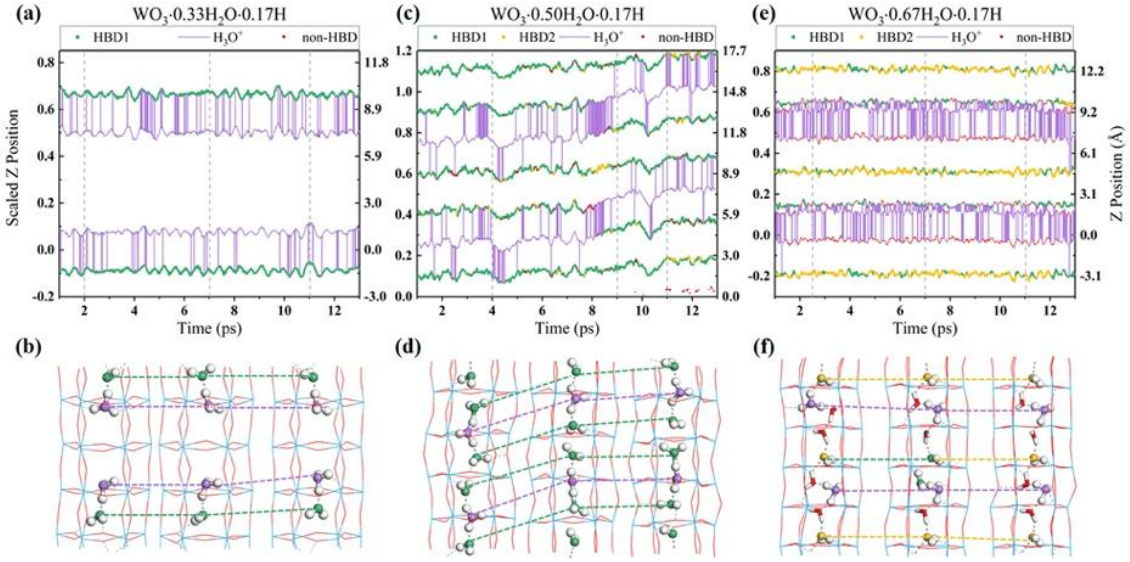

Figure 6.7 Motion of water molecules (HBD1, HBD2, and non-HBD) and hydronium ions along the 1D channels (z positions) of *h*-WO_3 (upper panel) together with a few snapshots (lower panel) at three different hydration levels: (a,b) 2.7 water-mol/nm or 0.33 H_2O per WO_3; (c,d) 4.0 water-mol/nm or 0.50 H_2O per WO_3; (e,f) 5.2 water-mol/nm or 0.67 H_2O per WO_3. Protonation level is at 0.17 H^+ per WO_3.

We further obtained the free energy profile of proton transfer at the various water densities (Figure 6.8) and found that the barrier is less than 0.3 k_bT. Such low barriers were also observed in MD simulations of proton diffusion along the water chain in carbon nanotubes,[16] indicating that the nuclear quantum effect is likely not important in this case.

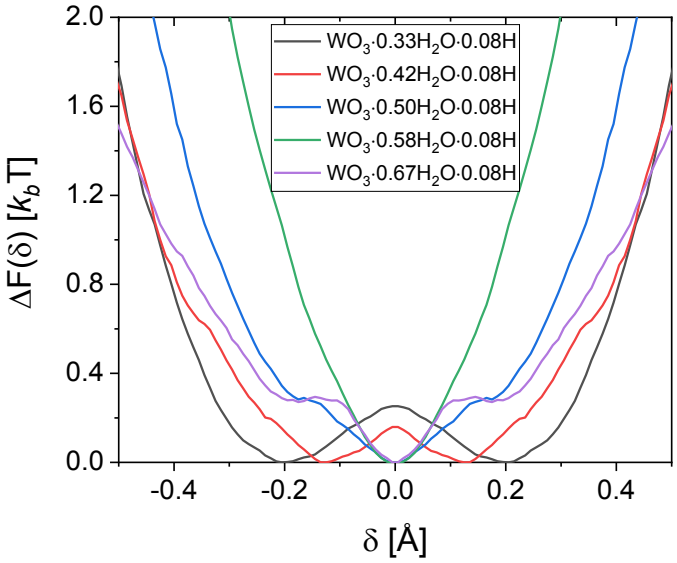

Figure 6.8 Free energy profile of proton transfer, evaluated according to F= -k_bTlnP(δ) where P(δ) is the probability distribution along the coordinate δ, defined as the difference of the H-O bond distances between the hydronium ion and the water molecule receiving the proton.

6.3.4. Impact of water rotation dynamics on proton transport along the water chain in *h*-WO_3.

Fastest proton transport along the water chain at 4 mol/nm is facilitated by the ease of interconversion of different types of water molecules, including the two types of HBDs. A key to this interconversion is the reorientation or rotation of a water molecule that would change an HBD to a non-HBD water to allow proton to pass. To quantify the water reorientation ability, we calculated the rotational diffusivity from the time-dependent

rotational mean square displacement (Figure 6.9). We found that water's rotational diffusivity in $WO_3 \cdot 0.5H_2O$ (4 water-mol/nm) at 1.69 rad^2/ps is only about 50% less than that of the bulk water (2.85 and 3.46 rad^2/ps[32, 33]). But it drastically decreased in $WO_3 \cdot 0.67H_2O$ (5 water-mol/nm) to 0.03~0.2 rad^2/ps, indicating that water rotation is greatly hindered, due to the dense packing. This rotational analysis fully supports our finding of the optimal linear water density of 4 mol/nm for proton transport.

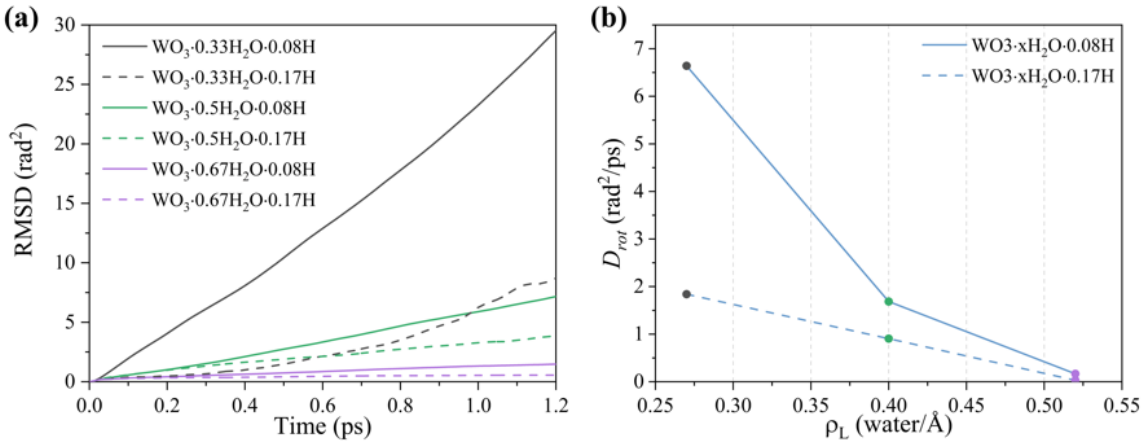

Figure 6.9 Water rotational mean square displacement (RMSD) in $WO_3 \cdot xH_2O \cdot yH$, where x and y represent hydration and protonation levels, respectively.

We have also analyzed the lattice W and O atoms along the inner surface or wall of the channel in WO_3 with the H_2O/H^+ along the water chain. There are mainly two types of interaction between H_2O/H^+ and lattice W/O along the channels: (a) coordination of water O to the lattice W atom along the channel ($W\text{-}O_{aq}$); (b) hydrogen bonding of H from water/hydronium to lattice O along the channel ($H\text{-}O_{lattice}$). We found that the $W\text{-}O_{aq}$ interaction is rather weak (Figure 6.10a), until the water density is very high at 5 water-mol/nm ($WO_3 \cdot 0.67H_2O \cdot 0.08H$) where coordination of water to W takes place, thereby slowing down water rotation and consequently proton diffusion. This is consistent with our

analysis of the water rotation dynamics at various water densities. We further found that the H-bond interaction between lattice O and hydrogen in the water chain (Figure 6.10b) shows little variation with the water density and is much weaker than the H-bond within the water chain (Figure 6.10), hence not a key factor in affecting water rotation.

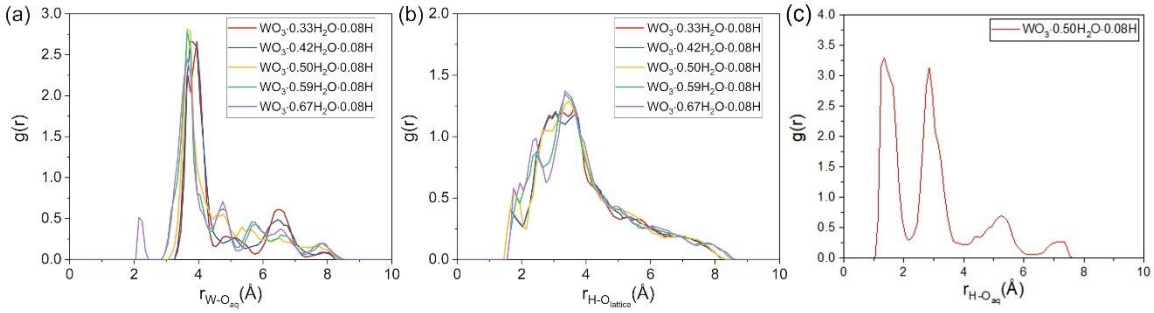

Figure 6.10 Interactions of water/hydronium with the 1D channels of *h*-WO_3 for various amounts of water inside the channel at the protonation level of 0.08 H^+/WO_3: (a) pair distribution function between O atoms from water and hydronium ion and lattice W atoms along the 1D channels; (b) pair distribution function of H atoms (from water and hydronium ion) and lattice O atoms along the 1D channels of *h*-WO_3(c) pair distribution function between H and O of two different molecules (water or hydronium ions) within the water/H^+ chain in the 1D channels of *h*-WO_3 (for the case of $WO_3{\cdot}0.50H_2O{\cdot}0.08H$).

6.3.5. Comparison with proton transport in other 1D scenarios.

It is interesting to compare proton diffusivity that we found in *h*-WO_3 (4.78 $Å^2$/ps at 4 water-mol/nm) with that in carbon nanotubes (CNTs). Previous classical molecular dynamics (CMD) simulation with empirical valence bond (EVB) model found a proton diffusivity of 4 $Å^2$/ps along the water chain confined inside CNT(6,6) at 4 water-mol/nm.[25] Bankura *et al*. applied the quantum mechanics/molecular mechanics (QM/MM) simulations to the same system and reported the proton diffusivity of 2.8 $Å^2$/ps.[34] Despite the different sizes and properties (~8 Å and hydrophobic for CNT(6,6) vs 5.4 Å and hydrophilic for *h*-WO_3) of the tunnels, the similar proton diffusivities found indicate that

the linear water density of 4 water-mol/nm is the universal and key factor to yield a similar and optimal proton diffusivity. The fast proton diffusion along the water chain is expected to occur in other tunnel oxides as well, such as α-MnO_2 which possess a one-dimensional tunnel with the width of ~5 Å.[35]

6.3.6. Experimental implications.

Besides a general mechanistic understanding of proton diffusion in tunnel oxides, our discovery of optimal water density also provides a possible strategy to design the fast proton conductor and supercapacitor electrodes[8, 9, 11] by tuning the concentration of structural water. The relation between proton diffusivity and water/proton concentration in the 1D channels also brings new physical understanding of proton transport under confinement, which is relevant in energy storage and separation technologies.

6.4. Summary and conclusions

In sum, we have used first-principles molecular dynamics to understand proton intercalation and transport in hexagonal WO_3 (h-WO_3) with 1D channels. We found an optimal linear density of four water molecules per nanometer that yields the highest proton diffusivity (~5 $Å^2$/ps) along the water chain confined in the channels of ~5 Å in diameter. Analysis of the hydrogen bond defects (HBDs) and their motion in relation to proton transfer revealed that the optimal linear water density of four water molecules per nanometer allows fast rotation of water molecules which further enables proton and HBDs to quickly move up and down the channel. This insight provides a unifying view of proton transport along a single file of water molecules confined in 1D channels.

References

1. Augustyn, V.; Simon, P.; Dunn, B., Pseudocapacitive oxide materials for high-rate electrochemical energy storage. *Energy & Environmental Science* **2014,** *7* (5), 1597-1614.

2. Fleischmann, S.; Mitchell, J. B.; Wang, R.; Zhan, C.; Jiang, D.-e.; Presser, V.; Augustyn, V., Pseudocapacitance: From Fundamental Understanding to High Power Energy Storage Materials. *Chemical Reviews* **2020,** *120* (14), 6738-6782.

3. Lukatskaya, M. R.; Dunn, B.; Gogotsi, Y., Multidimensional materials and device architectures for future hybrid energy storage. *Nature Communications* **2016,** *7* (1), 12647.

4. Trasatti, S., Physical electrochemistry of ceramic oxides. *Electrochimica Acta* **1991,** *36* (2), 225-241.

5. Yoshida, N.; Yamada, Y.; Nishimura, S.-i.; Oba, Y.; Ohnuma, M.; Yamada, A., Unveiling the Origin of Unusual Pseudocapacitance of $RuO_2 \cdot nH_2O$ from Its Hierarchical Nanostructure by Small-Angle X-ray Scattering. *The Journal of Physical Chemistry C* **2013,** *117* (23), 12003-12009.

6. Chang, K.-H.; Hu, C.-C.; Huang, C.-M.; Liu, Y.-L.; Chang, C.-I., Microwave-assisted hydrothermal synthesis of crystalline WO_3–$WO_3 \cdot 0.5H_2O$ mixtures for pseudocapacitors of the asymmetric type. *Journal of Power Sources* **2011,** *196* (4), 2387-2392.

7. Lee, S.; Lee, Y.-W.; Kwak, D.-H.; Kim, M.-C.; Lee, J.-Y.; Kim, D.-M.; Park, K.-W., Improved pseudocapacitive performance of well-defined WO_{3-x} nanoplates. *Ceramics International* **2015,** *41* (3, Part B), 4989-4995.

8. Chen, Z.; Peng, Y.; Liu, F.; Le, Z.; Zhu, J.; Shen, G.; Zhang, D.; Wen, M.; Xiao, S.; Liu, C.-P.; Lu, Y.; Li, H., Hierarchical Nanostructured WO_3 with Biomimetic Proton Channels and Mixed Ionic-Electronic Conductivity for Electrochemical Energy Storage. *Nano Letters* **2015,** *15* (10), 6802-6808.

9. Sun, W.; Yeung, M. T.; Lech, A. T.; Lin, C.-W.; Lee, C.; Li, T.; Duan, X.; Zhou, J.; Kaner, R. B., High Surface Area Tunnels in Hexagonal WO_3. *Nano Letters* **2015,** *15* (7), 4834-4838.

10. Zhu, M.; Meng, W.; Huang, Y.; Huang, Y.; Zhi, C., Proton-Insertion-Enhanced Pseudocapacitance Based on the Assembly Structure of Tungsten Oxide. *ACS Applied Materials & Interfaces* **2014,** *6* (21), 18901-18910.

11. Jiang, H.; Hong, J. J.; Wu, X.; Surta, T. W.; Qi, Y.; Dong, S.; Li, Z.; Leonard, D. P.; Holoubek, J. J.; Wong, J. C.; Razink, J. J.; Zhang, X.; Ji, X., Insights on the Proton Insertion Mechanism in the Electrode of Hexagonal Tungsten Oxide Hydrate. *Journal of the American Chemical Society* **2018,** *140* (37), 11556-11559.

12. Lin, H.; Zhou, F.; Liu, C.-P.; Ozoliņš, V., Non-Grotthuss proton diffusion mechanism in tungsten oxide dihydrate from first-principles calculations. *Journal of Materials Chemistry A* **2014,** *2* (31), 12280-12288.

13. Mitchell, J. B.; Geise, N. R.; Paterson, A. R.; Osti, N. C.; Sun, Y.; Fleischmann, S.; Zhang, R.; Madsen, L. A.; Toney, M. F.; Jiang, D.-e.; Kolesnikov, A. I.; Mamontov, E.; Augustyn, V., Confined Interlayer Water Promotes Structural Stability for High-Rate Electrochemical Proton Intercalation in Tungsten Oxide Hydrates. *ACS Energy Letters* **2019,** *4* (12), 2805-2812.

14. Clark Ii, J. K.; Paddison, S. J., Ab initio molecular dynamics simulations of water and an excess proton in water confined in carbon nanotubes. *Physical Chemistry Chemical Physics* **2014,** *16* (33), 17756-17769.

15. Habenicht, B. F.; Paddison, S. J.; Tuckerman, M. E., Ab initio molecular dynamics simulations investigating proton transfer in perfluorosulfonic acid functionalized carbon nanotubes. *Physical Chemistry Chemical Physics* **2010,** *12* (31), 8728-8732.

16. Cao, Z.; Peng, Y.; Yan, T.; Li, S.; Li, A.; Voth, G. A., Mechanism of Fast Proton Transport along One-Dimensional Water Chains Confined in Carbon Nanotubes. *Journal of the American Chemical Society* **2010,** *132* (33), 11395-11397.

17. Lee, S. H.; Rasaiah, J. C., Proton transfer and the diffusion of H^+ and OH^- ions along water wires. **2013,** *139* (12), 124507.

18. Kresse, G.; Furthmüller, J., Efficient iterative schemes for ab initio total-energy calculations using a plane-wave basis set. *Physical Review B* **1996,** *54* (16), 11169-11186.

19. Perdew, J. P.; Burke, K.; Ernzerhof, M., Generalized Gradient Approximation Made Simple. *Physical Review Letters* **1996,** *77* (18), 3865-3868.

20. Blöchl, P. E., Projector augmented-wave method. *Physical Review B* **1994,** *50* (24), 17953-17979.

21. Grimme, S., Semiempirical GGA-type density functional constructed with a long-range dispersion correction. **2006,** *27* (15), 1787-1799.

22. Nosé, S., A unified formulation of the constant temperature molecular dynamics methods. **1984,** *81* (1), 511-519.

23. Shuichi, N., Constant Temperature Molecular Dynamics Methods. *Progress of Theoretical Physics Supplement* **1991,** *103*, 1-46.

24. Bylander, D. M.; Kleinman, L., Energy fluctuations induced by the Nos'e thermostat. *Physical Review B* **1992,** *46* (21), 13756-13761.

25. Dellago, C.; Naor, M. M.; Hummer, G., Proton Transport through Water-Filled Carbon Nanotubes. *Physical Review Letters* **2003,** *90* (10), 105902.

26. Dellago, C.; Hummer, G., Kinetics and Mechanism of Proton Transport across Membrane Nanopores. *Physical Review Letters* **2006,** *97* (24), 245901.

27. Tajkhorshid, E.; Nollert, P.; Jensen, M. Ø.; Miercke, L. J. W.; O'Connell, J.; Stroud, R. M.; Schulten, K., Control of the Selectivity of the Aquaporin Water Channel Family by Global Orientational Tuning. **2002,** *296* (5567), 525-530.

28. Sagnella, D. E.; Laasonen, K.; Klein, M. L., Ab initio molecular dynamics study of proton transfer in a polyglycine analog of the ion channel gramicidin A. *Biophysical Journal* **1996,** *71* (3), 1172-1178.

29. Mei, H. S.; Tuckerman, M. E.; Sagnella, D. E.; Klein, M. L., Quantum Nuclear ab Initio Molecular Dynamics Study of Water Wires. *The Journal of Physical Chemistry B* **1998,** *102* (50), 10446-10458.

30. Kürpick, U.; Kara, A.; Rahman, T. S., Role of Lattice Vibrations in Adatom Diffusion. *Physical Review Letters* **1997,** *78* (6), 1086-1089.

31. Li, Y. M.; Hibino, M.; Miyayania, M.; Kudo, T., Proton conductivity of tungsten trioxide hydrates at intermediate temperature. *Solid State Ionics* **2000,** *134* (3), 271-279.

32. Debnath, A.; Mukherjee, B.; Ayappa, K. G.; Maiti, P. K.; Lin, S.-T., Entropy and dynamics of water in hydration layers of a bilayer. **2010,** *133* (17), 174704.

33. Farimani, A. B.; Wu, Y.; Aluru, N. R., Rotational motion of a single water molecule in a buckyball. *Physical Chemistry Chemical Physics* **2013,** *15* (41), 17993-18000.

34. Bankura, A.; Chandra, A., Hydroxide Ion Can Move Faster Than an Excess Proton through One-Dimensional Water Chains in Hydrophobic Narrow Pores. *The Journal of Physical Chemistry B* **2012,** *116* (32), 9744-9757.

35. Yang, Z.; Ford, D. C.; Park, J. S.; Ren, Y.; Kim, S.; Kim, H.; Fister, T. T.; Chan, M. K. Y.; Thackeray, M. M., Probing the Release and Uptake of Water in α-$MnO_2 \cdot xH_2O$. *Chemistry of Materials* **2017,** *29* (4), 1507-1517.

Chapter 7. High-rate proton intercalation in $WO_3 \cdot nH_2O$

7.1. Introduction

Over the past few decades, the most widely investigated approach to increase the power density of redox-active materials has been nanostructuring to decrease diffusion distances and increase the electrochemical interfacial area.[1-4] While successful in increasing power capability, this design strategy has drawbacks, mainly low volumetric energy density and propensity for parasitic side reactions due to the unconstrained porosity.[5] An emerging strategy is to find structural features that can enable fast ion transport in redox-active materials. In recent years, these include the discovery of intercalation pseudocapacitance via solid-solution intercalation in crystalline Nb_2O_5,[6] the presence of oxygen vacancies in MoO_{3-x},[7] and oxygen intercalation in perovskite oxides like $LaMnO_3$.[8] Another prominent example is the presence of confined fluids such as structural water.[9] Structural water can be found in diverse classes of materials including oxides, chalcogenides, MXenes,[10] and framework materials such as Prussian blue analogs[11-13] and metal organic frameworks.[14] It has been hypothesized that proton transport in materials with extended structural water networks may occur via the Grotthuss mechanism,[11, 15] whereby very fast (picosecond timescale) proton transport occurs by hydrogen bonding to adjacent water molecules.[16] However, it is not yet clear whether this mechanism can manifest itself in materials when proton transport is coupled to a faradaic reaction, as in electrochemical energy storage.

In order to understand the role of structural water during proton transport that is

coupled to a faradaic reaction, we have been investigating the electrochemical de/intercalation of protons in hydrated tungsten oxides, $WO_3 \cdot nH_2O$ (n = 1, 2), whose structural water content and structure is well-known (Figure 7.1).[17, 18] Recently, we found that the presence of structural water leads to a transition in the energy storage mechanism from solid-state diffusion limited in WO_3 to surface-limited (or pseudocapacitive) in $WO_3 \cdot 2H_2O$.[17] We also found that the presence of structural water minimized the electrochemically-driven deformation of $WO_3 \cdot 2H_2O$.[18]

Here, we investigate the role of structural water on the observed kinetic differences between $WO_3 \cdot nH_2O$ and WO_3 by coupling electrochemical characterization with fundamental studies of the structure and dynamics of both the solid-state structure and confined water network. Our measurements reveal that structural water in $WO_3 \cdot nH_2O$ is highly confined, which allows for rapid and facile structural transformation during electrochemical proton intercalation. We demonstrate that the facile structural transformation of $WO_3 \cdot nH_2O$ allows for reversible proton intercalation at a scan rate of 2 V s^{-1}, corresponding to a charge/discharge time of only ~ 500 ms. We hypothesize that the role of the confined water network is to stabilize the layered structure of $WO_3 \cdot nH_2O$ as it undergoes intercalation-induced phase transformations at high rates. This leads us to propose a new materials design strategy for high power, high energy density storage via the presence of confined fluids. This concept could be extended to other layered materials, such as oxides and chalcogenides via interlayer engineering.

7.2. Density functional theory (DFT) simulation details

DFT calculations with periodic boundary conditions were performed using the

Vienna *ab initio* Simulation Package (VASP).[19] An energy cutoff of 700 eV was used for plane wave basis sets. The Perdew-Burke-Emzerhof (PBE)[20] form of the generalized-gradient-approximation was used for electron exchange and correlation; the projector augmented wave (PAW)[21] method for the electron-core interaction. DFT-D3[22] was adopted to account for van der Waals interactions. The structure of $H_{0.13}WO_3 \cdot H_2O$ was simulated by a supercell containing 16 $WO_3 \cdot H_2O$ formula units and two protons, considering both bridging (O_b) and terminal oxygen sites (O_t) for protonation. The Brillouin zone was sampled by a 2 × 2 × 2 Monkhorst-Pack k-point mesh. Structural relaxation was carried out with a force convergence criterion of 0.01 eV/Å. First pricinples molecular dynamics (FPMD) simulations were performed in canonical ensemble (NVT) with a Nosé thermostat at 300 K for 10 ps with a 1 fs time step.[23-25] The vibrational density of states (VDOS) was obtained from the velocity auto-correlation function of the FPMD trajectory.

7.3. Electrochemical characterization

The electrochemical intercalation of protons into $WO_3 \cdot nH_2O$ or anhydrous WO_3 can be expressed as:

$$WO_3 \cdot nH_2O;\ WO_3 + xH^+ + xe^- \leftrightarrow H_xWO_3 \cdot nH_2O;\ H_xWO_3 \quad (0 \leq x \leq 1) \quad (1)$$

where x is the extent of proton storage, with a maximum of 1. This leads to maximum gravimetric capacities of 360 C g^{-1} for $WO_3 \cdot 2H_2O$, 386 C g^{-1} for $WO_3 \cdot H_2O$, and 416 C g^{-1} for WO_3. Despite the modest gravimetric capacities, these materials serve as model systems for understanding the role of structural water during proton intercalation at fast timescales due to the stoichiometric, well-ordered water network, the fact that the same redox reaction

is present in all three phases, and that the dehydration reaction to form each phase does not affect overall particle surface area or morphology.[19] Similar surface area and morphology between the crystalline phases means that they will exhibit similar gravimetric capacitances from the formation of the electrical double layer.

To probe electrochemical proton intercalation into $WO_3 \cdot nH_2O$ under extremely short timescales (second to sub-second), we electrodeposited $WO_3 \cdot nH_2O$[26] and WO_3 thin film electrodes (~300 nm) and performed cyclic voltammetry with sweep rates (v) from 100 to 2,000 mV s^{-1} (timescales ranging from 9 s to 500 ms) in a sulfuric acid electrolyte. The high rate-electrochemical behavior of all three phases at 2 V s^{-1} (~ 500 ms charge/discharge) is shown in Figure 7.1d. In line with our previous electrochemical characterization with thicker electrodes made with acid-precipitated particles,[17] the voltammetric response of the two hydrated structures is more reversible than for WO_3. The capacity as a function of sweep rate is quantified in Figure 7.1e. At these extremely fast timescales for electrochemical energy storage, $WO_3 \cdot nH_2O$ stores more protons than WO_3. It is important to note that according to our prior study,[17] the capacity of WO_3 is initially higher than $WO_3 \cdot nH_2O$ but decays rapidly with increasing rates. For $WO_3 \cdot 2H_2O$ and $WO_3 \cdot H_2O$, the similarities of the voltammetry and capacity retention indicate that the proton storage mechanisms are similar. Both hydrated phases exhibit ~ 90% retention from 100 mV s^{-1} to 2 V s^{-1}, while that of the anhydrous phase is only 60%. To investigate the role of structural water in the observed kinetic differences, the electrochemically-driven structural transformations of $WO_3 \cdot 2H_2O$ and WO_3 were investigated with *operando* X-ray diffraction (XRD).

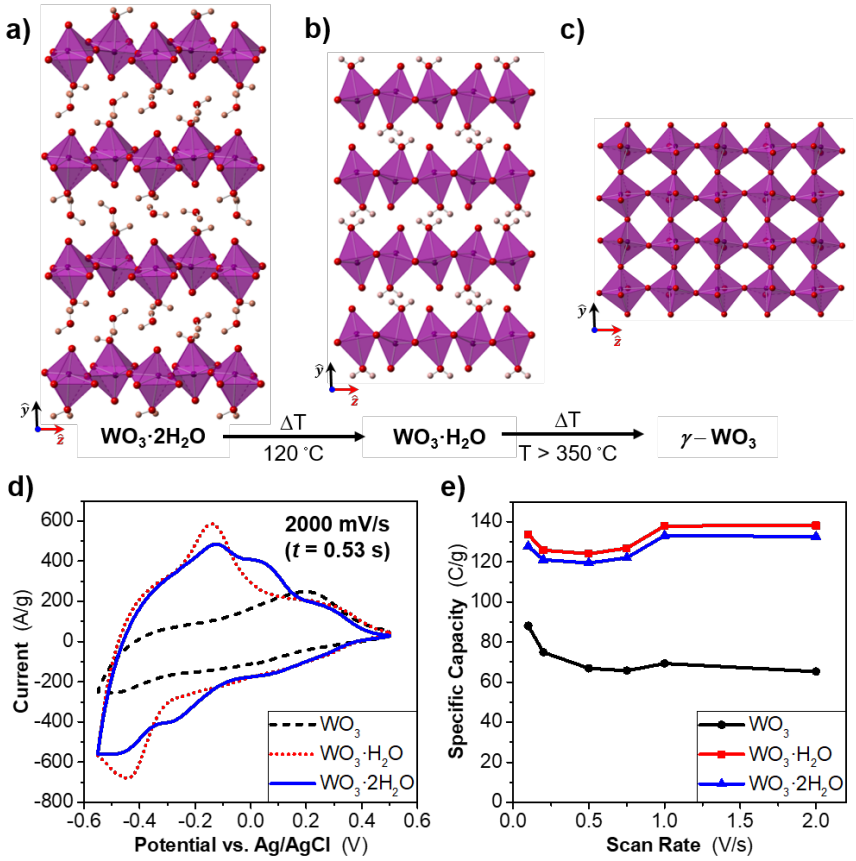

Figure 7.1 Crystal Structures and Electrochemical Proton Intercalation at Second and Sub-Second Timescales. Crystal structures of (a) monoclinic $WO_3 \cdot 2H_2O$, (b) orthorhombic $WO_3 \cdot H_2O$, and (c) monoclinic γ-WO_3. (d) Electrochemical proton intercalation of each phase in 0.5 M H_2SO_4 at 2 V s^{-1}. (e) Specific capacity versus sweep rate shows the improved capacity retention of the layered, hydrated structures at second and sub-second timescales.

7.4. electrochemically-driven structural transformations

Faradaic electrochemical energy storage inevitably leads to structural changes that may be accompanied with phase transitions.[27, 28] These structural transformations are often the rate-limiting steps for electrochemical energy storage with intercalation-based materials.[29, 30] In order to probe the electrochemically-induced structural transformations of $WO_3 \cdot 2H_2O$ and WO_3, we performed *operando* synchrotron XRD at different cyclic voltammetry sweep rates. Of the two hydrated phases, only the $WO_3 \cdot 2H_2O$ was

characterized due to the similarity of their electrochemical responses. Here, we utilized higher mass loading slurry-type electrodes made from acid-precipitated particles to ensure sufficient signal from the XRD experiment.

Figure 7.2 shows the one-dimensional diffraction patterns of $WO_3 \cdot 2H_2O$ and WO_3 as a function of time and potential at sweep rates of 1 and 100 mV s^{-1}. As observed in our previous *ex situ* XRD experiments,[18] the layered, hydrated structure undergoes a reversible phase transition with electrochemical proton de/intercalation. This is indicated by the reversible merging of the two sets of peaks at ~ 13.5° and 15.5° 2θ when the extent of proton intercalation in $H_xWO_3 \cdot 2H_2O$ is ~ 0.04, which is concomitant with the cathodic/anodic redox peaks at ~ 0 V vs. Ag/AgCl (Figure 7.2a). The peak merging is attributed to lattice distortions within the two-dimensional $WO_5(OH_2)$ layers toward a more symmetric orthorhombic structure.[31, 32] The transformation begins with $x \sim 0.02$ and is practically complete at $x \sim 0.04$, which corresponds to a full transformation in just 40 s. Interestingly, we find that the (010) peak at ~ 7.5°, signifying the interlayer spacing (6.96 Å), does not shift or change intensity with proton de/intercalation. When the sweep rate is increased to 100 mV s^{-1} (charge/discharge times < 10 sec), the reversible phase transition is still present with a faster transformation time of just 7 s (Figure 7.2c), and the interlayer spacing remains constant.

These results are significant because the intercalation pseudocapacitive charge storage has been previously hypothesized to only occur in materials that do not undergo phase transformations.[33] We hypothesize that the stability of the interlayer indicates that the confined water molecules isolate the electrochemically-driven structural

transformations to two dimensions within the $WO_5(OH_2)$ octahedral network, leading to facile ion transport within the structure. To determine whether similar structural stability is present in $WO_3 \cdot H_2O$, we performed *ex situ* XRD of $H_{0.1}WO_3 \cdot H_2O$ (Figure 7.3) and observed a slight decrease in the interlayer spacing, ~ 0.6 %. This is commensurate with the interlayer spacing change for proton intercalation into the well-known pseudocapacitive oxide, birnessite $MnO_2 \cdot nH_2O$ (~ 1 % per 0.1 mol of e^-)[34] and again highlights the stability of the structural water network in $WO_3 \cdot nH_2O$.

The kinetics of the structural response in WO_3 are drastically different as compared to $WO_3 \cdot 2H_2O$ (Figure 7.2b). However, even at a proton content of $x \sim 0.07$, the structural transformation to the protonated tetragonal structure of H_xWO_3[35-37] is incomplete even after 240 s. The extended two-phase region between γ-WO_3 and tetragonal H_xWO_3 indicates sluggish phase transformation kinetics in the absence of a confined interlayer water network. This is likely the rate-limiting process that prevents fast transport of protons through the anhydrous material. The inability of the WO_3 structure to respond to electrochemical proton intercalation at fast rates is especially evident by the lack of structural transformation at 100 mV s^{-1} (Figure 7.2d). The structure is in effect "frozen" at these faster charge/discharge times ($t < 10$ s) and unable to rapidly accommodate protons. We hypothesize that the presence of these confined water networks in the interlayer of $WO_3 \cdot 2H_2O$ enables the facile, basically 2D, phase transformation observed during electrochemical proton intercalation by effectively stabilizing the interlayer and restricting structural changes to two dimensions.

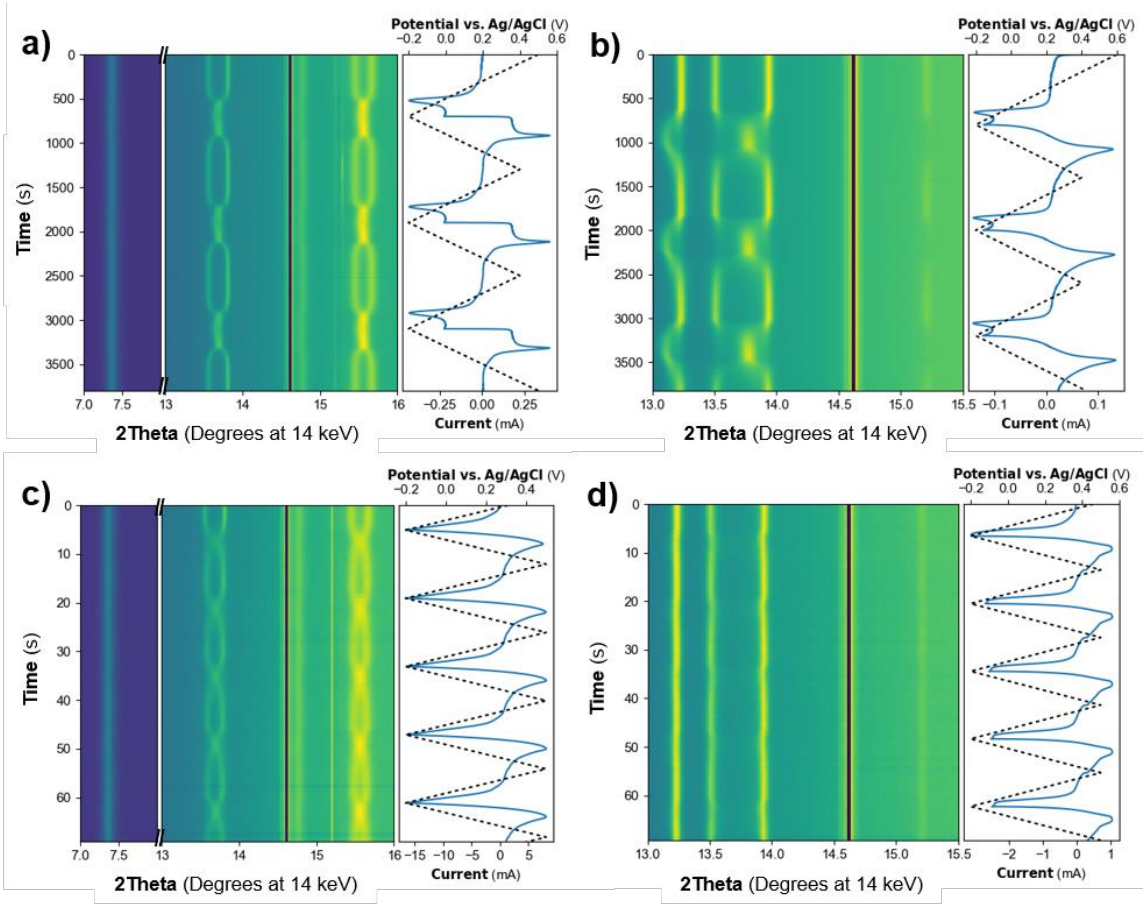

Figure 7.2 *Operando* XRD of Electrochemically-Induced Phase Transformations in $WO_3 \cdot 2H_2O$ and WO_3. Synchrotron XRD color maps of $WO_3 \cdot 2H_2O$ (a, c) and WO_3 (b, d) as a function of electrochemical cycling at 1 (a, b) and 100 (c, d) mV s^{-1}. The black line at ~ 14.5° 2θ indicates an edge in the area detector. The applied potential as a function of time is depicted by the black dashed lines at the right of each plot, and the resulting current is shown by the blue solid curves.

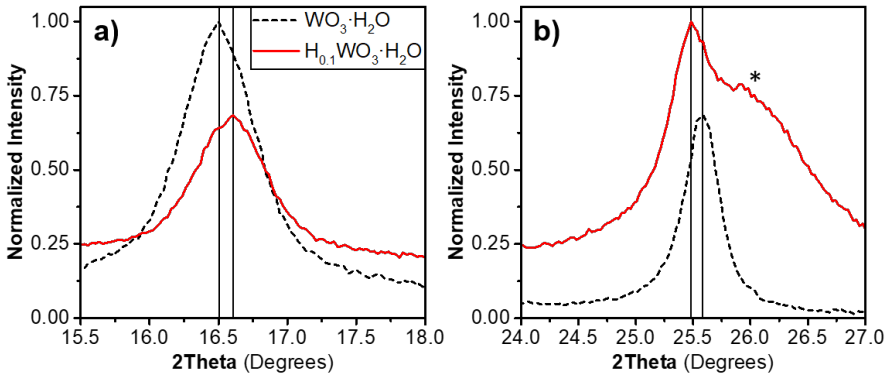

Figure 7.3 *Ex Situ* XRD of $WO_3 \cdot H_2O$. XRD patterns of pristine $WO_3 \cdot H_2O$ (*black, dashed curve*) and $H_{0.1}WO_3 \cdot H_2O$ (*red, solid curve*). (a) Shift of the (020) reflection signifies slight contraction (~ 0.6%) of the interlayer spacing upon proton intercalation into $WO_3 \cdot H_2O$. (b) Slight shift in the (111) reflection indicates a slight increase in the interplanar spacing. The additional peak indicated by the (*) is due to the Mylar film used to protect the electrode from air oxidation.

7.5. Proton binding site

Ex situ INS was utilized to determine the intercalated proton binding site in $H_{0.13}WO_3 \cdot H_2O$. The intercalated protons lead to the presence of a new peak at ~ 150 meV and a shift in the O-H stretching mode peak to ~ 420 meV, as compared to the pristine electrode (Figure 7.4b, c). Both the total and projected vibrational densities of states (VDOS) from the FPMD of the protonated $WO_3 \cdot H_2O$ reveal that the peak at ~ 150 meV is consistent with the W-O-H bending mode of a proton present at the bridging oxygen (O_b) site (Figure 7.4d) although the storage of protons at a terminal oxygen is also possible (O_t). DFT calculations of $H_{0.13}WO_3 \cdot 2H_2O$ indicate that intercalated protons prefer only the O_b sites, which is in line with the lack of interlayer spacing change observed from *operando* XRD. These proton site preferences are in agreement with prior DFT calculations on $H_xWO_3 \cdot nH_2O$,[38] which also indicate a rotationally enabled proton transport mechanism that may be active in the present materials. The location of the intercalated proton in

$H_{0.1}WO_3$ in the bridging site is already well-known,[39] and our INS and density functional theory (DFT) results are in line with these prior observations (Figure 7.5). The *ex situ* INS and DFT results indicate that $WO_3 \cdot nH_2O$ and WO_3 store protons at bridging oxygen sites, and thus we hypothesize that the significant differences in electrochemical proton intercalation kinetics are attributed to differences in the ability of the respective solid state structures to undergo necessary structural transformations.

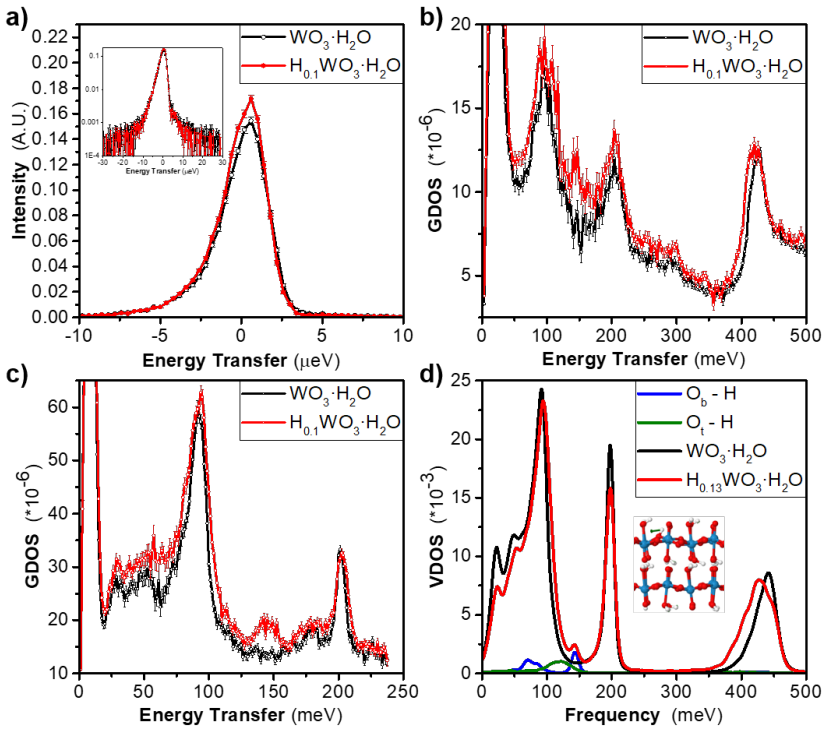

Figure 7.4 Proton Intercalation Site in $WO_3 \cdot nH_2O$. (a) *Ex situ* QENS of an $WO_3 \cdot H_2O$ electrode in the pristine ($WO_3 \cdot H_2O$, *black*) and intercalated ($H_{0.1}WO_3 \cdot H_2O$, *red*) states at T = 300 K and Q = 0.9 $Å^{-1}$ (the asymmetry of the elastic peak is due to the intrinsically asymmetric resolution function often characteristic of spallation-source based neutron spectrometers). The intensity is plotted in logarithmic scale in the inset to highlight the quasielastic scattering "wings" signal. *Ex situ* INS of the same electrodes at T = 5 K with incident energies E_i = (b) 600 and (c) 250 meV. Generalized vibrational density of states (GDOS) versus energy transfer depicts the vibrational modes of protons in $WO_3 \cdot H_2O$. *Ab initio* molecular dynamics simulations of the vibrational density of states (VDOS, (d)) show the effect of protons at the terminal (O_t, *green*) and bridging (O_b, *blue*) oxygen atoms to the overall spectrum.

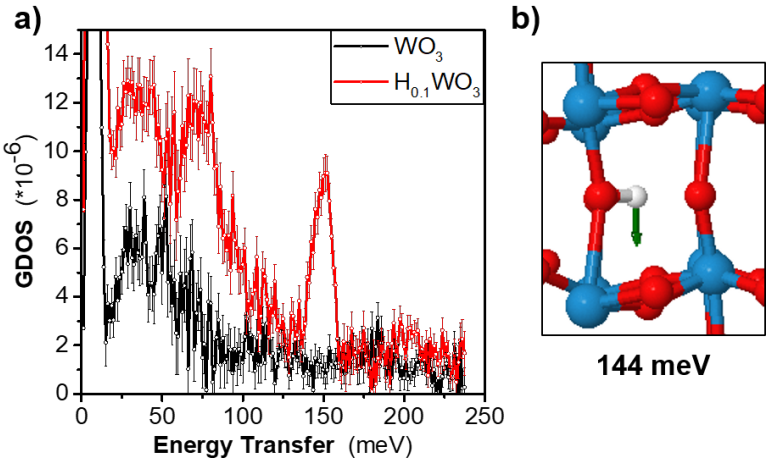

Figure 7.5 Proton Storage Site in WO_3. (a) *Ex situ* INS spectra of WO_3 (*black*) and electrochemically intercalated $H_{0.1}WO_3$ (*red*) with incident energy (E_i) of 250 meV at T = 5 K. $H_{0.1}WO_3$ exhibits additional density of states (GDOS) at ~ 150 meV, corresponding to the bending mode of a W-O-H bond formed by the electrochemically intercalated proton and a bridging oxygen. The vertical bars on each data point indicate the mean ± standard deviation. (b) DFT normal-mode analysis of the W-O-H bending mode at ~ 150 meV. Blue atoms indicated W metal centers bridged by oxygen atoms (red). The green arrow indicates the bending mode of the intercalated proton (white).

7.6. Conclusions

Here, we present the unexpected discovery of the role of structural water in crystalline transition metal oxide hydrates in enabling both structural flexibility and stability for highly reversible, sub-second electrochemical intercalation. The confined and ordered nature of the structural water, as probed with neutron scattering and SSNMR, coupled with *operando* XRD results, demonstrate the ability for $WO_3 \cdot nH_2O$ to undergo extremely facile phase transformations while allowing little-to-no changes in the interlayer spacing. The results presented here indicate that the confined water networks in crystalline hydrates such as $WO_3 \cdot nH_2O$ isolate the structural transformations to two dimensions, leading to more facile electrochemically-driven structural transformations. We hypothesize that this is the mechanism behind the exceptional, sub-second proton intercalation ability

of $WO_3 \cdot nH_2O$, and highlights the importance of electrochemically-driven phase transformations in determining kinetic limitations in energy storage intercalation reactions. They also point to the possibility of tuning solid-state structures to minimize electrochemically-driven structural distortions via the incorporation of confined fluids such as structural water, thus introducing a new materials design strategy for fast, pseudocapacitive energy storage.

References

1. Bruce, P. G.; Scrosati, B.; Tarascon, J.-M., Nanomaterials for Rechargeable Lithium Batteries. **2008,** *47* (16), 2930-2946.

2. ARICÒ, A. S.; BRUCE, P.; SCROSATI, B.; TARASCON, J.-M.; SCHALKWIJK, W. V., Nanostructured materials for advanced energy conversion and storage devices. In *Materials for Sustainable Energy*, pp 148-159.

3. Manthiram, A.; Vadivel Murugan, A.; Sarkar, A.; Muraliganth, T., Nanostructured electrode materials for electrochemical energy storage and conversion. *Energy & Environmental Science* **2008,** *1* (6), 621-638.

4. Rauda, I. E.; Augustyn, V.; Dunn, B.; Tolbert, S. H., Enhancing Pseudocapacitive Charge Storage in Polymer Templated Mesoporous Materials. *Accounts of Chemical Research* **2013,** *46* (5), 1113-1124.

5. Palacin, M. R.; Simon, P.; Tarascon, J. M., Nanomaterials for electrochemical energy storage: the good and the bad. *2016* **2016,** *63* (3), 7 %J Acta Chimica Slovenica.

6. Augustyn, V.; Come, J.; Lowe, M. A.; Kim, J. W.; Taberna, P.-L.; Tolbert, S. H.; Abruña, H. D.; Simon, P.; Dunn, B., High-rate electrochemical energy storage through Li^+ intercalation pseudocapacitance. *Nature Materials* **2013,** *12* (6), 518-522.

7. Kim, H.-S.; Cook, J. B.; Lin, H.; Ko, Jesse S.; Tolbert, Sarah H.; Ozolins, V.; Dunn, B., Oxygen vacancies enhance pseudocapacitive charge storage properties of MoO_{3-x}. *Nature Materials* **2017,** *16* (4), 454-460.

8. Mefford, J. T.; Hardin, W. G.; Dai, S.; Johnston, K. P.; Stevenson, K. J., Anion charge storage through oxygen intercalation in $LaMnO_3$ perovskite pseudocapacitor electrodes. *Nature Materials* **2014,** *13* (7), 726-732.

9. Augustyn, V.; Gogotsi, Y., 2D Materials with Nanoconfined Fluids for Electrochemical Energy Storage. *Joule* **2017,** *1* (3), 443-452.

10. Lukatskaya, M. R.; Kota, S.; Lin, Z.; Zhao, M.-Q.; Shpigel, N.; Levi, M. D.; Halim, J.; Taberna, P.-L.; Barsoum, M. W.; Simon, P.; Gogotsi, Y., Ultra-high-rate pseudocapacitive energy storage in two-dimensional transition metal carbides. *Nature Energy* **2017,** *2* (8), 17105.

11. Wu, X.; Hong, J. J.; Shin, W.; Ma, L.; Liu, T.; Bi, X.; Yuan, Y.; Qi, Y.; Surta, T. W.; Huang, W.; Neuefeind, J.; Wu, T.; Greaney, P. A.; Lu, J.; Ji, X., Diffusion-free Grotthuss topochemistry for high-rate and long-life proton batteries. *Nature Energy* **2019,** *4* (2), 123-130.

12. Pasta, M.; Wessells, C. D.; Liu, N.; Nelson, J.; McDowell, M. T.; Huggins, R. A.; Toney, M. F.; Cui, Y., Full open-framework batteries for stationary energy storage. *Nature Communications* **2014,** *5* (1), 3007.

13. Mizuno, Y.; Okubo, M.; Hosono, E.; Kudo, T.; Zhou, H.; Oh-ishi, K., Suppressed Activation Energy for Interfacial Charge Transfer of a Prussian Blue Analog Thin Film Electrode with Hydrated Ions (Li^+, Na^+, and Mg^{2+}). *The Journal of Physical Chemistry C* **2013,** *117* (21), 10877-10882.

14. Hmadeh, M.; Lu, Z.; Liu, Z.; Gándara, F.; Furukawa, H.; Wan, S.; Augustyn, V.; Chang, R.; Liao, L.; Zhou, F.; Perre, E.; Ozolins, V.; Suenaga, K.; Duan, X.; Dunn, B.; Yamamto, Y.; Terasaki, O.; Yaghi, O. M., New Porous Crystals of Extended Metal-Catecholates. *Chemistry of Materials* **2012,** *24* (18), 3511-3513.

15. Whittingham, M. S., Hydrogen motion in oxides: from insulators to bronzes. *Solid State Ionics* **2004,** *168* (3), 255-263.

16. Marx, D., Proton Transfer 200 Years after von Grotthuss: Insights from Ab Initio Simulations. *ChemPhysChem* **2006,** *7* (9), 1848-1870.

17. Mitchell, J. B.; Lo, W. C.; Genc, A.; LeBeau, J.; Augustyn, V., Transition from Battery to Pseudocapacitor Behavior via Structural Water in Tungsten Oxide. *Chemistry of Materials* **2017,** *29* (9), 3928-3937.

18. Wang, R.; Mitchell, J. B.; Gao, Q.; Tsai, W.-Y.; Boyd, S.; Pharr, M.; Balke, N.; Augustyn, V., Operando Atomic Force Microscopy Reveals Mechanics of Structural Water Driven Battery-to-Pseudocapacitor Transition. *ACS Nano* **2018,** *12* (6), 6032-6039.

19. Kresse, G.; Furthmüller, J., Efficient iterative schemes for ab initio total-energy calculations using a plane-wave basis set. *Physical Review B* **1996,** *54* (16), 11169-11186.

20. Perdew, J. P.; Burke, K.; Ernzerhof, M., Generalized Gradient Approximation Made Simple. *Physical Review Letters* **1996,** *77* (18), 3865-3868.

21. Blöchl, P. E., Projector augmented-wave method. *Physical Review B* **1994,** *50* (24), 17953-17979.

22. Grimme, S.; Antony, J.; Ehrlich, S.; Krieg, H., A consistent and accurate ab initio parametrization of density functional dispersion correction (DFT-D) for the 94 elements H-Pu. **2010,** *132* (15), 154104.

23. Nosé, S., A unified formulation of the constant temperature molecular dynamics methods. **1984,** *81* (1), 511-519.

24. Shuichi, N., Constant Temperature Molecular Dynamics Methods. *Progress of*

Theoretical Physics Supplement **1991,** *103*, 1-46.

25. Bylander, D. M.; Kleinman, L., Energy fluctuations induced by the Nos'e thermostat. *Physical Review B* **1992,** *46* (21), 13756-13761.

26. Pugolovkin, L. V.; Cherstiouk, O. V.; Plyasova, L. M.; Molina, I. Y.; Kardash, T. Y.; Stonkus, O. A.; Yatsenko, D. A.; Kaichev, V. V.; Tsirlina, G. A., Electrodeposited non-stoichiometric tungstic acid for electrochromic applications: film growth modes, crystal structure, redox behavior and stability. *Applied Surface Science* **2016,** *388*, 786-793.

27. Meethong, N.; Kao, Y.-H.; Tang, M.; Huang, H.-Y.; Carter, W. C.; Chiang, Y.-M., Electrochemically Induced Phase Transformation in Nanoscale Olivines $Li_{1-x}MPO_4$ (M = Fe, Mn). *Chemistry of Materials* **2008,** *20* (19), 6189-6198.

28. Alfaruqi, M. H.; Mathew, V.; Gim, J.; Kim, S.; Song, J.; Baboo, J. P.; Choi, S. H.; Kim, J., Electrochemically Induced Structural Transformation in a γ-MnO_2 Cathode of a High Capacity Zinc-Ion Battery System. *Chemistry of Materials* **2015,** *27* (10), 3609-3620.

29. Vassiliev, S. Y.; Levin, E. E.; Nikitina, V. A., Kinetic analysis of lithium intercalating systems: cyclic voltammetry. *Electrochimica Acta* **2016,** *190*, 1087-1099.

30. Singh, G. K.; Ceder, G.; Bazant, M. Z., Intercalation dynamics in rechargeable battery materials: General theory and phase-transformation waves in $LiFePO_4$. *Electrochimica Acta* **2008,** *53* (26), 7599-7613.

31. Dickens, P. G.; Kay, S. A.; Crouch-Baker, S.; Claridge, D. A., Thermochemistry of the hydrogen insertion compounds formed by the molybdic and tungstic acids $H_xMO_3 \cdot nH_2O$ (M=Mo, n=1; M=W, n=1,2). *Solid State Ionics* **1987,** *23* (1), 9-14.

32. Granqvist, C. G., Electrochromic tungsten oxide films: Review of progress 1993–1998. *Solar Energy Materials and Solar Cells* **2000,** *60* (3), 201-262.

33. Augustyn, V.; Simon, P.; Dunn, B., Pseudocapacitive oxide materials for high-rate electrochemical energy storage. *Energy & Environmental Science* **2014,** *7* (5), 1597-1614.

34. Kuo, S.-L.; Wu, N.-L., Investigation of Pseudocapacitive Charge-Storage Reaction of $MnO_2 \cdot nH_2O$ Supercapacitors in Aqueous Electrolytes. *Journal of The Electrochemical Society* **2006,** *153* (7), A1317.

35. Strømme Mattsson, M., Cation intercalation in sputter-deposited W oxide films. *Physical Review B* **1998,** *58* (16), 11015-11022.

36. Zhong, Q.; Dahn, J. R.; Colbow, K., Lithium intercalation into WO_3 and the phase diagram of Li_xWO_{-3}. *Physical Review B* **1992,** *46* (4), 2554-2560.

37. Ampe, B.; Leroy, J.; Thomas, D.; Tridot, G. J. R. D. C. M., CONTRIBUTION TO STUDY OF SYSTEMS WO AND WVO. **1968,** *5* (4), 801-&.

38. Lin, H.; Zhou, F.; Liu, C.-P.; Ozoliņš, V., Non-Grotthuss proton diffusion mechanism in tungsten oxide dihydrate from first-principles calculations. *Journal of Materials Chemistry A* **2014,** *2* (31), 12280-12288.

39. Dickens, P.; Whittingham, M. J. Q. R., Chemical Society, The tungsten bronzes and related compounds. **1968,** *22* (1), 30-44.

Chapter 8. Fast proton insertion in Layered $H_2W_2O_7$

8.1. Introduction

Electrochemical energy storage (EES) devices such as Li-ion batteries have profoundly changed our ways of communication, work, and entertainment. Their continued development, including the search for materials and mechanisms that could enable simultaneous high power and high energy density, has been termed the "holy grail" of EES.[1] Electrochemical insertion remains the best EES mechanism for optimizing both electrode capacity and kinetics. In this regard, there are renewed interests in the electrochemical insertion of protons due to their small size and possibility for correlated transport via hydrogen bonding. One common feature of fast proton conductors is the presence of structural water. In some materials, structural water is proposed to enable fast proton transport via a solid-state Grotthuss mechanism.[2, 3] In other materials, such as $WO_3 \cdot nH_2O$ (n = 1 and 2), structural water appears to minimize the extent of electrochemically-induced structural deformation.[4-6] While the benefits of structural water on electrochemical proton insertion are evident, materials that can simultaneously satisfy the matrices of high energy, high power, low cost, long lifetime, and sustainability are rare. This scarcity of existing materials brings up the need to explore unconventional methods to synthesize materials that cannot be accessible via direct routes.

Topochemical reactions can be used to convert a thermodynamically stable phase into a related metastable phase by selectively etching away arrays of atoms while retaining much of the bonding in the precursor.[7-9] The selective etching of MAX phases (where M

is a transition metal, A is an element such as Al, Si, Sn, In, Ga, and X is C and/or N)[10] into MXenes is a prominent example of soft chemistry used to prepare metastable 2D materials. In particular, Ti_3C_2 MXene shows pseudocapacitive proton storage in acidic electrolytes with high capacity retention up to sub-second charge/discharge timescales and cycling stability of over 10,000 cycles.[11, 12] MXenes are not the only example of highly efficient metastable materials for proton insertion. Perez *et al*. utilized selective etching of Li from Li_3IrO_4 to synthesize a new protonated phase, $H_{3+x}IrO_4$. This material showed highly reversible proton insertion kinetics with up to ~ 1.7 e^- stored per Ir.[13] Later, Zhang *et al*. extended this method to the Ruddlesden-Popper phase Sr_2IrO_4 and prepared $H_{3.6}IrO_4 \cdot 3.7H_2O$.[14] Fleischmann *et al*. found that micron-scale $H_2Ti_3O_7$ derived from $Na_2Ti_3O_7$ exhibits bulk proton insertion up to 0.8 H^+ per formula unit.[15] These examples highlight that metastable materials derived from selective ion etching of high-temperature precursors open up a host of new structures and compositions for EES applications. In the case of transition metal oxides, those with layered perovskite structures such as Dion-Jacobson and Aurivillius phases that contain a soluble cation provide significant opportunities for creating novel metastable materials for proton insertion-based EES.[7, 8, 16]

In an Aurivillius phase, slabs of perovskite-like $[A_{n-1}B_nO_{3n+1}]^{2-}$, where A and B are cations and n is the number of perovskite blocks, are separated by layers of $[Bi_2O_2]^{2+}$.[17] In $Bi_2W_2O_9$, the perovskite A-sites are vacant and so the structure consists of $[W_2O_7]^{2-}$ layers separated by $[Bi_2O_2]^{2+}$. Schaak and Mallouk discovered $H_2W_2O_7$ via acid leaching of $Bi_2W_2O_9$;[18] the topochemical nature of the reaction was identified through electron microscopy.[19] Proton insertion into $H_2W_2O_7$ (which can also be written as $W_2O_6 \cdot H_2O$) was

first reported by Kim *et al*., with a specific capacity of ~60 mAh g^{-1} (0.5 e^- per W) at a rate of 5C (12-min charge/discharge time) and almost 100% capacity retention after 1,000 cycles.[20] Despite this promising proton insertion behavior, relatively little is known about the structure or energy storage mechanism of $H_2W_2O_7$. Our prior investigations of proton insertion into layered $WO_3 \cdot 2H_2O$ (obtained via direct synthesis) showed the importance of structural water for fast kinetics.[4-6] However, this material has a low theoretical specific capacity due to the large weight fraction of water (13 wt.%). There are two potential benefits of $H_2W_2O_7$ for enabling fast insertion kinetics and high capacity: its bilayered structure could host more proton insertion sites and it contains structural water (4 wt.%).

In this work, we demonstrate that $H_2W_2O_7$, a metastable material synthesized via selective etching of the Aurivillius-related $Bi_2W_2O_9$, can be used as an electrode for high power proton-based energy storage. We perform comprehensive structural characterization to obtain a high-fidelity crystal structure of $H_2W_2O_7$ based on analysis of X-ray diffraction (XRD), neutron pair distribution function (neutron PDF), high-angle annular dark-field scanning transmission electron microscopy (HAADF-STEM), and Raman spectroscopy, coupled with atomistic modeling from density functional theory (DFT). Electrochemical characterization using cyclic voltammetry in a sulfuric acid electrolyte showed a capacity retention of ~80% at 1,000 mV s-1 (1.5-sec charge/discharge time) as compared to 1 mV s-1 (~16-min charge/discharge time). Based on analysis of the cyclic voltammetry peak current, the proton insertion kinetics in the micron-scale particles were limited by finite-space diffusion. Cyclability at 20 mV s-1 (~23-sec charge/discharge time) showed capacity retention of 89% at 100,000 cycles. The insertion mechanism was studied by ex situ XRD,

in situ Raman spectroscopy, and DFT calculations. These results indicated that proton storage occurs at the terminal oxygen sites within the hydrated interlayer. Lastly, optical micrographs collected during in situ Raman spectroscopy showed reversible, multicolor electrochromism, with color changes from pale yellow to blue, purple, and lastly, orange as a function of proton content in $H_2W_2O_7$ in an aqueous electrolyte. These results highlight the use of selective etching of layered perovskites for the synthesis of high power, metastable transition metal oxide materials and the use of $H_2W_2O_7$ as an anode material for proton-based energy storage or aqueous electrochromic applications.

8.2. Density functional theory (DFT) simulation details

DFT calculations were performed using the Vienna *Ab initio* Simulation Package (VASP)[21] with generalized gradient approximation (GGA) for electron exchange and correlation in the form of the Perdew-Burke-Ernzerhof (PBE) functional.[22] The projector augmented wave (PAW) potentials were adopted to describe the electron-nuclei interaction.[23] An energy cutoff of 700 eV was used for plane wave basis sets and the Brillouin zone were sampled by a 4×4×1 *k*-point mesh. The van der Waals interactions were described by the DFT-D3 correction.[24] The structure of $H_{2+x}W_2O_7$ was modeled by a supercell containing 4 formula units. All degrees of freedom were relaxed until the residual forces were below 0.01 eV $Å^{-1}$. To simulate the proton insertion energetics during the electrochemical process, hydrogen atoms (H^++e^-) were added to the unit cell. The proton-binding energy on an oxygen site was calculated as $E_H = \frac{E_{H_{2+x}W_2O_7} - E_{H_2W_2O_7} - \frac{x}{2}E_{H_2}}{x}$, where $E_{H_{2+x}W_2O_7}$, $E_{H_2W_2O_7}$ and E_{H_2} are the total energy of protonated $H_{2+x}W_2O_7$, pure $H_2W_2O_7$, and H_2 molecule, respectively.

8.3. Structural Characterization

Selective etching of the Aurivillius-related $Bi_2W_2O_9$ in an aqueous acidic environment proceeds via the topotactic exchange of BiO^+ with H^+:

$$Bi_2W_2O_9 + 2HCl \xrightarrow{\Delta} H_2W_2O_7 + 2BiOCl \quad (1)$$

While the bilayer $[W_2O_7]^{2-}$ structure of $H_2W_2O_7$ and its dehydration behavior were investigated by Kudo *et al*,[18] a refined structure and positions of the light elements (H and O) have not yet been resolved. Here, an iterative approach was adopted to obtain a high-fidelity crystal structure using DFT geometry optimization and multi-modal characterization.[25] We first created a $H_2W_2O_7$ structure based on the structure of the parent $Bi_2W_2O_9$. The structure was then optimized with DFT and refined with X-ray diffraction (XRD) to obtain the long-range (average) structure. The characterization of the short-range structure, particularly distortion of W-octahedra and locations of H atoms, was obtained by combining knowledge from neutron PDF, Raman spectroscopy, and DFT. Atomic-resolution STEM imaging further verified the exact structure. The final structure is shown in Figure 8.1. Further details of the crystal structure investigation(s) may be obtained from the Fachinformationszentrum Karlsruhe, D-76344 Eggenstein-Leopoldshafen (Germany), on quoting the depository number CSD-2021260.

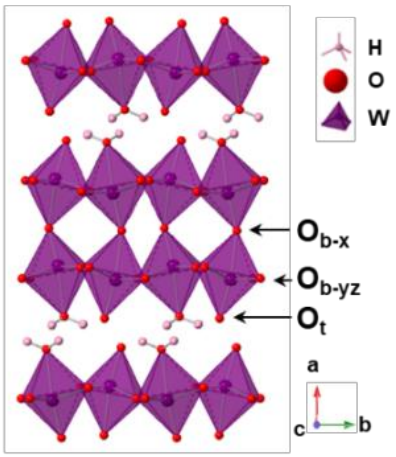

Figure 8.1 Refined crystal structure of $H_2W_2O_7$. O_{b-yz}, O_t, and O_{b-x} stand for equatorial bridging oxygen, terminal oxygen, and axial bridging oxygen, respectively. The unconventional axis is due to the $P112_1/n$ space group setting.

8.4. Electrochemical Characterization

Electrochemical characterization of $H_2W_2O_7$ was carried out by cyclic voltammetry in a 3 M H_2SO_4 electrolyte. Electrochemical proton insertion into $H_2W_2O_7$ can be described as:[20]

$$H_2W_2O_7 + xH^+ + xe^- \leftrightarrow H_{2+x}W_2O_7 \quad (2)$$

Assuming a maximum insertion of 1 H^+/e^- per W ($x = 2$) results in a capacity of 111 mAh g^{-1}. The voltammograms in Figure 8.2 a&b show the presence of a reversible redox couple with a half-wave potential ($E_{1/2}$) of -0.245 V vs. Ag/AgCl and a peak-to-peak separation (ΔE_p) of 51 ± 2 mV at 1 mV s^{-1}. The single set of well-defined redox peaks with a small peak-to-peak separation indicates that proton insertion in $H_2W_2O_7$ likely involves a first-order phase transformation. At lower sweep rates, the low Coulombic efficiency (Figure 8.3) is attributed to the onset of the hydrogen evolution reaction (HER). The Coulombic efficiency approaches 100% at higher sweep rates as the HER becomes kinetically limited.

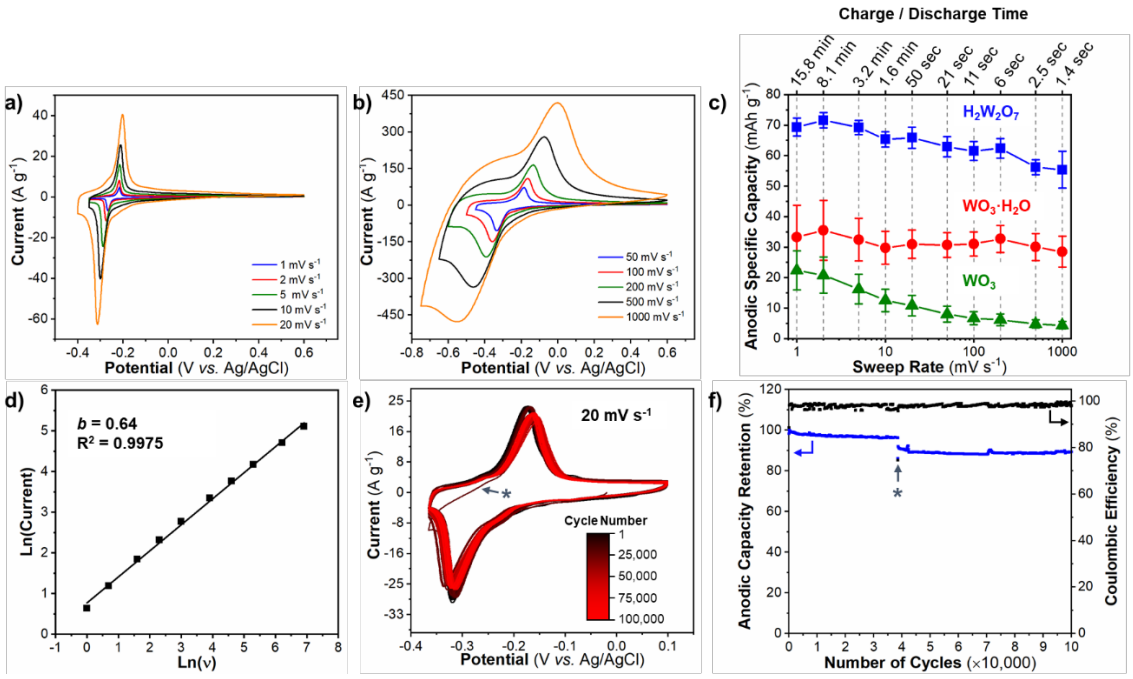

Figure 8.2 Electrochemical characterization of $H_2W_2O_7$ in 3 M H_2SO_4. a,b) Cyclic voltammograms from 1 – 20 mV s^{-1} and 50 – 1000 mV s^{-1}, c) anodic specific capacity as a function of sweep rate and the corresponding discharging time, comparing $H_2W_2O_7$, $WO_3 \cdot H_2O$, and WO_3. The average values and standard error are obtained from three electrodes of each composition. d) Sweep rate dependence of the anodic peak current in log scale for *b*-value determination from 1 – 1000 mV s^{-1}, and cyclability test: e) cyclic voltammograms of $H_2W_2O_7$ at 20 mV s^{-1} to showcase the stability of this material during cycling. Presented is every 1,000th cycle out of 100,000 cycles. f) Anodic capacity retention and Coulombic efficiency as a function of cycle number for 100,000 cycles. The asterisk symbol (*) indicates the first cycle after a two-month pause of experiment due to the COVID-19 pandemic.

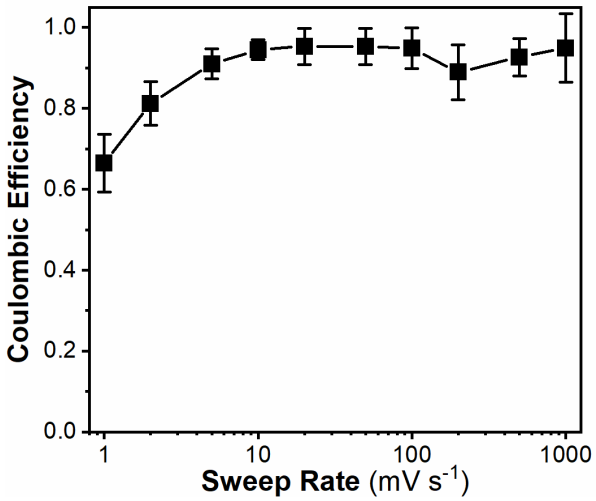

Figure 8.3 Coulombic efficiency of $H_2W_2O_7$ in 3 M H_2SO_4 from 1 to 1,000 mV s^{-1}, corresponding to the cyclic voltammograms in Figure 8.2 a&b. Error bars represent the standard deviation obtained from measurements performed on three separate electrodes.

$H_2W_2O_7$ showed a specific capacity of ~70 mAh g^{-1} at 1 mV s^{-1} (~16-min charge/discharge time, ~1.25 e^- per formula unit) and retained 80% capacity at 1,000 mV s^{-1} (~1.5-sec charge/discharge time, ~1 e^- per formula unit). Usually, this type of rate capability is only seen in pseudocapacitive materials undergoing minor structural transitions such as $WO_3 \cdot H_2O$,[6] which had 86% capacity retention at 1,000 mV s^{-1} but half the capacity of $H_2W_2O_7$ (Figure 8.2c). In addition, the $WO_3 \cdot H_2O$ had the kinetic advantage of a much smaller particle size, ~200 nm in diameter and 10 nm in thickness,[26] compared to the micron-sized $H_2W_2O_7$. This comparison showcases the high-power capability of $H_2W_2O_7$ even with large particle sizes, which are beneficial for volumetric capacity and decreased parasitic side reactions. WO_3 obtained via dehydration of $H_2W_2O_7$ has the same particle size (Figure 8.4 c&d) but significantly worse charge storage performance, with ~22 mAh g^{-1} at 1 mV s^{-1} and only 20% capacity retention at 1,000 mV s^{-1}. These results highlight the benefits of the metastable $H_2W_2O_7$ derived from selective etching: lower

water content than $WO_3 \cdot H_2O$ leads to higher capacity, while the presence of a structural water network leads to better kinetics than WO_3.

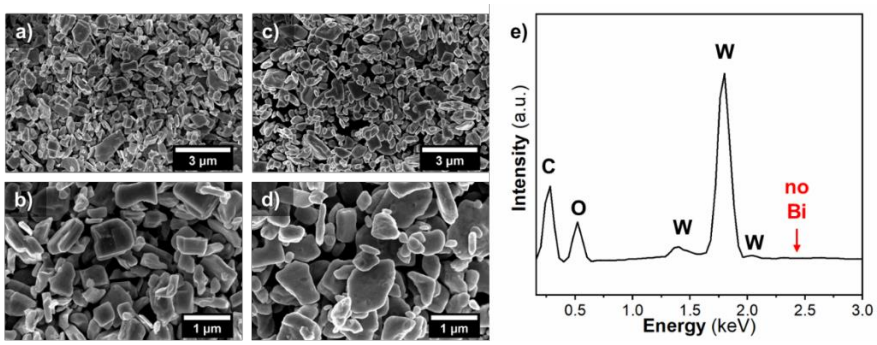

Figure 8.4 Scanning electron micrographs of a,b) $H_2W_2O_7$ and c,d) WO_3 obtained from heat treatment of $H_2W_2O_7$. e) SEM-EDS spectrum of $H_2W_2O_7$ showing that the acid exchange is complete, and no bismuth was detectable at 2.419 keV (Bi *M*-edge).

8.5. Charge storage mechanism

To understand the charge storage mechanism in $H_2W_2O_7$, we employed ex situ XRD and in situ Raman spectroscopy characterization, in conjunction with DFT simulations. Ex situ XRD of a $H_2W_2O_7$ electrode cycled to -0.5 V vs. Ag/AgCl (for a capacity of 0.5 e^- per W) in 1 M H_2SO_4 shows the shift of both *200* and *400* peaks to higher angles (Figure 8.5). These shifts represent a 2.9% contraction of the interlayer upon the insertion of 1 proton per formula unit. After cycling back to the open-circuit potential (deinsertion of 1 proton per formula unit), the *200* and *400* peaks returned to their original position. The ex situ XRD experiments present a reversible contraction of the interlayer spacing to accommodate electrochemical proton insertion in $H_2W_2O_7$. We utilized DFT to complement these results and obtain a mechanistic view of the possible proton insertion mechanism.

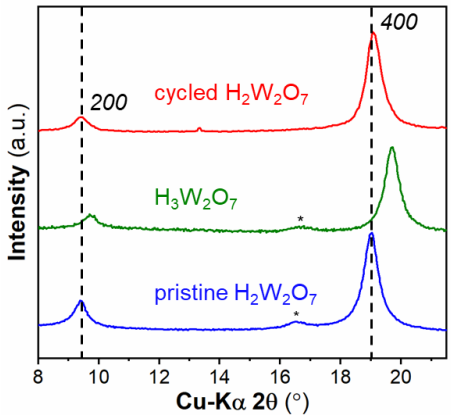

Figure 8.5 Ex situ XRD patterns of pristine, protonated, and cycled $H_2W_2O_7$ electrodes. * indicates $WO_3 \cdot H_2O$ impurity.

DFT was used to investigate proton binding sites and energies (E_H) in $H_{2+x}W_2O_7$. As illustrated in Figure 8.1, the potential oxygen sites for proton binding include two types of bridging oxygens, the axial $O_{b\text{-}x}$ and the equatorial $O_{b\text{-}yz}$, and the terminal oxygens, O_t (Figure 8.6a). Since the supercell contains 8 W atoms, adding one proton to the structure is equivalent to adding 0.25 protons per formula unit. The calculated E_H is shown in Figure 8.6b and the corresponding DFT-optimized structures (and other simulated scenarios) are compared in Figure 8.7. For x = 0.25, $O_{b\text{-}yz}$ is the most energetically favorable site for proton binding, which is only slightly more preferred than the O_t site. Interestingly, we found that at higher charge states (x = 0.5 – 1.0), the scenarios with all O_t sites for proton binding become more favorable. In other words, one expects that as more protons are inserted, some that initially bind with $O_{b\text{-}yz}$ will migrate to the more stable O_t sites. This is in contrast to the single-layer $WO_3 \cdot H_2O$, where at low proton concentrations the proton absorption site was found to be at O_t but at higher concentrations moved to $O_{b\text{-}yz}$ due to repulsive interactions between the intercalated protons in the interlayer.[6, 27]

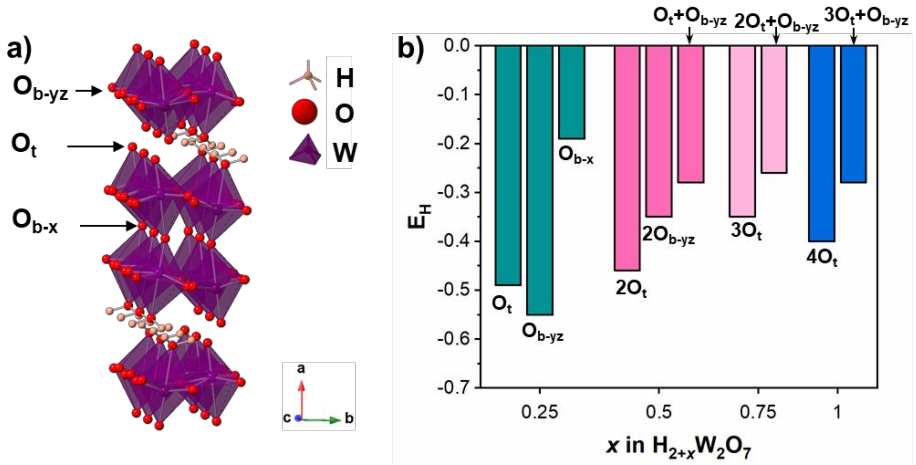

Figure 8.6 a) Refined crystal structure of $H_2W_2O_7$. $O_{b\text{-}yz}$, O_t, and $O_{b\text{-}x}$ stand for equatorial bridging oxygen, terminal oxygen, and axial bridging oxygen, respectively. The unconventional axis is due to the $P112_1/n$ space group setting. b) DFT-calculated proton binding energy at various oxygen sites in $H_{2+x}W_2O_7$ with x from 0.25 to 1. The integer before each O site indicates the number of such O sites with proton binding (based on a supercell containing 8 W atoms).

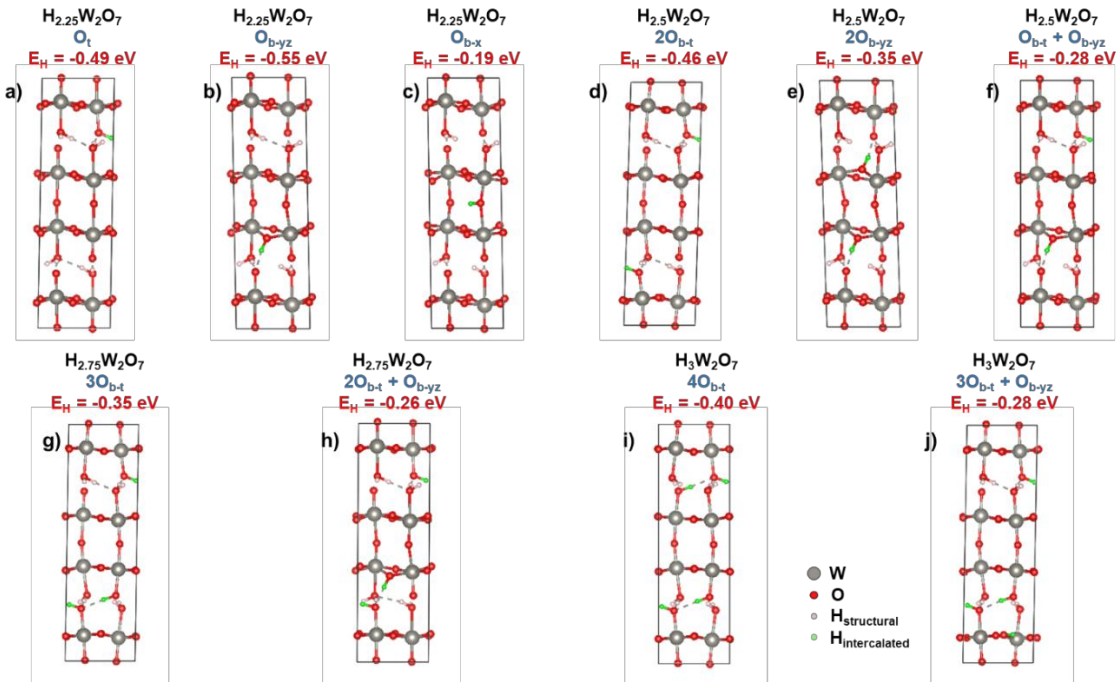

Figure 8.7 DFT-calculated proton-binding sites and energies (E_H) in $H_{2+x}W_2O_7$ at various proton concentrations. Simulated scenarios: a) x = 0.25 and H at O_t site; b) x = 0.25 and H at $O_{b\text{-}yz}$ site; c) x = 0.25 and H at $O_{b\text{-}x}$ site; d) x = 0.5 and H at two O_t sites; e) x = 0.5 and H at two $O_{b\text{-}yz}$ sites; f) x = 0.5 and H at one O_t site and one $O_{b\text{-}yz}$ site; g) x = 0.75 and H at three O_t sites; h) x = 0.75 and H at two O_t sites and one $O_{b\text{-}yz}$ site; i) x = 1 and H at four O_t sites; j) x = 1 and H at three O_t sites and one $O_{b\text{-}yz}$ site.

To verify the DFT results, we compared the *200* and *400* XRD peaks from the DFT simulation to the ex situ XRD patterns for $H_3W_2O_7$ (x = 1). As shown in Figure 8.8, the agreement between DFT ($4O_t$ model where all H bind to O_t) and XRD is excellent, both showing an interlayer contraction after proton binding. Therefore, together with the preferred energetics of the $4O_t$ model (Figure 8.6b), we conclude that O_t is the most probable proton-binding site in $H_2W_2O_7$ as it is charged to $H_3W_2O_7$ (x = 1). We further hypothesize that the difference in proton-binding sites between $H_2W_2O_7$ and $WO_3 \cdot H_2O$ is likely the main reason behind the capacity increase in $H_2W_2O_7$ as compared to $WO_3 \cdot H_2O$. In addition, Lin *et al*. predicted a fast diffusion pathway formed by the zigzag O_t sites in the interlayer of $WO_3 \cdot H_2O$.[27] The O_t sites in $H_2W_2O_7$ may provide protons with access to this pathway, leading to the high power capability observed in this material. This will be a subject of investigation in our future studies.

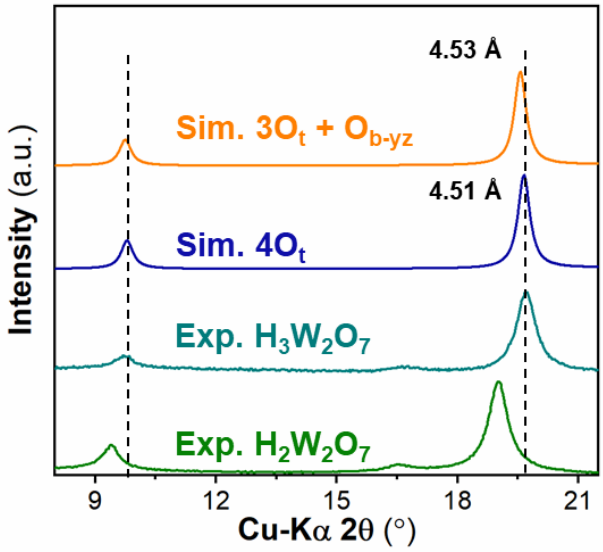

Figure 8.8 Comparison of the *200 and 400* XRD peaks from the DFT-optimized structures to the ex situ experimental data for $H_2W_2O_7$ and $H_3W_2O_7$. "Sim." stand for simulated pattern based on DFT structure; "Exp." means experimental. A Pseudo-Voigt function was used for the shape of the simulated pattern.

8.1. Conclusions

In summary, we performed comprehensive structural and electrochemical characterization of $H_2W_2O_7$ obtained by selective etching of the Aurivillius phase $Bi_2W_2O_9$. $H_2W_2O_7$ is a metastable layered material consisting of bilayers of distorted, corner-sharing tungsten octahedra with terminal coordinated structural water molecules. It can store ~70 mAh g^{-1} at 1 mV s^{-1} (~16-min discharging time) and maintain ~80% capacity at 1,000 mV s^{-1} (~1.5-s discharging time). The cycle life at 20 mV s^{-1} is well beyond 100,000 cycles. While the kinetics are limited by finite-space diffusion, the power capability and cycle life of $H_2W_2O_7$ are competitive to electrochemical capacitors. The high capacity is attributed to proton binding at terminal oxygen sites. These results render $H_2W_2O_7$ a promising material for aqueous energy storage and electrochromic applications. This material also highlights selective etching of perovskites and related phases in acid as a method to prepare metastable transition metal oxides with structural water.

References

1. Smith, P. F.; Takeuchi, K. J.; Marschilok, A. C.; Takeuchi, E. S., Holy Grails in Chemistry: Investigating and Understanding Fast Electron/Cation Coupled Transport within Inorganic Ionic Matrices. *Accounts of Chemical Research* **2017,** *50* (3), 544-548.

2. Ohkoshi, S.-i.; Nakagawa, K.; Tomono, K.; Imoto, K.; Tsunobuchi, Y.; Tokoro, H., High Proton Conductivity in Prussian Blue Analogues and the Interference Effect by Magnetic Ordering. *Journal of the American Chemical Society* **2010,** *132* (19), 6620-6621.

3. Wu, X.; Hong, J. J.; Shin, W.; Ma, L.; Liu, T.; Bi, X.; Yuan, Y.; Qi, Y.; Surta, T. W.; Huang, W.; Neuefeind, J.; Wu, T.; Greaney, P. A.; Lu, J.; Ji, X., Diffusion-free Grotthuss topochemistry for high-rate and long-life proton batteries. *Nature Energy* **2019,** *4* (2), 123-130.

4. Mitchell, J. B.; Lo, W. C.; Genc, A.; LeBeau, J.; Augustyn, V., Transition from Battery to Pseudocapacitor Behavior via Structural Water in Tungsten Oxide. *Chemistry of Materials* **2017,** *29* (9), 3928-3937.

5. Wang, R.; Mitchell, J. B.; Gao, Q.; Tsai, W.-Y.; Boyd, S.; Pharr, M.; Balke, N.; Augustyn, V., Operando Atomic Force Microscopy Reveals Mechanics of Structural Water Driven Battery-to-Pseudocapacitor Transition. *ACS Nano* **2018,** *12* (6), 6032-6039.

6. Mitchell, J. B.; Geise, N. R.; Paterson, A. R.; Osti, N. C.; Sun, Y.; Fleischmann, S.; Zhang, R.; Madsen, L. A.; Toney, M. F.; Jiang, D.-e.; Kolesnikov, A. I.; Mamontov, E.; Augustyn, V., Confined Interlayer Water Promotes Structural Stability for High-Rate Electrochemical Proton Intercalation in Tungsten Oxide Hydrates. *ACS Energy Letters* **2019,** *4* (12), 2805-2812.

7. Uppuluri, R.; Sen Gupta, A.; Rosas, A. S.; Mallouk, T. E., Soft chemistry of ion-exchangeable layered metal oxides. *Chemical Society Reviews* **2018,** *47* (7), 2401-2430.

8. Schaak, R. E.; Mallouk, T. E., Perovskites by Design: A Toolbox of Solid-State Reactions. *Chemistry of Materials* **2002,** *14* (4), 1455-1471.

9. Naguib, M.; Gogotsi, Y., Synthesis of Two-Dimensional Materials by Selective Extraction. *Accounts of Chemical Research* **2015,** *48* (1), 128-135.

10. Anasori, B.; Lukatskaya, M. R.; Gogotsi, Y., 2D metal carbides and nitrides (MXenes) for energy storage. *Nature Reviews Materials* **2017,** *2* (2), 16098.

11. Xia, Y.; Mathis, T. S.; Zhao, M.-Q.; Anasori, B.; Dang, A.; Zhou, Z.; Cho, H.; Gogotsi, Y.; Yang, S., Thickness-independent capacitance of vertically aligned liquid-crystalline MXenes. *Nature* **2018,** *557* (7705), 409-412.

12. Lukatskaya, M. R.; Kota, S.; Lin, Z.; Zhao, M.-Q.; Shpigel, N.; Levi, M. D.; Halim, J.; Taberna, P.-L.; Barsoum, M. W.; Simon, P.; Gogotsi, Y., Ultra-high-rate pseudocapacitive energy storage in two-dimensional transition metal carbides. *Nature Energy* **2017,** *2* (8), 17105.

13. Perez, A. J.; Beer, R.; Lin, Z.; Salager, E.; Taberna, P.-L.; Abakumov, A. M.; Simon, P.; Tarascon, J.-M., Proton Ion Exchange Reaction in Li_3IrO_4: A Way to New $H_{3+x}IrO_4$ Phases Electrochemically Active in Both Aqueous and Nonaqueous Electrolytes. **2018,** *8* (13), 1702855.

14. Zhang, R.; Pearce, P. E.; Pimenta, V.; Cabana, J.; Li, H.; Alves Dalla Corte, D.; Abakumov, A. M.; Rousse, G.; Giaume, D.; Deschamps, M.; Grimaud, A., First Example of Protonation of Ruddlesden–Popper Sr_2IrO_4: A Route to Enhanced Water Oxidation Catalysts. *Chemistry of Materials* **2020,** *32* (8), 3499-3509.

15. Fleischmann, S.; Sun, Y.; Osti, N. C.; Wang, R.; Mamontov, E.; Jiang, D.-e.; Augustyn, V., Interlayer separation in hydrogen titanates enables electrochemical proton intercalation. *Journal of Materials Chemistry A* **2020,** *8* (1), 412-421.

16. Sanjaya Ranmohotti, K. G.; Josepha, E.; Choi, J.; Zhang, J.; Wiley, J. B., Topochemical Manipulation of Perovskites: Low-Temperature Reaction Strategies for Directing Structure and Properties. **2011,** *23* (4), 442-460.

17. Kendall, K. R.; Navas, C.; Thomas, J. K.; zur Loye, H.-C., Recent Developments in Oxide Ion Conductors: Aurivillius Phases. *Chemistry of Materials* **1996,** *8* (3), 642-649.

18. Schaak, R. E.; Mallouk, T. E., Exfoliation of layered rutile and perovskite tungstates. *Chemical Communications* **2002,** (7), 706-707.

19. Kudo, M.; Ohkawa, H.; Sugimoto, W.; Kumada, N.; Liu, Z.; Terasaki, O.; Sugahara, Y., A Layered Tungstic Acid $H_2W_2O_7 \cdot nH_2O$ with a Double-Octahedral Sheet Structure: Conversion Process from an Aurivillius Phase $Bi_2W_2O_9$ and Structural Characterization. *Inorganic Chemistry* **2003,** *42* (14), 4479-4484.

20. Kim, E.; Suzuki, S.; Miyayama, M., Electrode properties of layered tungsten-based oxides for electrochemical capacitors. *Journal of the Ceramic Society of Japan* **2014,** *122* (1426), 426-429.

21. Kresse, G.; Furthmüller, J., Efficient iterative schemes for ab initio total-energy calculations using a plane-wave basis set. *Physical Review B* **1996,** *54* (16), 11169-11186.

22. Perdew, J. P.; Burke, K.; Ernzerhof, M., Generalized Gradient Approximation Made Simple. *Physical Review Letters* **1996,** *77* (18), 3865-3868.

23. Blöchl, P. E., Projector augmented-wave method. *Physical Review B* **1994,** *50* (24),

17953-17979.

24. Grimme, S.; Antony, J.; Ehrlich, S.; Krieg, H., A consistent and accurate ab initio parametrization of density functional dispersion correction (DFT-D) for the 94 elements H-Pu. **2010,** *132* (15), 154104.

25. White, C. E.; Provis, J. L.; Proffen, T.; Riley, D. P.; van Deventer, J. S. J., Combining density functional theory (DFT) and pair distribution function (PDF) analysis to solve the structure of metastable materials: the case of metakaolin. *Physical Chemistry Chemical Physics* **2010,** *12* (13), 3239-3245.

26. Wang, R.; Chung, C.-C.; Liu, Y.; Jones, J. L.; Augustyn, V., Electrochemical Intercalation of Mg^{2+} into Anhydrous and Hydrated Crystalline Tungsten Oxides. *Langmuir* **2017,** *33* (37), 9314-9323.

27. Lin, H.; Zhou, F.; Liu, C.-P.; Ozoliņš, V., Non-Grotthuss proton diffusion mechanism in tungsten oxide dihydrate from first-principles calculations. *Journal of Materials Chemistry A* **2014,** *2* (31), 12280-12288.

Chapter 9. Summary and Outlook

9.1. Summary

In this dissertation, we employed density functional theory (DFT) combined with first-principles molecular dynamics (FPMD) simulation to study the ion behavior of pseudocapacitor electrodes for energy storage. We first start our study with the newly discovered two-dimensional transition metal carbides (MXenes). In particular, we studied proton dynamics in MXene-confined water. The FPMD trajectories show proton surface redox process happened reversibly on the different surface O sites mediated with proton transfer in the water layer. In between proton surface redox events, more frequent in-water proton-transfer events were observed. As the confined water layer becomes thinner, the proton surface redox rate increases but proton diffusivity decreases. By examine the proton diffusion mechanism, we found in the 2D-like confined water, the proton still follows the Eigen-Zundel-Eigen mechanism as in the 3D bulk water via special pair dance. Our study revealed that although proton dynamics are slowed down by the confinement, both surface redox and transport are fast. Indicating that the charging/discharging dynamics of MXene is limit by other processes like edge intercalation process. This pointed out the significance of nano-structure engineering of MXene to enhance the rate performance.

Besides MXene in the dilute acidic electrolyte, we then studied MXene in the water-in-salts electrolyte. We employed DFT simulations to quantitatively correlate the changes in interlayer spacing with the changes in the interfacial species. By correlating the DFT results with the in-situ X-ray diffraction (XRD) and electrochemical quartz crystal

microbalance (EQCM), we found 3 electrochemical stages during the cathodic scan. Moreover, the pair of abnormal peaks in the anodic and cathodic scans of the CV curves that contribute to increased charge storage capability is led by desolvation-free Li^+ (de)intercalation. The finding on the abnormal charging behavior when water-in-salts electrolyte is used provides a new strategy to expand the stable chemical window and increasing charge storage capability.

Other than ion transport and intercalation, we then investigated the interfacial structure of MXene edge by combining DFT calculation and structural search technique. The predicted most stable structure in vacuum showed an interlayer connection at the MXene edge, while the configurational search of hydrated MXene edge suggested the spontaneous CH_4 formation from the edge-water reaction, which well agreed with the previous experiment. Our study on MXene edge provides structural information that paves the way for further research on edge involved electrochemical process.

Next, we extend our study to tungsten oxide hydrates. We first investigated proton diffusion in tunnel *h*-WO_3 under different hydration levels. An optimal linear water density of 4 water/nm was found for proton conduction. Analyzing the proton dynamic along with the hydrogen-bonding defects (HBDs) showed that the optimal linear water density of 4 water/nm allows fast rotation of water molecules which further enables proton and HBDs to quickly move up and down the channel. Our study revealed the significance of the rotational ability of the water in proton dynamics that would expect to observe in other Grotthuss type of 1D proton diffusion system.

We then studied proton intercalation into monoclinic WO_3 hydrate which exhibits

2D layered structure. Our calculation of proton intercalation energy at different sites of $WO_3 \cdot 2H_2O$ suggests that the intercalated proton prefers to bond with the bridging oxygen site of the W-O lattice rather than crystal water molecules. The calculated vibrational densities of states (VDOS) obtained from the FPMD simulation of $WO_3 \cdot H_2O$ agrees well with the inelastic neutron scattering (INS) measurement and confirms the proton present at bridging oxygen sites. These together indicate that $WO_3 \cdot nH_2O$ stores protons at bridging oxygen sites. Our DFT results demonstrate the fast proton insertion ability observed in the hydrates is not from the fast Grotthuss type of proton diffusion among crystal water but the experimentally observed crystal water enabled flexible structure. We also studied another phase of tungsten oxide hydrates $H_2W_2O_7$. By performed an iterative approach using DFT geometry optimization and multi-modal characterization, we are able to obtain a high-fidelity crystal structure of $H_2W_2O_7$. The further calculations of photon absorption energy demonstrate low proton absorption energy at terminal oxygen sites. This work showed DFT is a powerful tool to study the crystal structure of the condense phase.

Our simulations provide important mechanistic understandings on the pseudocapacitive mechanism of MXenes and tungsten oxide hydrates in different aspects, including ion transport, adsorption and interfacial structure, which greatly benefit future development of energy storage technologies.

9.2. Outlook

For an ideal battery model, the phase transition of electrochemical reaction happened at a specific voltage stage that can be obtained directly from the free energy change of the phase transition. However, for pseudocapacitive electrode material, the

electrochemical reaction occurs at continuously varying potential that can't be calculated from simple thermodynamic potential of bulk material. The surface or interfacial effects become nonnegligible to the pseudocapacitive behavior. Under this circumstance, it's hard to understand the nature of the surface redox reaction from the electrochemical response. Our conventional interpretation based on battery-type behavior of the electrochemical response may not apply in pseudocapacitive behavior. Although there are emerging *in-situ* or *ex-situ* techniques to characterize the structure change during the charge/discharge process, it hard to interpret the results due to the complexity of the system. Developing atomistic simulation methods that can model the spectroscopy feature could bridge the gap between the structure and the experimental characterization. Therefore, we can broaden the mechanistic understanding of the electrochemical response.

Moreover, as the system becomes complex, we now can only capture part of the structural feature that contributes to the pseudocapacitive behavior. Therefore, developing atomistic predictive models that can efficiently include all aspects that contribute to the pseudocapacitive behavior is desired. Key to this development is computationally efficient integration of the bulk and surface chemistry of the electrode, the applied potential across the interface, the formation of the double-layer, the solvation environment. Once these accurate predictive models are developed, computation could guide the design of energy storage material or devices. This would expedite our pace in developing high-power and high-energy density energy storage materials.